BRAGG GRATING FORMATION IN PMMA FIBERS DOPED WITH TRANS-4-STILBENEMETHANOL

ZHIFENG ZHANG

Ph.D

The Hong Kong Polytechnic University

2013

The Hong Kong Polytechnic University

Institute of Textiles and Clothing

Bragg Grating Formation in PMMA Fibers

Doped with trans-4-Stilbenemethanol

Zhifeng ZHANG

A thesis submitted in partial fulfillment of the requirements

for the degree of Doctor of Philosophy

APR 2012

Certificate of Originality

I hereby declare that this thesis is my own work and that, to the best of my knowledge and belief, it reproduces no material previously published or written, nor material that has been accepted for the award of any other degree or diploma, except where due acknowledgement has been made in the text.

_____ (Signed)

_____ Zhifeng ZHANG_____ (Name of student)

Abstract

Polymer fiber Bragg gratings (PFBGs) are an emerging sensor technology in smart structures and biomedical applications. However, the formation mechanism of PFBGs has not been fully understood despite some limited successes in laboratory-made sensors. Therefore, this thesis is focused on a systematic study of the PFBG formation in PMMA based fibers doped with *trans*-4-stilbenemethanol (TS).

Step-index single-mode polymer optical fibers (POFs) were fabricated by the preform-drawing method. First, the photosensitivity of the core film was investigated by the refractive index reduction induced by UV irradiation and confirmed by formation of volume film gratings. Secondly, the refractive index profile of the fabricated fibers was directly measured, and step-index profile was achieved by prepolymerizing the monomer for fiber core. Thirdly, the diameter fluctuation of the fabricated POFs was significantly reduced by stopping natural convection in the heating jacket of the drawing tower with a cap.

PFBGs have been inscribed by using phase masks that have a wide range of zeroth order diffractions, for example, a phase mask with zeroth order diffraction up to 49%, far exceeding the maximum requirement to write fiber Bragg gratings (FBGs) as previously reported (<5%). In addition, the microstructure of the fabricated PFBGs was found to be dependent on phase masks. Hence, the near-field of phase masks was simulated based on their diffraction ratios. The calculation revealed that the near-field of phase masks was influenced not only by the zeroth order diffraction, but

also the second and the third. The simulated near-fields agreed with the observed microstructures of the fabricated PFBGs to a large extent.

The formation dynamics of PFBGs during long-time phase masked UV exposure was studied. The Bragg peak increased rapidly immediately after UV exposure and reached the first highest level within ~5 minutes, and then dropped slightly or maintained constant. About 20 min after UV exposure started, the Bragg peak increased again and reached the second highest value. Finally, the Bragg peak decreased slowly and vanished. The observation of grating microstructure revealed that the POF was severely damaged after 20 min of exposure, and hence the optimal inscription time was ~5 min.

For PFBGs that were inscribed by 5 min (also for 1, 15, or 30 min) of phase masked UV exposure, the Bragg peak continued to vary after exposure. The peak power decreased and almost disappeared within a few hours, but slowly recovered over one day. This relaxation process was observed for the first time in PFBGs. It has been found that heating the as-fabricated PFBGs can effectively speed up this relaxation process. Several hypotheses, such as the moisture absorption/desorption and back-reactions forming TS, were proposed and tested to explain this relaxation process. After careful investigation, however, the most probable reason for this relaxation process was ascribed to the stress relaxation induced by photoisomerization because of geometrical difference in trans and cis isomers of 4-stilbenemethanol.

The fabricated PFBGs were found to be highly sensitive to relative humidity (RH). For example, the measured humidity sensitivity of a PFBG around 1310 nm was -66 pm/%RH. Moreover, the humidity and temperature were found to have a synergetic

effect on PFBGs. That is, the temperature sensitivity is humidity-dependent and vice versa. Thermal response of the fabricated PFBGs was measured in ambient conditions and at constant RH. For a 1308 nm PFBG, the measured temperature sensitivity at 0 %RH and 60 %RH were -1 and -8.7 pm/℃, respectively, which are one to two orders of magnitude lower than the value measured in ambient conditions.

A sensor integrated with two PFBGs was developed for simultaneous measurement of shear stress and pressure by placing one PFBG horizontally and the second tilted in a silicone cube. Finite element analysis revealed that the induced strain along fiber axis was not uniform if the fiber was bonded to the silicone matrix. The identified better configuration was to have a friction-free interface between the fiber and the silicone matrix, and loading the PFBGs by the deformation of the elastic cube at its boundary. Hence, release agent was applied on the surface of POFs to prevent the bonding, and two gaskets were adhered to two ends of each fiber to stretch the fiber under loading. The measured sensitivity of pressure and shear stress were 0.82 and 1.33 nm/kPa, respectively.

Publications Arising from the Thesis

Published Journal Papers

[1] Z. F. Zhang, X. M. Tao, "Intrinsic Temperature Sensitivity of Fiber Bragg Gratings in PMMA-Based Optical Fibers," *Photonics Technology Letters, IEEE*, vol.25, no.3, pp.310-312, Feb.1, 2013

[2] Z. F. Zhang and X. M. Tao, "Synergetic Effects of Humidity and Temperature on PMMA Based Fiber Bragg Gratings," *Journal of Lightwave Technology*, vol. 30, pp. 841-845, 2012.

[3] Z. F. Zhang, C. Zhang, X. M. Tao, G. F. Wang and G. D. Peng, "Inscription of Polymer Optical Fibre Bragg Grating at 962 nm and its Potential in Strain Sensing," *Photonics Technology Letters, IEEE*, vol. 22, PP, pp. 1562-1564, 2010.

[4] Z. F. Zhang, X. M. Tao, H. P. Zhang, B. Zhu, "Highly Sensitive Soft Fiber Optic Sensors for Simultaneous Measurement of Shear Stress and Pressure," accepted by *Sensors Journal, IEEE*.

Conference proceedings

[5]. Z. F. Zhang, X.M. Tao, G. F. Wang, and J. M. Yu, "Volume Phase Holographic Grating Fabricated in *trans*-4-Stilbenemethanol Doped PMMA." Progress in Electromagnetics Research Symposium (Key: 090902213612), Xi'an, March 2010.

Papers in preparation

[6] Z. F. Zhang, X.M. Tao, "Relaxation of Fiber Bragg Gratings in PMMA based optical fibers doped with *trans*-4-stilbenemethanol".

Acknowledgements

First, I would like to sincerely thank Prof. Tao Xiao-Ming for her expert guidance, inspiring encouragement and invaluable help. The breadth and depth of her knowledge, spanning from chemistry to material science, from physics to optics, from textiles to mechanics and more, amazed me ever since the start of this study. Her enthusiasm to scientific knowledge and focus on engineering problems set a perfect example for the rest of my academic life. It is my life-long fortune to be supervised by her.

I would also like to thank Prof. Peng Gang-Ding for his guidance and generous help on the experiments during my short visit to The University of New South Wales.

Several others had helped me during my thesis study. Dr. Sun Xiao-Hong taught me a lot on optics at the beginning; Dr. Zhang Hua-Peng conducted the finite element analysis on the shear sensor and provided valuable understandings; Dr Zhang Chi gave me many helpful advices on grating writing. I would like to thank all of them. Thanks are also due to Mr. Hui Kevin for his technical support on optics experiments.

I am indebted to my colleagues in Prof. Tao's group, with whom I have great pleasure to study and live: Dr. Wang Guang-Feng, Dr. Wang Yang-Yong, Dr. Zhu Bo, Dr. Hua Tao, Mr. Zheng Wei, Ms. Shen Jing, Mr. Shu Lin, Mr. Yi Wei-Jing, Mr. Feng Jie, Dr. Guo Ying, Ms. Huang Xing-Xing, Mr. Li Ming- Jian, Ms. Li Qiao, Mr. Wang Fei, Mr. Chen Song, Ms. Mai Kai-Ying et al.

Finally, I sincerely thank my hard-working parents, my diligent and supportive wife, my kind and considerate sister and brother-in-law, and my energetic brother. Without their love and encouragement, this thesis would never be done.

Table of Contents

List of Figures

XIII

List of Tables

Abbreviations and Symbols

AFM	Atomic Force Microscope
BA	Butyl acrylate
BDK	Benzil dimethyl ketal
BzMA	Benzyl methacrylate
COC	Cyclic olefin copolymer
CTE	Coefficient of thermal expansion
CYTOP	Amorphous transparent perfluorinated polymer developed by Asahi Co. Ltd.
EMA	Ethyl methacrylate
FBG	Fiber Bragg grating
FEA	Finite element analysis
FEM	Finite element model
hFBG	The polymer fiber Bragg grating horizontally embedded in the shear stress and pressure sensor
MMA	Methyl methacrylate
MPOF	Microstructured polymer optical fiber
MPU	Mesoscale photomechanical unit
NA	Numerical aperture
OSA	Optical spectrum analyzer
PC	Polycarbonate
PFBG	Polymer fiber Bragg grating
POF	Polymer optical fiber
PS	Polystyrene
RH	Relative humidity
RI	Refractive index
RIP	Refractive index profile
SMF	Single-mode fiber (glass fiber)
SRG	Surface relief grating
tFBG	The polymer fiber Bragg grating embedded in the shear stress and pressure sensor with an angle to the horizontal plane

TFEMA	2,2,2-Trifluoroethyl methacrylate
TOPAS	TOPAS Advanced Polymer Co. Ltd.
TS	*trans*-4-Stilbenemethanol
UV	Ultra-violet
VHG	Volume holographic grating

ε_n	Normal strain
ε_s	Shear strain
Λ_0	Period of grating before annealing
Λ_n	Period of grating after n^{th} annealing
D_f	Diameter of fiber
D_p	Diameter of preform to draw fiber
H_e	Radiant exposure on the film, mJ/cm^2
M_w	Molecular weight
N_A	Avogadro constant
N_c	Area density of *cis*-4-stilbenemethanol, mol/cm^2
N_t	Area density of *trans*-4-stilbenemethanol, mol/cm^2
N_{t0}	Initial area density of *trans*-4-stilbenemethanol, mol/cm^2
dn/dT	Thermo-optic coefficient
n_1	Refractive index of fiber cladding
n_2	Refractive index of fiber core
n_3	Refractive index of fiber core after laser irradiation
n_{eff}	Effective refractive index of fiber core within range of Bragg grating
p_{11}	Component of strain-optic tensor
p_{12}	Component of strain-optic tensor
p_e	Effective strain-optic coefficient
v_f	Drawing speed of fiber
v_p	Feeding speed of preform during fiber drawing
α_Λ	Linear coefficient of thermal expansion
α_n	Normalized thermo-optic coefficient

β_Λ	Coefficient for refractive index change induced by humidity change $(\frac{1}{n}\frac{\partial n}{\partial H})$
β_n	Coefficient for expansion induced by humidity change $(\frac{1}{\Lambda}\frac{\partial \Lambda}{\partial H})$
ε_t	Absorption rate
λ_0	Bragg wavelength of the grating before annealing
λ_n	Bragg wavelength of the grating after n[th] annealing
M	Molar concentration of salt solution, mol/L
Δn	Refractive index change
Λ	Pitch of fiber Bragg grating
C	Weight percentage of *trans*-4-stilbenemethanol, wt %
E	Relative humidity raging from 0 to 100%
H	Relative humidity from 0 to 1
NA	Numerical aperture
T	Temperature in ℃
V	Normalized frequency number
g	Acceleration of gravity, m/s^2
l	Film thickness, cm
n	Refractive index
η	Quantum efficiency
λ	Bragg wavelength
ν	Light frequency
ρ	Density of PMMA, g/cm^3
σ_n	Normal stress
σ_s	Shear stress
$\eta(V)$	Fraction of the integrated fundamental-mode intensity contained in the core
F_n	Normal force applied on the shear stress and pressure sensor
F_s	Shear force applied on the shear stress and pressure sensor
R	Peak reflectivity of fiber Bragg grating
L	Length of fiber Bragg grating

CHAPTER 1 INTRODUCTION

1.1. Background

Fiber Bragg gratings (FBGs) have been extensively studied and successfully applied in the last three decades [1-5]. FBG is an in-fiber component formed by periodically modulating the refractive index (RI) of the core of an optical fiber. Its primary function is to reflect light at a certain wavelength. The first Bragg grating in optical fiber was observed by Hill et al in 1978 [6]. Since then, FBGs have been fabricated by several methods, such as the interferometric method [7] and the phase mask method [8]. Owing to their high sensitivity and multiplexing capability, FBGs have been widely used as various kinds of sensors, along with their vast application in fiber optic communication [9]. Major advantages of FBG sensors include high sensitivity, electrical immunity, and remote and distributed sensing capability. To date, almost all FBGs in real applications have been written in silica optical fibers due to their superior properties.

Bragg gratings written in silica fibers, however, have several disadvantages or limitations when used as sensors. When used as temperature sensors, their sensitivity is relatively low, about 10 to 15 pm/°C for gratings at 1.5 μm [10]. The main cause of this low temperature sensitivity is the small thermo-optic coefficient of the fused silica (8.6×10^{-6} °C^{-1}) [5]. The strain measurement range of FBGs in silica fiber is low, normally lower than 1% [5]. Furthermore, the silica fiber is brittle, and broken fibers are extremely dangerous to eyes and skins. These safety issues hinder the application of Bragg gratings in silica fiber for applications in vivo measurement.

FBGs in polymer optical fibers (POFs) are promising to address the above issues, despite that their research and application are severely inhibited by high loss, poor stability of POFs, and also by their incompatibility with silica fibers. The thermo-optical coefficient of POFs is almost one order larger than that of silica fibers. POFs can be stretched much longer than silica fibers. PMMA based polymer fibers can be stretched by 80% before break [11], and the yielding strain is up to 6% [12]. Therefore, polymer FBGs (PFBGs) would provide much broader range of strain sensing. PMMA, one of the most common optical polymers, has outstanding biocompatibility, and this makes Bragg gratings in PMMA fibers ideal for biosensing. In addition, PFBGs are ideal devices for inclusion in an organic solid-state fiber laser [13], which in turn provides a compact and low-cost optical source over a broad range of wavelength throughout the visible spectrum [14].

Moreover, polymers provide an ideal platform for the incorporation of more complex material functionalities through selective doping or reaction, thereby enabling amplification and electro-optic effects to be achieved. It has been demonstrated that a single fiber can be incorporated with conductors, semiconductors and insulators to form fiber devices, paving the way to multifunctional fabric systems [15]. As an example directly related to PFBGs, Kalli et al coated POFs written with FBG via photochemical deposition of a Pd/Cu metallic layer with a procedure induced by vacuum-ultraviolet radiation at room temperature, and the FBG can be tuned over a 2 nm range by applying electricity due to joule heating [16, 17]. Another major growth area for POF is the biomedical applications, as biological materials are much more compatible with organic polymers than with glasses. The surface of polymers is readily functionalized with materials of biological interest [18].

Studies on Bragg gratings in POFs are as yet limited especially in regard to grating formation mechanism, despite that this area has been attracting increasingly more research interest. Peng et al firstly report Bragg gratings written in fibers without dopant [19], and Rhodamine 6G doped PMMA optical fibers [20]. The grating formation mechanism in Rhodamine 6G originates from the absorption of the writing laser by Rhodamine 6G, but what reactions occur after absorption is unclear. The grating formation in fiber without dopant is thought to be photo-induced cross-linking or photopolymerization. Yu and co-workers studied the changes in RI and thickness of PMMA films under irradiation by UV light. They found that the UV irradiation generated volatile molecules due to degradation. Growth dynamics study of Bragg gratings reveals two distinct grating formation stages. In the first stage, the index modulation increases slowly and linearly; whereas in the second stage, the index increases exponentially [21, 22]. Microstructure observation suggests that the index modulation in the second stage is caused by damage to the fiber under long time exposure, but the index modulation in the first stage is uncertain.

Because a long time of irradiation was needed to write gratings in PMMA based fibers without dopant, our research group developed single-mode POFs doped with a photoactive organic—*trans*-4-stilbenemethanol (TS) [23]. This fiber is photosensitive thanks to the permanent RI modulation induced by photoisomerization of TS under UV irradiation at an appropriate wavelength (e.g. 325 nm). Although Bragg gratings had been demonstrated in this fiber, there were still difficulties to repeat the experiment at the start of this project. Effects other than photoisomerization of TS had been noticed, Bragg peaks appeared in the fiber without the dopant after several hours of UV exposure, and saturated after ~32 h [23].

The chemical or physical processes behind this phenomenon are unknown yet, and they are also involved in the grating formation process in fibers doped with the photoactive materials. Another major problem is the consistency of the qualitiy of single-mode POFs. The fiber used in [23] has a core diameter of 20 μm, and the RI difference between its core and cladding was not measured directly from the fiber, instead, it was estimated from the film measurement. The refractive index profile (RIP) of the fabricated fiber, the most important property of an optical fiber, is unknown.

1.2. **Problem Statement**

Based on the background, three major research problems within the area of PFBGs are summarized as follows: (1) Fabrication technology of high quality single-mode POFs suitable for grating inscription is at their earlier era, which retards much needed application of PFBGs. (2) The most critical parameter for such single-mode POFs is their cross-section profile of refractive index and variation along fiber length. The refractive index profile of single-mode POFs has been estimated on the preform rather than directly measured. (3) The modulation of refractive index by chemical or physical changes have not been fully investigated, needless to say understood during grating inscription. In the previous work of TS doped PMMA fibers, the photoisomerization of TS molecules has been assumed to be the primary process to induce negative refractive index modulation, which may destroy the wave guiding condition. Furthermore, the effect of UV irradiation on the bulk polymer has not been studied.

1.3. **Objectives**

This project attempts to investigate and understand the formation mechanism of Bragg gratings in TS doped polymer fibers based on PMMA. The main objective is to answer the question of what account for the formation of Bragg gratings in TS doped fibers. To investigate the grating formation process, polymer fibers doped with TS must be fabricated first, which is another objective of this project. It is necessary to test their thermal and strain responses because these two properties are most concerned for a PFBG sensor. Finally, sensors based on the fabricated PFBGs will be developed to demonstrate their practical applications.

In short, there are four specific objectives for this study: (1) to prepare single-mode PMMA POFs doped with TS and improve their quality; (2) to study the grating formation process and to understand the grating formation mechanism, so that PFBGs can be inscribed readily; (3) to test thermal and strain responses of the fabricated PFBGs, so as to determine the temperature and strain sensitivities; (4) to develop sensors based on the fabricated PFBGs to demonstrate their practical application.

1.4. **Methodology**

1.4.1. **Preparation of photosensitive single-mode POFs**

Photosensitive single-mode POFs will be fabricated by the preform-drawing technique, while the preform is prepared by the Teflon thread method. The RIP of the fabricated fibers will be directly measured, and the fabrication process will be optimized so that the fabricated fibers have the step-index profile. Also, the drawing

process will be investigated and analyzed to find the most influential factors that affect the quality of the resultant fibers, so that measures can be taken to improve fiber quality accordingly, especially the evenness of fiber diameter. In addition, the fiber attenuation will be measured by the cut-back method.

The photosensitivity of the fiber core, that is, TS doped methyl methacrylate (MMA) copolymer, will be studied in the form of film. The photosensitivity will be confirmed by two approaches: (1) the RI change of the film induced by UV irradiation; (2) the formation of volume Bragg gratings in the film. The RI of the film can be measured by a prism coupler. Either the phase mask technique or the interferometric setup can be employed to writing volume Bragg gratings in the film, and the formation of volume Bragg gratings can be determined by their diffraction.

1.4.2. **Inscription of PFBGs**

PFBGs will be inscribed in the fabricated fibers using the phase mask technique, and the interferometric method will be also tried. In order to readily write gratings, factors that might influence the Bragg grating formation will be investigated. These factors include the zeroth order diffraction of phase masks and configuration of the writing system. Moreover, the formation dynamics of Bragg gratings in the fabricated POFs will be closely investigated to understand the grating formation mechanism.

1.4.3. **Characterization of PFBGs**

Characterization of the fabricated gratings includes their micro structure, thermal and strain responses. Structure of the PFBGs will be examined by microscope. Thermal

and strain responses of the PFBGs can be characterized by their wavelength shift upon heating or stretching. The response of PFBGs to humidity will be investigated by controlling the relative humidity around PFBGs. In addition, Bragg wavelength shift of PFBGs induced by annealing will be monitored to study the impact of annealing treatment on PFBGs.

1.4.4. **Shear stress and pressure sensor**

The sensor will be a silicone cube embedded with two PFBGs. One of them is horizontally placed, and the other one is tilted. The transduction principle is the strain induced on two POFs by deformation of the cube under force or displacement loading. Both gratings should have response to normal and shear loading, and by combining their responses the normal and shear loading will be discriminated and determined.

1.5. **Project Significance**

The major contribution of this project lies in the study of formation mechanism of gratings in the TS doped PMMA fibers. Though previous studies have fabricated and tested PFBGs, the chemical or physical processes induced by UV irradiation in POFs during grating inscription are still unclear. This study attempts to reveal these chemical or physical processes, so as to understand the grating formation mechanism. In addition, this project directly measures the refractive index profile of the fabricated POFs, providing their most important physical property so that single-mode nature of fabricated POFs can be satisfied and confirmed. Another significance of this project is the study of combined impact of humidity and temperature on

PFBGs, while most previous studies only investigated either their thermal response or humidity response.

1.6. **Structure of the Thesis**

This thesis comprises seven chapters. Chapter 1 describes the background of this study, brings up the research questions and accordingly states the research objectives, and lastly reveals the research methodology. Chapter 2 conducts an extensive review on the PFBGs. Chapter 3 studies the photosensitivity of the TS doped copolymer based on MMA. Chapter 4 deals with the fabrication and characterization of photosensitive single-mode POFs. Chapter 5 presents investigations on the PFBGs, including their inscription and characterization. Chapter 6 reports an example of application using the fabricated PFBGs, that is, an ultra sensitive sensor that can simultaneously measure shear stress and pressure. Chapter 7 concludes the thesis by summarizing the main findings and presenting suggestions on the future work.

CHAPTER 2 LITERATURE REVIEW

This chapter presents an extensive review on the PFBGs, including the fabrication of photosensitive single-mode POFs, inscription of PFBGs in the fabricated POFs, their thermal and strain responses, and some emerging applications of PFBGs. The purpose of the review is to develop a complete understanding of the previous research in this area, and identify issues for further investigations.

2.1. **Fabrication of Photosensitive Single-mode POFs**

Single-mode POFs are preferred for Bragg gratings because of several reasons. First, the reflection spectrum of FBGs in the single-mode fibers has only one peak, which makes the measurement much easier as many peaks may overlap with each other [24, 25]. Secondly, the multiplex capability of the sensing system based on FBGs, one of the key advantages of FBGs technology, is severely degraded if multi-mode fibers are used. For example, for a light source with 70 nm band width, 70 gratings can be discriminated in a single fiber if the bandwidth of reflection peak is 1 nm, but if there are two Bragg peaks for each grating with the same width of 1 nm, only 35 gratings can be discriminated. Lastly, the Bragg peak power of FBGs in the single-mode fibers is higher than those in multi-mode fibers for the same input power and same RI modulation because the light power distributes in various modes in multi-mode fibers. Nevertheless, Bragg gratings in multi-mode fibers have been studied in some cases. For example, Luo et al studied the reflection spectra of multimode PFBGs subjected to axial strain, and the respective effects of strain on each reflection peak were measured to analyze the sensitivity of each peak to strain [26].

Table 2.1 Specifications of single-mode POFs provided by Paradigm and Kiriama

Product NO.	Specification	Supplier
MORPOF02	Fiber core: copolymer of MMA and styrene Core diameter 3.1 μm; NA=0.27 Cutoff wavelength 1100 nm	Paradigm
MORPOF03	Core diameter 8 μm; NA = 0.07 Cutoff wavelength 750 nm	
MORPOF04	Core diameter 3.4 μm; NA = 0.11 Cutoff wavelength 600 nm *Fiber core doped with DCM (dicyanmethylene-2-methyl-6-1(p-dimethylaminostyryl)-4H-pyran).*	
MORPOF05	Fiber core: copolymer of MMA and styrene Core diameter 3.4 μm; NA=0.27 Cutoff wavelength 1400 nm	
SM-125	Core diameter 6 μm; Loss at 650 nm: 3.8 dB/cm Cladding diameter: 125 μm; PMMA core and cladding	Kiriama
SM-340	Core diameter 8 μm; Loss at 650 nm: 3.8 dB/cm Cladding diameter: 125 μm; PMMA core and cladding	

Though multi-mode POFs are manufactured by a large number of companies, only two suppliers of single-mode POFs have been found, namely, Paradigm Optics Inc. (Paradigm) and Kiriama Pty Ltd (Kiriama). Paradigm provides four types of step-index single-mode fibers; Kiriama sells two types of single-mode microstructured POFs. Specifications of these six fibers are listed in Table 2.1. FBGs have been written in some of some of these fibers, such as MORPOF02 [27, 28] and MORPOF03 [29] from Paradigm. PFBGs have also been successfully written in multi-mode fibers from Kiriama [30]. However, these six fibers except MORPOF04 from Paradigm are not photosensitive intrinsically, so formation of FBGs in them is mainly due to photodegradation of fibers under prolonged UV irradiations. MORPOF04 doped with DCM is photosensitive, but not ideal for grating inscription because DCM absorbs visible light. Hence, photosensitive single-mode POFs are fabricated rather than purchased in this study due to the fact that all commercially available POFs are not ideal for inscription of Bragg gratings.

Furthermore, fabricating fiber rather than purchasing allow us to fine-tune the properties of fibers. However, drawing photosensitive single-mode POFs is a major challenge. The very first consideration of fabricating fibers is to select appropriate polymers as basic optical material.
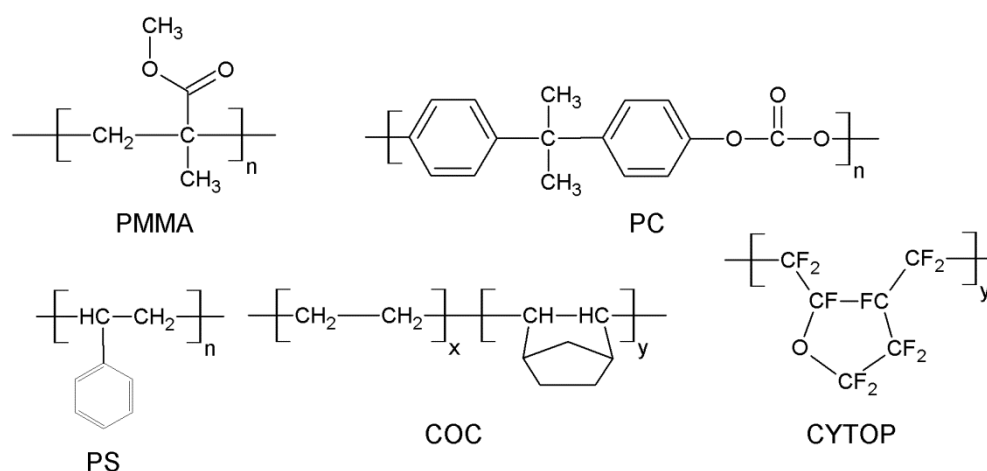
Figure 2.1 Molecular structure of five polymers commonly used as material for POFs

2.1.1. Selection of optical polymer

PMMA, polycarbonate (PC), polystyrene (PS), CYTOP (an amorphous fluoropolymer developed by Asahi Glass Co. Ltd) and cyclic olefin copolymer (COC, e.g. TOPAS COC produced by TOPAS Advanced Polymer Co. Ltd) are some commonly used optical polymers that can be chosen to fabricate single-mode POFs. Chemical structures of these five polymers are illustrated in Figure 2.1, and their properties are listed in Table 2.2. Among these five polymers, PMMA is still the material of choice for most POFs, mainly because of its easy fabrication process via radical polymerization. Moreover, properties of PMMA can be readily altered by copolymerization with other acrylic monomers to meet any particular requirements.

Table 2.2 Properties of PMMA, PC, PS, CYTOP, and TOPAS COC

	PMMA	PC	PS	TOPAS COC	CYTOP
RI	1.49[a] [31]	1.58[a] [31]	1.59[a] [32]	1.53 [33]	1.34
T_g (°C)	104	170	~90	70-177 [33]	108
Melting point (°C)	160	267	240	190-320	-
Coefficient of thermal expansion (10^{-4} °C^{-1})	0.68[b][31]	0.66[b] [31]	-	0.6 [33]	1.15-1.20
Thermo-optic coefficient dn/dT (10^{-4} °C^{-1})	-1.05 [b] [31] -1.2[b] [34]	-1.07[b] [31] -1.1 to -1.4[b] [34]	-	-1.0 [33]	-
Stress-optic coefficient (10^{-12} Pa^{-1})	-4.5 to -1.5 [35]	68	4.8	4.0	-
Moisture absorption (wt %)	Up to 2.0	0.04	0.1-0.3	0.01[33]	-

[a]: At 632.8 nm
[b]: At 20 °C

PC is superior over PMMA in mechanical properties, and has higher operation temperature thanks to higher T_g, but its polymerization and modification is not as easy as that of PMMA. PS is rarely used to fabricate POFs because it has no distinct advantages over PMMA. Moreover, phenyl groups in PS make the material vulnerable to UV light. CYTOP achieved extremely low loss compared to PMMA. However, the polymerization technology of CYTOP is not available due to technology protection, and hence fabricating it from chemicals is not feasible. Nevertheless, there has been attempt to draw single mode POFs with CYTOP core. Zhou et al prepared a preform by polymerizing MMA around a multi-mode POF of CYTOP, and draw the preform into fiber to reduce core of the multi-mode fiber to satisfy the single-mode condition [36]. COC, a newly invented transparent polymer, also has been applied to fabricate single-mode POFs, and all fabricated POFs based on it are microstructured or holey type. The most attractive feature of COC is its low moisture absorption (e.g. ≤ 0.01% for TOPAS COC).

2.1.2. **Photosensitivity of POFs**

To be photosensitive in the context of optical fibers means the RI of the fiber core can be permanently photo-modulated, usually by UV laser. The mechanism of RI modulation is the main topic of the photosensitivity study. The photosensitivity of POFs is mainly determined by the material of the fiber core, but also depends on the macromolecular structure and morphology, and also irradiation conditions like laser wavelength and irradiance [37]. Deep understanding about the grating formation mechanism is essential to improve the writing method and the quality of FBGs.

2.1.2.1. POFs without dopant

Bragg gratings have been fabricated in PMMA [19, 38, 39], CYTOP [40, 41] and TOPAS COC [42] fibers without dopant. The formation dynamics of Bragg gratings in fibers, that have a core of poly(methyl methacrylate/ethyl methacrylate/benzyl methacrylate), has been closely studied [19, 21, 22, 43], but the explanation of the grating formation is still based on the general understanding of the photo-effect of UV light on polymers. Generally, UV irradiation on polymers with low-level exposure leads to the chain scission, or cross-linking of macromolecules, which normally increase the RI of PMMA films [44-48]. Photopolymerization would also occur if there are residual monomers. Experimentally, writing gratings in polymer fibers (either based on PMMA or COC) without dopant takes a very long time, which inevitably causes damage to the fibers. Moreover, this kind of RI modulation seems more likely due to photodegradation of fiber core [43]. The damage to fiber core leads to a higher attenuation of the fiber.

2.1.2.2. POFs doped with trans-4-stilbenemethanol

Our research group proposed and developed photosensitive POFs by doping the fiber core with photoactive TS, and successfully written PFBGs in them [23, 49-51]. TS exhibits a reversible trans-cis photoisomerization by irradiation of light at appropriate wavelength [52, 53], as shown in Figure 2.2. The refractive indices of two configurations are different [54]. Usually the trans type exhibits a higher RI, which provides an opportunity for the realization of photoinduced RI change by photoisomerization.
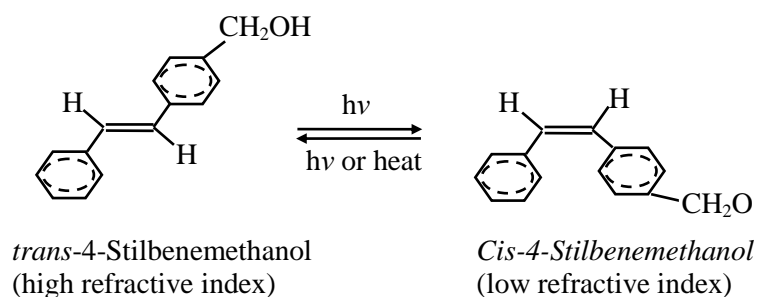
Figure 2.2 Reversible isomerization of 4-stilbenemethanol under UV irradiation or heat

The trans-cis photoisomerization of TS is a unimolecular photochemical reaction. The trans configuration can be converted to cis under UV irradiation at certain wavelength like 325 nm , and cis can reversibly transform to trans by irradiation at other wavelengths like 250 nm. The cis-trans isomerization is thermodynamically spontaneous since the trans configuration has a lower energy. The thermal isomerization has several impacts on the present study. Although the trans isomer has the thermodynamically stable configuration, isomerization of trans-cis is utilized to induce RI change because only the trans configuration is commercially available. This means that the fabricated gratings might not be stable thermodynamically. But our earlier experiments showed that the cis configuration was stable even heated up

to 80 °C due to the high activation energy required for cis-trans transformation when being doped in MMA copolymer [53]. The activation energy from cis to trans configuration for stilbene is up to 180 kJ/mol [55]. This is one of the major reasons to adopt stilbene rather than azobenzene. Even in the dark, the equilibrium state of azobenzene is composed of almost purely trans isomer, and half lifetime of cis isomer of azobenzene ranges from several seconds to several days [56].

The fiber core was doped with TS so that permanent Bragg gratings were formed due to the RI change of the fiber core induced by photoisomerization. The host polymer has a great impact on the grating formation. In addition, other effects induced by laser irradiation also affect grating formation, such as photo-orientation [57] or photomechanical effects [58]. Another important process that might have an impact on the grating formation is the diffusion of dopants after grating formation, which is known as grating relaxation and has been well studied and applied on the film gratings and volume gratings [59-61]. This diffusion process has not been reported in the PFBGs.

2.1.2.3. POFs doped with other photoactive dopants

Other photoactive dopants that have been introduced into POFs for grating inscription include fluorescein and Rhodamine 6G [20, 62], azo dye [63, 64] and benzil dimethyl ketal (BDK) [65]. Fluorescein and Rhodamine 6G were used because they absorb light around 355 nm, which is one of the typical wavelengths of the UV laser for grating inscription. Azo dyes photoisomerize in the similar way like TS, thus they were doped into the fiber core. BDK molecules absorbed photons and split to produce free radicals and the produced radicals could initiate a series of

reactions within the fiber core. Compared with TS, the photochemical reactions of these dopants after excitation are not known, and the most probable reactions are the decomposition of dopants molecules and degradation of host polymers.

2.1.3. **Preform fabrication**

The preform-drawing technique is the only method that has been used for fabrication of single-mode POFs. In principle, the co-extrusion method, which is widely used in industry to fabricated large-core multi-mode POFs, can also be used to draw single-mode POFs. However, the co-extrusion method is not that suitable for fabrication of single-mode POFs in laboratories, because the design and control of the co-extrusion system is sophisticated and complex. The preform-drawing method can be easily implemented in laboratories, and is able to draw solid-core and microstructured POFs as long as the preform is processed accordingly. The preform-drawing method involves two steps: (1) preparing the preform and (2) heating and drawing the preform to fiber. Kuzyk thoroughly reviewed fabrication methods of preforms to draw single-mode POFs in [66], and classifications and nomenclatures in it are adopted here. Processes of preparing preforms for solid-core POFs and microstructured ones are different, hence they are treated individually.

2.1.3.1. Preparing preform for solid-core POFs

Three major schemes to fabricate preforms for solid-core POFs are listed and compared in Table 2.3. The earliest reported method is polymerizing the cladding around a core fiber [67]. The core preform was polymerized and drawn into a fiber, and then the cladding was polymerized around the core fiber fastened at the center of a test tube. The obtained preform was then embedded in a PMMA tube and heated

and drawn into a fiber. The embedding and drawing processes were repeated to decrease the core diameter to satisfy the single-mode condition. This approach is not only complex in procedure, but also has strict requirements on the drawing process. The core fiber must have an even diameter along its axis, otherwise the ultimate fiber will have different core diameter even the diameter of cladding is uniform. In addition, this approach needs handling and fixing the core fiber, and it gets contaminated inevitably.

Table 2.3 Three methods and their trade-offs for fabrication of preform to be drawn to single-mode POFs

Methods	Polymerizing cladding around core fiber [67]	Polymerizing core within cladding hole [68]	Assembling core fiber and cladding preform [69]
Advantage	Long preform can be easily fabricated	Long preform can be easily fabricated	The fabricated fiber is step-index
Disadvantage	Two drawing processes needed: (1) core fiber drawing and (2) fiber preform drawing; Handling and fixation of core fiber in test tube is difficult; Swelling and diffusion of monomer into core during cladding polymerization; Bubbling during drawing due to residual monomer	Diffusion of monomer into cladding during core polymerization; Bubbling during drawing due to residual monomer	Two drawing process needed: (1) core fiber drawing and (2) fiber preform drawing; Assembling process needs special squeezing instrument;

A second method is to polymerize the cladding preform first, and then polymerize core in the central hole of the cladding preform [68]. The cladding preform was polymerized in a test tube fixed with a Teflon thread at the center. The Teflon thread was pulled out after polymerization so that the core could be polymerized in the remained hole. Despite of the problem of dissolving and diffusion of cladding preform by the monomers during the core polymerization, this method is preferred

over the first one because only one drawing process is required. Also, the central hole can be much smaller provided that a thin Teflon wire is used.

The third approach is to fabricate core fiber and cladding preform separately, and then assemble them together and the assembled preform is drawn to fiber. The most noteworthy feature of this method is that it completely prevents the dissolving and diffusion of core fiber or cladding preform by monomers. This guarantees the fabricated fiber is step-indexed. But the assembling process is troublesome because specially designed squeezer was necessary [69]. Instead of using two half-rounds of PMMA as cladding, Dirk and et al prepared cladding by bulk polymerization of a monomer around a thin Teflon coated wire that was held in the center of another specially prepared tube [70]. After the test tube was broken and the Teflon coated wire was pulled out, the fiber was inserted, and the whole assemble was drawn into a fiber.

2.1.3.2. *Preparing preform for microstructured POFs*

Drilling [71], casting [72], and stacking [73] are three commonly used techniques to prepare preforms for microstructured POFs (MPOFs). All these three methods are feasible to prepare single-mode POFs, though they are mostly used for fabrication of multi-mode POFs. Using the drilling technique, Zagari et al fabricated single-mode MPOFs [74]. The whole fabrication process is as follows: A number of holes with the desired pattern were drilled in a PMMA rod in diameter of 80 mm. This primary preform was drawn into a microstructured cane with an approximate diameter of 2.5 mm. The cane and some capillary tubes that surrounded the cane were then inserted into a thick-walled tube to form the secondary preform, which was drawn to the final

MPOF. The produced fibers, with a core diameter of 2.2 μm and a 570 μm cladding, were shown to be endlessly single-mode. That is, it is single-mode for the whole spectrum of light. Almost all reported single-mode POFs based on COC are microstructured, and they were drawn from preforms that have been drilled with holes in the desired pattern [42, 75-79].

MPOFs are attractive in several aspects. For example, it can be fabricated from a single polymer because the wave guiding property is achieved by the presence of holes. Moreover, the microstructure provides various possibilities for fiber design by changing the pattern of holes. However, it is difficult to make only the core of this kind of fibers photosensitive to a certain wavelength while keeping the cladding transparent and inert to the same wavelength, because the whole preform is composed of a single polymer or copolymer. Hence, traditional solid-core POFs are appropriate for investigation of grating formation because their core can be easily made photosensitive by doping while keeping the cladding transparent and inert.

2.1.4. **Heat-drawing preform to fiber**

The preform is heat-drawn to fibers by a drawing tower. Three essential parts of a drawing tower are schematically illustrated in Figure 2.3: the preform feeding unit, the heating jacket and the fiber drawing unit. To draw fiber, the preform is slowly fed into the heating jacket by the feeding unit; the preform tip is heated to melt by the jacket; the melt tip is drawn into fiber by the drawing unit and wound around a spool. In addition to these essential parts, a positive-feedback the diameter monitoring system may be added to precisely control fiber diameter. Also, a coating unit may be equipped to coat the fiber after drawing.
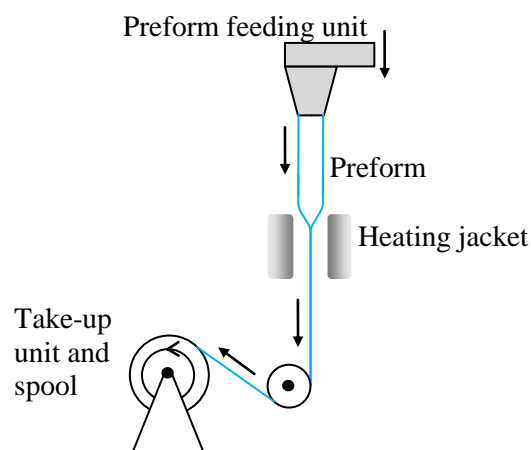
Figure 2.3 Schematic diagram of the fiber drawing tower

Many factors, including the temperature distribution of preform, the drawing force and the drawing speed, have impacts on the drawing process, hence the quality and property of resultant fibers. The preform temperature must be above its melting temperature. But too high temperature will make insufficient viscosity for drawing, and degrade the preform. The drawing force depends on the temperature-sensitive viscosity of preform polymer [80]. The drawing force has to be lower than the yield strength of the fiber, or the fiber will break. But too low force causes a detrimental variation in fiber diameter. In addition, the drawing force affects the mechanical and optical properties of fibers [12]. Though a high drawing speed is desired for fast fabrication, too high drawing speed causes the drawing process unstable, consequently leads to large diameter variation. Natural convection was found to become unsteady in the furnace and to influence heat transfer from the furnace to preform [81] and ultimately lead to large fluctuation of fiber diameter [82]. Therefore, forced convection has been adopted in commercial drawing towers.

Sophisticated drawing towers to draw high quality silica fibers are commercially available, and diameter variation can be controlled within 0.7 μm for widely used single-mode glass fiber SMF-28e in diameter of 125 μm. However, most drawing towers for polymer preform are built up by researchers and not that sophisticated [80-88], and the fabricated fibers have a large diameter variation.

2.1.5. **Fiber characterization**

The RIP and attenuation are two foremost important physical properties of optical fibers. Index profile measurement gives not only information about index distribution, but also dimensional information such as core diameter and maximum index difference.

2.1.5.1. Refractive index profile

A large number of profiling systems based on various principles have been implemented in laboratory to measure the RIP of optical fibers, as thoroughly reviewed by Stewart [89]. Stewart classified all the systems into three major groups according to their suitability for use on fibers or preforms: axial profiling techniques, transverse techniques, and non-refractive method. Axial profiling techniques, such as the reflection method and the refracted near field technique, need a flat perpendicular end on the fiber or preform. Transverse techniques reconstruct the index profile from the distorted wavefront that transversely passes through the fiber or preform, usually immersed in a refractive index matching liquid. Typical examples of these techniques include the transverse interferometry, the beam deflection technique and the light scattering method. Non-refractive techniques indirectly determine the index profile by measuring composition across the cross section of fibers.

As for POFs, the commonly used method in literature is longitudinal interferometric technique, one of the transverse techniques. This method has been used to measure the RI distribution of the preform to draw graded-index POFs [90, 91]. This interferometric technique was previously used to measure the radical distribution of the RI in light-focusing rods [92], which were fiber preforms essentially. It has also been used to measure the RIP of POFs, and to determine the birefringence induced during drawing process [93].

2.1.5.2. Attenuation of POFs

High attenuation is one of key problems associated with the single-mode POFs, especially for PMMA based fibers in the infrared range, as shown in Table 2.4. PMMA based fibers have a loss of up to 100 dB/m for 1300 nm or 1550 nm. This attenuation level is close to absorption loss of PMMA, which is about 50-100 dB/m within 1300-1500 nm range [94]. Loss at 1300 nm and 1550 nm is specially concerned here because most PFBGs operated at these two wavelength ranges, although great efforts are being taken to write PFBGs at shorter wavelengths [28, 30]. The attenuation of single-mode PMMA based POFs fabricated by Teflon-wire method was reported to be about 10 dB/m at 650 nm [95], which is almost two orders of magnitude higher than that of multi-mode PMMA fiber [96], This large difference in loss suggests that POFs fabricated by Teflon-wire method have extremely high scattering loss, and this high scattering loss mainly originates from the interface between the fiber cladding and core. The issue of high attenuation is also associated with COC based POFs [33].

Table 2.4 Attenuation of single-mode and few-mode POFs compared multi-mode ones

Fiber specification	Attenuation
Multi-mode fiber with PMMA core [97]	0.1 dB/m at 522, 570 nm 0.2 dB/m at 650 nm
Single-mode PMMA fiber doped with 0.1 wt% dye(ISQ or TSQ) [69]	20-40 dB/m at 1064 nm ~30 dB/m at 1300 nm
Fiber of PMMA core doped with 2500 ppm Rhodamine B [95]	100 dB/m at 650 nm
Single mode POF with perfluorinated core [36]	0.2 dB/m at 1410-1540 nm 0.5 dB/m at 1610 nm
Few-mode fiber of PMMA core doped with dye (1 wt% ISQ or DR1) [68]	20-60 dB/m at 1300 nm
Step-index, single-mode POF with polystyrene doped PMMA core (MORPOF02 of Paradigm Optics) [28]	450-600 dB/m within 700-850 nm
PMMA MPOF [28]	5-20 dB/m within 700-850 nm
Single-mode PMMA fiber [67]	5 dB/m at 850 nm 20 dB/m at 1550 nm
PMMA based POF [98]	100 dB/m around 1550 nm
Multi-mode PMMA fiber [96]	0.10 dB/m at 650 nm SI POF 0.16 dB/m at 650 nm for GI POF
Fiber based on COC (TOPAS COC 5013) [33]	50 dB/m at 800 and 1300 nm 70 dB/m at 1550 nm

One way to reduce the attenuation of the fiber is to use perfluorinated polymer fiber instead of PMMA. Zhou et al drew single-mode perfluorinated polymer optical fiber from commercial multimode perfluorinated POF, and the transmission loss was less than 0.2 dB/m in the wavelength range of 1410-1540 nm and less than 0.5 dB/m for wavelengths up to 1610 nm [36].

2.1.5.3. *Impact of annealing on POFs*

Annealing treatment has various impacts on POFs, including its optical and mechanical properties. Annealing POF can relieve the frozen-in stress induced by the drawing process [12], and thus remove the birefringence caused by residual stress in

POFs [93]. Yuan et al studied the thermal response of FBGs written in commercial POFs, and they found that annealing treatment on POFs could improve short-term performance at high temperature and large strain, and the operation temperature and strain range of FBGs in PMMA fibers were also extended by the annealing process [27]. Annealing PMMA based MPOFs extended temperature sensing range [99], though increased its loss [100]. Annealing treatment reduced the stress-optic coefficient of PMMA fibers, but also had a significant impact on the dependence of the stress-optic coefficient on drawing tension [35]. Annealing (80 ℃ for 7 h) of PFBGs fabricated in microstructured PMMA fiber resulted in a Bragg wavelength shift of -22 nm [79]. Jiang et al found that when annealed at 95 ℃, dye doped PMMA fibers decreased in length and increased in diameter. The annealed fiber had a higher ductility but a lower strength than those without annealing [12].

2.2. **Inscription of PFBGs**

Table 2.5 lists reports on inscription of PFBGs in various POFs, including the specifications of the used POFs and the writing conditions. Obviously, almost all POFs are made of PMMA or TOPAS COC, and the phase mask technique is the most commonly used method.

The phase mask technique and the holographic technique are two common methods to write FBGs in fibers. Phase masks, also called phase-shift masks, are photomasks that form interference patterns with high resolution by taking advantage of the phase difference between lights diffracted by the masks. The phase masks used for writing FBGs are designed so that most of the incident light is diffracted into the first order, and two beams in the first diffraction order intersect and produce interference

patterns with a period equal to half of the phase mask pitch. When photosensitive fibers are placed in the interference pattern, the RI of fiber cores will be modulated periodically to form FBGs, as shown in Figure 2.4. One of the major advantages of the phase mask technique is its simplicity of optics alignment. Moreover, the stability requirement for writing systems is not as stringent as the holographic method. One of the drawbacks of the phase mask technique is that many phase masks with different pitches are needed to fabricate FBGs at various wavelengths, because one mask can only inscribe FBGs at one specific wavelength.

Table 2.5 Fiber specifications and writing conditions of reported inscriptions of PFBGs

Reference	POF specification	Writing method and conditions
[23]	Core: copolymer of methyl methacrylate, ethyl methacrylate (EMA) and benzyl methacrylate (BzMA) doped with 0.66% TS Fiber core diameter ~20 μm, cladding 250 μm	Phase mask technique 325 nm dye laser, plused, 10 Hz, power 10 mW Writing time 10 min, grating length 11 mm (scanned) Reflection peaks observed in transmission spectrum
[38]	Few-mode MPOF: the core was surrounded by 60 holes with diameters of 5.5 μm and a separation of 10 μm. Core diameter 13 μm	Phase mask technique Continuous wave 325 nm He-Cd laser (KIMMON IK5625R-G); 30 mW laser beam focused on fiber
[42]	Microstructured POF based on COC (TOPAS 8007-F-04); Single mode at 1550 nm	Phase mask technique Continuous wave 325 nm He-Cd laser (KIMMON IK3301R-G); 30 mW laser beam focused on fiber; The grating saturated after 45 min
[27, 28]	PMMA MPOF Polystyrene doped PMMA fiber (MORPOF02, Paradigm Optics)	Phase mask technique CW He-Cd laser (KIMMON IK5751I-G) Gratings at 850 nm and 1550 nm Writing time is more than one hour.
[30]	Multimode microstructured POF based on PMMA (Kiriama Pty. Ltd.)	Phase mask technique; CW He-Cd laser Gratings at 827 nm are written

Table 2.5 Fiber specifications and writing conditions of reported inscriptions of PFBGs (Continued)

Reference	POF specification	Writing method and conditions
[78]	Single-mode, microstructured POF based on COC	Phase mask technique CW He-Cd laser (KIMMON IK5751I-G)
[101]	PMMA based step-index POF with two eccentric cores (8.1 μm)	Phase mask technique Continuous wave 325 nm He-Cd laser (KIMMON IK5625R-G) 30 mW laser beam focused on fiber
[102, 103]	Single-mode, step-index POF (MORPOF05, Paradigm Optics) 3.4 μm core composed of copolymer of MMA and styrene	Phase mask technique 308 nm Xe-Cl excimer laser; Pulse laser, 5 Hz Irradiation within 30 to 60 min
[65]	PMMA fiber doped with benzildimethylketal	The modified Sagnac optical ring system (interferometric technique) 355 nm frequency-tripled Nd:YAG laser, pulsed (5 Hz, 6 ns pulse width)
[19]	Single mode POF The fiber core is composed of copolymer of MMA, EMA and BzMA	The modified Sagnac optical ring system (interferometric technique) 355 nm frequency-tripled Nd:YAG laser, pulsed (5 Hz, 6 ns pulse width)
[104]	Single mode POF; The fiber core is composed of BDK (2 wt%) doped the copolymer of MMA, EMA and BzMA	The modified Sagnac optical ring system (interferometric technique) 355 nm frequency-tripled Nd:YAG laser
[63]	PMMA based POF Copolymer core doped with 3.2 wt% azobenzene, 6 μm in diameter	Interferometric technique; 441.3 nm He-Cd laser Seventh order Bragg reflection (Birefringence grating) at 632.8 nm observed
[26]	~21 μm core of copolymer of MMA and butyl acrylate (BA) doped with 9.6 wt% BDK	Modified Sagnac system, 355 nm pulse laser, 10 Hz, 6 ns; Intensity 153 mW/cm^2
[29]	MORPOF03 (Paradigm Optics)	Phase mask technique, Xe-Cl laser at 308 nm laser, gratings around 980 nm
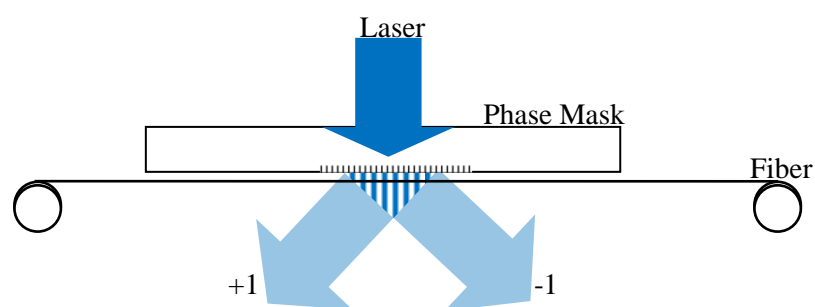
Figure 2.4 Schematic diagram of the phase-mask technique for photo imprinting a refractive-index Bragg grating in a photosensitive optical fiber [3]

The phase mask technique has been used by most research groups to write Bragg gratings in POFs. Webb et al adopted phase mask technique to write FBGs in microstructured polymer fiber, including PMMA based fiber [38] and polyolefin based fiber [42]. Instead of placing a phase mask directly on polymer fiber, they found that there should be a certain distance between the phase mask and fiber, and the optimal distance was 80 μm [105]. Previously our research group reported fiber grating written in TS doped PMMA fiber [23, 50, 51], and the writing system was also the phase mask technique.
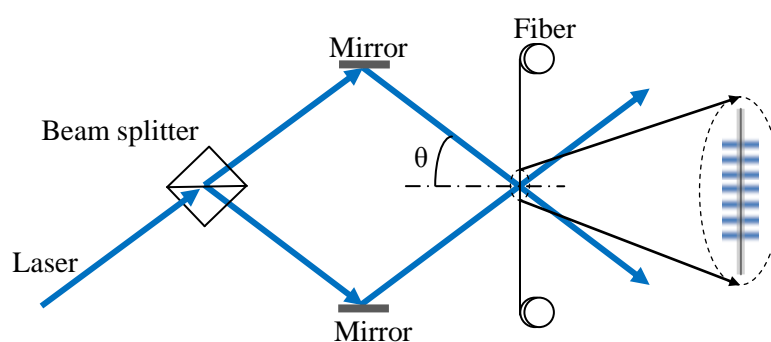
Figure 2.5 Schematic diagram of the holographic technique for the inscription of FBGs. A beam splitter is used to separate laser beam here, but one phase mask might be used instead.

The holographic technique is also called the interferometric technique, because photosensitive fibers are placed in the interferometric field produced by two intersecting coherent laser beams. As shown in Figure 2.5, the input beam is split into two beams by a beam splitter, and two separated beams are then reflected by two mirrors to intersect and form interference pattern. As the photosensitive fiber is placed in the interference pattern, a FBG can be written in fiber. The superiority of the interference system is its tunability on the period of the interference pattern and

the period of FBGs written in fiber. The period can be altered by adjusting the intersecting angle, which determines the period of the interference patterns. This means one interference system can write FBGs with various Bragg wavelengths. This writing system, however, uses more optics including one beam splitter and two mirrors, and is severely influenced by the instability of system.
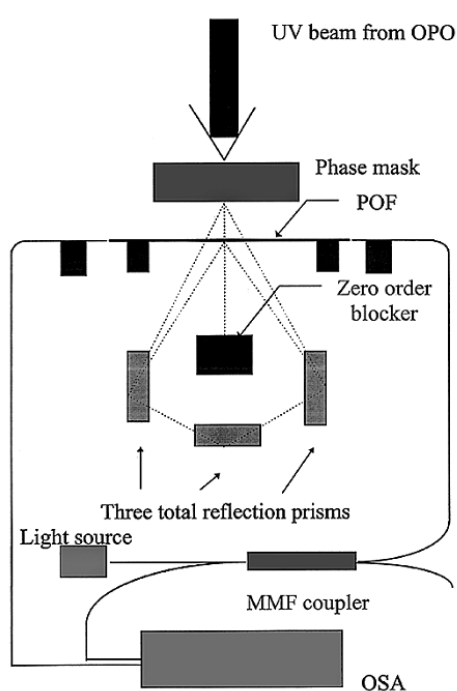
Figure 2.6 The grating writing system used by Peng et al [19]. During experiment, the intersecting point of reflected +1 and -1 order beam is on the phase mask, but not at the exact point where incident beam diffracts. By this configuration, the intersecting angle is almost the same as the diffraction angle of the phase mask used, so that the period of interferometric pattern is half of phase mask pitch.

By employing a modified Sagnac interferometer (Figure 2.6), Peng et al successfully wrote PFBGs in PMMA based fibers [19, 20]. Bragg gratings were created by shining a 325-nm UV beam to the fiber through three quartz prisms. These prisms constituted a modified Sagnac interferometer where the two first-order diffraction beams formed the required interference pattern for the grating. The primary reason of applying this configuration was to avoid the influence of zeroth order diffraction of phase masks, as even small amount of zeroth order diffraction was found to change

the near-field of phase masks dramatically [106]. The operating wavelength of the phase mask they used was 248 nm, but the suitable wavelength for writing grating locates at 325 nm. Hence the zeroth order diffraction of the phase mask needed to be blocked. Although a phase mask was used in this writing system, it was essentially an interferometric technique, since the fiber was placed in the interference pattern of two reflected beams. As discussed earlier, this method requires highly stable writing system, and also precise alignment of optics components.

Despite different writing systems and conditions, most fabricated PFBGs have central wavelength in the range of 1500~1600 nm. For polymer fibers, attenuation at this range is between 50-100 dB/m (Table 2.4), consequently only a very short fiber of a few centimeters was allowed to be used for grating writing.

2.3. Properties of PFBGs

For sensor applications, two most important properties of PFBGs are their temperature and strain response.

2.3.1. Thermal response

One of the highly claimed features of PFBGs compared with silica FBGs is its high temperature sensitivity thanks to the large thermo-optic coefficient, and this has been shown by many experimental results (Table 2.6). Liu et al created PFBGs in PMMA based fibers and thermally tuned them, and found that the tuning range was more than 18 nm over a temperature variation of 50 ℃, and no hysteresis effect was observed as the gratings were heated up and cooled down [107]. Temperature sensitivity of lower value -149.5 pm/℃ was also reported [108]. Carroll et al tested

PFBGs fabricated in MPOFs based on PMMA, obtained temperature sensitivities from -52 pm/℃ to -95 pm/℃ [99]. A similar value was obtained for the TS doped MPOF [105]. Chen et al measured the thermal response of PFBGs at 1562.5 nm in step-index POFs, and the temperature sensitivity was measured to be -50.1 pm/℃. PFBGs in single-mode POFs with a core doped with polystyrene is also tested to have a temperature sensitivity of -98 pm/℃ before annealing and -109 pm/℃ after annealing [27]. Despite large variation in all these measured values, they were still much higher than that of silica FBGs, which is about 10 pm/℃ [109].

Table 2.6 Experimental values of the temperature sensitivity of PFBGs

POF Specification	Grating peak (nm)	Sensitivity (pm/K)	Reference
Copolymer of styrene and MMA (Paradigm, MORPOF02)	1535	-10 (*in dry condition*) -34.9 (in water) -138 (ambient)	[103]
Step-index PMMA fiber	1562	-50	[101]
the core is made of MMA/EMA/BzMA doped with 2 wt% BDK	1569	-149	[110]
POF based on PMMA	1538	-149	[108]
POF based on PMMA	1542	-55	[98]
Single mode microstructured POF of COC	870	-60	[78]
PMMA based MPOF	1560	-52 to -95	[99]
MORPOF02	1553	-109 (before annealing) -98 (after annealing)	[27]
MMA/EMA/BzMA copolymer core	1580	-360 (-18 nm over 50 ℃ change)	[107]
COC based MPOF	1603	810	[77]
COC based MPOF	1568	-36.5 (*at constant RH 55%*)	[42]
PMMA based POF	1567	-43 (*at constant RH 45%*)	[37, 111]
COC based MPOF	849	-78	[112]

Theoretically, Bragg wavelength shift of FBGs due to temperature change is given by

$$\frac{\Delta\lambda}{\lambda} = (\alpha_n + \alpha_\Lambda)\Delta T \tag{2-1}$$

Where α_Λ is the coefficient of thermal expansion (CTE), and α_n is the normalized thermo-optic coefficient $\frac{dn}{dT}/n$, which is the thermo-optic coefficient dn/dT divided by the effective refractive index n.

The reported values for α_Λ and dn/dT of PMMA vary substantially, as shown in Table 2.7 and Table 2.8. The values for α_Λ ranges from 0.5×10^{-4} to 0.9×10^{-4} $℃^{-1}$, and dn/dT from -0.91×10^{-4} to -1.2×10^{-4} $℃^{-1}$. When α_Λ is assumed to be 0.5×10^{-4} $℃^{-1}$ (the lowest value) and dn/dT -1.2×10^{-4} $℃^{-1}$ (the largest absolute value), the specific sensitivity (theoretically largest) of the PFBGs in PMMA fiber is -0.31×10^{-4} $℃^{-1}$. Accordingly, the absolute sensitivity is -47, -40 and -27 pm/ ℃ for 1550, 1300 and 900 nm Bragg wavelengths, respectively. These values are lower than most experimental values in Table 2.6, and the difference most likely originates from the impact of humidity on PFBGs in PMMA based fibers [103].

Table 2.7 Reported values for CTE of PMMA

Reference	CTE ($\times10^{-4}$ $℃^{-1}$)	Notes
[31]	0.58 at 0 ℃	Plexiglas 55 used.
	0.68 at 20 ℃	Humidity control not
	0.81 at 40 ℃	mentioned.
[113]	0.84 below T_g	Measured on thin film
[114]	0.5 – 0.9	Test method: ASTM C177
[115]	0.7-0.8	-

Table 2.8 Reported values for dn/dT of PMMA

Reference	Thermo-optic coefficient dn/dT ($\times 10^{-4}$ $°C^{-1}$)	Notes
[31]	-0.91 at 0 °C -1.05 at 20 °C -1.23 at 40 °C	Plexiglas 55 used; 633 nm Humidity control not mentioned.
[34]	-1.2 (-23 °C to 90 °C)	PMMA prism (Altuglas) Sample heated via N_2 flow 578 nm
[116]	-0.85	Plexiglas 55
[117]	-1.1	Spin coated PMMA film (PL polymer lab), 633 nm

2.3.2. **Strain response**

The Bragg wavelength shift of FBGs upon applied strain along the fiber axis is governed by

$$\frac{\Delta\lambda}{\lambda} = (1 - p_e)\epsilon \qquad (2\text{-}2)$$

Where ϵ is the applied strain along fiber axis, and p_e is the effective strain-optic coefficient determined by

$$p_e = \frac{n^2}{2}[p_{11} - \nu(p_{11} + p_{12})] \qquad (2\text{-}3)$$

Where n is the effective refractive index of the core; p_{11} and p_{12} are components of the strain-optic tensor.

For PMMA at 633 nm, measured p_{11} and p_{12} are 0.300 and 0.297, respectively [31]. If n and ν are assumed to be 1.49 and 0.3, respectively, p_e is estimated to be 0.13. Accordingly, the specific strain sensitivity $(\Delta\lambda/\lambda_B)/\varepsilon$ is calculated to be 0.87 (pm/μm)/με. Hence, the sensitivities at 900, 1300 and 1500 nm are 0.8, 1.1 and 1.3 pm/με, respectively.

Table 2.9 Reported strain sensitivity of PFBGs

Fiber	Grating peak (nm)	Strain sensitivity (pm/με)	Reference
Step-index PMMA fiber	1562	1.13	[101]
MORPOF02, copolymer core (MMA/Styrene)	1553	1.37 (before annealing) 1.3 (after annealing)	[27]
POF based on PMMA	1538	1.48	[108]
PMMA based POF	1535	1.46	[118]
PMMA based MPOF MORPOF02	1550nm, 850 nm	1.3 at 1550 nm 0.71 at 850 nm	[28]
Single mode microstructured POF of COC	870	0.64	[78]
Multimode POF; Core is copolymer of MMA and BA doped with BDK	1572-1576	1.2	[26]

The experimental values of strain sensitivity for PFBGs are tabulated in Table 2.9. It is evident that there are big differences among these values, and most values are inconsistent with the theoretical values. The inconsistence between theoretical and experimental values is mainly caused by variation in molecular structures and morphology. The values of p_{11} and p_{12} used for calculation are for the bulk isotropic PMMA in which macromolecules aggregate randomly, however, macromolecules in POFs are oriented along fiber axis due to drawing. This ordered structure has major effect on the strain-optic tensor [119]. That is to say, values of p_{11} and p_{12} for bulk PMMA and POFs are different. And also, the large deviation between experimental values is also due to the fact that most fibers in Table 2.9 are drawn without tension control.

Though the strain sensitivity of PFBGs is not much larger than that of silica FBGs, the strain range of PFBGs is much wider than the later due to the material nature. The elongation to break for PMMA fiber is close to 30%, and yielding strain is about 5% [12].

2.4. **Applications of PFBGs**

Although the mass production of PFBGs has not been realized yet, a certain number of promising applications using PFBGs have been demonstrated.

2.4.1. **Wavelength-tunable filter**

It was reported that by coating a thin metal film on the surface of POF in which a PFBG were written, researchers were able to electrically tune the Bragg wavelength of the PFBG by applying an electric voltage on the metallic coating and the grating acted as a wavelength-tunable filter [16, 17]. Optically tuning was also demonstrated later, that is, a pumping light was launched into the fiber and absorbed, and absorption resulted in the temperature change of the fiber, hence Bragg wavelength change of PFBGs in the fiber [120]. The superiority of optical tuning over electrical counterpart is that optical tuning can be controlled remotely. Although optically tuning was claimed, the filter involved optical-thermal effect. Fully optically tuning can be realized by doping the fiber core with dopant that photoisomerizes [121, 122]. Bragg gratings were written in the fiber with the interference pattern of two coherent laser beams of 500 nm via photochromic effect. The fabricated gratings could be removed by irradiating them with UV light and the inscription and erasing process could be repeated.

2.4.2. **Flexible sensing skin**

The flexible skin embedded with PFBGs was reported 10 times more sensitive to pressure than those with gratings in silica fibers [123, 124]. The strain sensitivity of PFBGs embedded in flexible skin was 45 times higher than that of silica fiber in spite

of their similar intrinsic strain sensitivity. The main reason for this sensitivity enhancement was the lower Young's modulus of polymer fiber (~2 GPa) than silica fiber (~70 GPa). When embedded in flexible skin, POFs have much larger strains induced by deformation of the skin, resulting in higher sensitivity.

2.4.3. Textile health monitoring

Health monitoring of old tapestries is of great interest to conserve cultural heritage. Ye et al attached PFBGs, also silica ones, to a woven textile and use them to measure the strain in textile [125]. They found that PFBGs provided improved strain transfer coefficients and reduced concentration of stress on fiber compared to silica FBGs, and therefore made a more suitable solution for textile monitoring. The reason was also due to lower Young's modulus of polymer fibers than silica fibers.

2.4.4. Tunable laser

Using PFBGs as the reflection mirror and wavelength selector, Liu et al fabricated a tunable fiber ring laser, and the tuning range was as broad as 35 nm by simply applying an axial strain on the fiber [126, 127], which was more than 3 times larger than the typical value that can be achieved using silica FBGs, namely, 11 nm [128].

2.4.5. Acceleration sensor

Stefani et al designed a transducer that converted acceleration to the strain of the polymer fiber written with PFBGs [129]. The fabricated sensor exhibited a sensitivity of 20 pm/g up to acceleration of $4.5g$. In addition, the frequency response was better than silica FBGs.

2.4.6. **Mesoscale photomechanical unit**

FBGs are typical examples of so-called mesoscale photomechanical unit (MPU) [130], and they are essential building blocks to realize all-optical devices in POFs, for example, grating based interferometric devices [131].

2.5. **Summary**

This chapter reviewed the research on PFBGs, including the fabrication of photosensitive single-mode POFs, the inscription and characterization of PFBGs, and also some emerging applications of PFBGs. Five common polymers were compared, and PMMA was selected to fabricate POFs for its easy fabrication and modification. To make the POFs photosensitive, doping POFs with photosensitive organics was necessary. Several dye dopants were compared, and TS was found more preferable than others because of the non-degradation mechanism, that is, PFBGs was formed by RI modulation induced by its photoisomerization rather by decomposition or degradation of the core polymer. Hence, this study will investigate the formation process of Bragg gratings in PMMA based POFs doped with TS. On the basis of comparison between three major approaches to fabricate preform for single-mode POFs, the Teflon wire method was adopted.

The proposed mechanism of Bragg grating formation in TS doped PMMA fibers was RI modulation induced by its photoisomerization upon UV irradiation. However, the real formation process has not been studied and preliminary experimental observation suggests more laser-induced processes involved. Hence, the investigation of the grating formation process in this fiber will be the central topic of this study. A large number of reports on fabrication of PFBGs were closely examined,

and the phase mask was found more common than the holographic method for its simplicity in the writing system, despite of the issue of the zeroth order diffraction of phase masks.

The theoretical estimation and experimental values of the temperature sensitivity and strain sensitivity of PFBGs were compared and analyzed. It was found that most experimental values of temperature sensitivity were higher than the largest value predicted by theory. The inconsistence seemingly comes from the impact of humidity on PFBGs, and hence the humidity response of PFBGs will be investigated after successful inscription.

Some promising applications using PFBGs were summarized, including tunable wavelength filter, flexible sensing skin, textile health monitoring, acceleration sensor, and MPU. Compared to silica FBGs, PFBGs exhibited superiority because of the lower Young's modulus and larger strain sensing range of POFs.

CHAPTER 3 PHOTOSENSITIVITY STUDY OF TS-DOPED PMMA FILMS

This chapter investigates the photosensitivity of the material system that is used as the core of POFs, namely, TS doped copolymer based on MMA. Bragg reflection of the grating written in the fiber with the same core material system was demonstrated in our laboratory previously [49]. However, at the very start of this thesis study, for quite a time, all attempts to write and observe Bragg gratings in the fabricated POFs failed. To find the origin of the failure, the process of the fiber fabrication was investigated in great detail, and the effects of the grating writing systems are examined. In addition, the photosensitivity of the fiber core system is re-examined. The photosensitivity of the fiber core system is confirmed in the film from two aspects: (1) the reduction of RI of the film after irradiation by UV laser; (2) existence of the volume holographic gratings written in the film, including both Bragg type and long period ones.

3.1. Experiment

3.1.1. Chemicals and purification

Methyl methacrylate (99% purity), ethyl methacrylate (99% purity), benzyl methacrylate (96% purity), *trans*-4-stilbenemethanol (95% purity), sodium hydroxide, sodium sulfide, calcium hydride (95%), lauroyl peroxide and 1-buthanethiol (99% purity), 1,2-dimethoxyethane (99% purity), sulfuric acid (96% purity), and hydrogen peroxide (30% aqueous solution) were all bought from International Laboratory USA

(ILUSA). Three monomers—methyl methacrylate, ethyl methacrylate and benzyl methacrylate—were washed by sodium sulfide aqueous solution to remove inhibitor, then dried by sodium sulfide, and further residual moisture were completely removed by calcium hydride. The detailed procedure can be found in Chapter 4. All the others were used as purchased.

3.1.2. **Preparation of films on glass slides**

The first step was to polymerize a fiber core preform. Methyl methacrylate (18.02g, 0.18 mol), ethyl methacrylate (0.91g, 0.008 mol) and benzyl methacrylate (2.11g, 0.012 mol) were mixed, in which initiator lauroyl peroxide (24 mg, 0.06 mmol), transfer agent 1-butanethiol (54 μL), and *trans*-4-stilbenemethanol (0.15g, 0.7 mmol) were added. The solution was poured into a test tube, which was gently shaken for complete dissolution. Then the test tube was placed in an oil bath, and heated at 65 ℃ for 2 h, then 60 ℃ for 10 h, 70 ℃ for 36 h, 80 ℃ for 8 h, 90 ℃ for 8 h, 100 ℃ for 8 h, 110 ℃ for 12 h, and finally 115 ℃ for 12 h. After polymerization, the test tube was scratched using a glass knife and broken to obtain the core preform, which was drawn to a core fiber on the fiber drawing tower.

Thin films were spin-coated on glass slides. Silicon wafers were also used and compared in some experiments, but the RI of the film made on both substrates was found to be the same. Prior to spin coating, the glass slides and silicon wafers were immersed in the mixture of sulfuric acid (30 mL of aqueous solution at concentration of 98%) and hydrogen peroxide (10 mL of aqueous solution at concentration of 30%), rinsed by deionized water and dried in oven. The core fiber was cut into small pieces and dissolved in 1,2-dimethoxyethane at a concentration of 10% g/g. Finally, the

core fiber solution was dropped on the glass slide or silicon wafer that was attached on the rotator of a spin coating machine. The spin coating speed and time were set to be 1000 rpm and 60 s, respectively. After spin coating, the substrate was detached and dried in a drying oven at 90 ℃ for 10 h. The thickness of resultant films is about 2 μm, which is measured by the Prism coupler described in 3.1.4.

Thick films were formed by casting the core fiber solution on a glass slide. The glass slide was tilted in all directions so that the solution covered a large area, and then the slide was placed on a flat surface in a fume hood to let the solvent evaporate overnight. Finally the film on the slide was dried under the same drying conditions for the thin films.

3.1.3. **Preparation of sandwiched films**

The polymerization solution was prepared as described in section 3.1.2 and poured into a test tube. Rather than fully polymerize the solution in the tube, the tube was prepolymerized at 90 ℃ for 2 h in an oil bath. After the temperature of the solution dropped to the room temperature, a few dips of the prepolymerized solution were dropped on a cleaned glass slide, and covered by a cover glass (about 0.1 mm in thickness). The glass slide was then placed on a hot plate and heated at 90 ℃ for 12 h, then 100 ℃ for 12h to complete the polymerization.

3.1.4. **Refractive index measurement**

RI of the film on glass slides or silicon wafers was measured on a Prism Coupler (Metricon 2010). In addition to RI, this instrument also provides the thickness of the measured film. The resolution and accuracy of the RI measurement are 0.0003 and

0.001, respectively. It also should be aware that the wavelength of laser used in measurement is 632.8 nm, whereas the operating wavelength of the final PFBGs written in POFs is around 960 nm, 1300 nm and 1550 nm. Therefore, dispersion should be considered when calculating the Bragg wavelength of PFBGs. As for PMMA, its RI at 632.8, 1310, and 1550 nm are 1.489 [132], 1.485 (d-PMMA) [133] and 1.481 [134], respectively.

3.1.5. **UV laser**

Two UV laser systems were used: an optically pumped, pulsed dye laser (Sirah CSTR-G-18) and a continuous-wavelength 325-nm He-Cd laser (Kimmon, IK3802R-G). The He-Cd laser was chosen for most the experiments thanks to its greater stability in wavelength and power stability than the dye laser. Nevertheless, the dye laser was used in the photosensitivity study of this chapter. The dye laser is pumped by a 532 nm laser emitted from a frequency-doubled Nd:YAG laser (Spectra-physical Lab-170-10). The dye laser generated a 325 nm pulsed radiation of 10 Hz with a pulse width of 8-10 ns. Its beam size is about 2 mm $\times$ 4 mm. The laser medium was the solution of DCM (4-dicyanomethylene-2-methyl-6-(p-dimethylaminostyryl)-4H-pyran)) in ethanol. Specifications of the He-Cd can be found in Appendix 1.

3.1.6. **Irradiation of thin films by UV laser**

Thin films on glass slides were irradiated by the dye laser to study the impact of irradiation on the RI of films. The beam was expanded using a plano-convex lens with two purposes: (1) to enlarge the beam size to facilitate RI measurement; (2) to

control irradiation intensity by varying the distance from the lens to the film to irradiate.

3.1.7. **UV absorption measurement**

The core fiber was dissolved in 1,2-dimethoxyethane, and the UV absorption spectrum of the solution was measured on an UV-Vis spectrometer (PERKIN ELMER Lambda 18).

3.1.8. **Film grating fabrication**

Bragg gratings were written in the thin films on glass slides and those sandwiched by using two writing methods: (1) phase mask technique; (2) interferometric technique. The phase mask technique was quite simple (Figure 2.4), that is, the phase mask was placed on the film (on cover glass for sandwiched films), and the film was irradiated by 325 nm He-Cd laser (Kimmon, IK3802R-G) through the phase mask. The interferometric system, as shown in Figure 2.5, except that the beam splitter was replaced by a phase mask to separate the laser beam, was also built to write Bragg gratings in the sandwiched films. The diffraction of the fabricated Bragg gratings was observed by use of a red laser (Research Electro-Optics, Inc. R-30990) or a green one (Photop Suwetech, Inc. DPGL-3005F).

Long period gratings were written in both kinds of film (on glass slides and sandwiched ones) by irradiating the film placed beneath an amplitude mask (copper, 375 μm), and their formation in films were checked by their diffraction using the red laser.

3.1.9. **Atomic force microscope**

An atomic force microscope (AFM; Metris-200, Burleigh Instruments Inc.) was used to examine the surface morphology of gratings written on spin-coated films on glass slides.

3.2. **Result and Discussion**

3.2.1. **Refractive index change of TS doped film under UV irradiation**

Figure 3.1 shows the RI of a thin film doped with 7 wt % TS irradiated by the 325 nm dye laser at an irradiance of 5 mW/cm^2, and dependence of the index on the radiant exposure. The index drops abruptly within the first few seconds, and then the reduction speed becomes slow and stabilizes at the minimum value after two minutes irradiation. Abrupt reduction in RI at start of irradiation is due to the high initial dopant concentration, and hence high absorption and photoisomerization speed. After most trans molecules isomerizes, the photoisomerization speed decreases because most photon transit through the film without absorption.
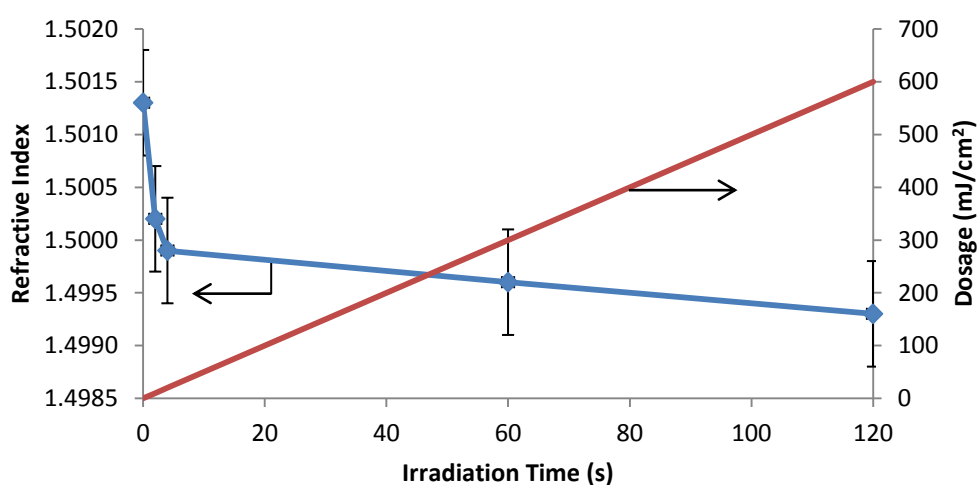
Figure 3.1 The RI of a 1.5 μm film doped with 7 wt % TS after irradiation for different irradiation durations (dye laser used, irradiance 5 mW/cm^2).

To get a general idea about the magnitude of the radiant exposure and to estimate the irradiation time needed to achieve 100% photoisomerization from trans to cis (less than 100% in reality), the ideal minimum radiant exposure can be roughly estimated on the basis of the following assumptions: (1) Only trans molecules absorbs the irradiation laser, and one TS molecules absorbs only one photon without other photoreactions; (2) All photos radiated on the film are absorbed and all absorption leads to trans-cis isomerization; (3) Dopant in cis configuration does not thermally isomerizes back to trans. Then, the following equation is formed for the film of a unit square centimeter:

$$N_c = N_{t0} - N_t = \frac{\eta \, \varepsilon_t \, H_e}{h\nu \, N_A} \tag{3-1}$$

Where N_c and N_t are the area density (mol/cm^2) of the cis and trans dopant in the film, respectively, and N_{t0} is the initial value for the film before irradiation; H_e is the radiant exposure (mJ/cm^2) on the film; ε_t is percentage of photons that are absorbed by the film among all photons radiated on the film; η is the quantum efficiency, that is, the percentage of the excited trans configuration that photoisomerizes; h is Plank constant and ν is the laser frequency, and $h\nu$ is the photo energy; and N_A is the Avogadro constant. Due to the absorption of the laser by the dopant and continuous photoisomerization, N_c, N_t, H_e and ε_t are time-dependent, moreover, N_c, N_t, and ε_t also varies along the irradiation direction. To calculate the ideal minimum radiant exposure to transform all trans dopants to cis, the equation can be treated in a simplified way. After complete trans-cis photoisomerization, N_t reduced to zero, and N_c is equal to N_{t0}. Therefore, the minimum radiant exposure can be calculated by rewriting the equation 3-1:

$$H_\mathrm{e} = \frac{h\nu\, N_A\, N_{t0}}{\eta\, \varepsilon_t} \qquad (3\text{-}2)$$

Both η and ε_t are 100% based on the assumption. The initial value N_{t0} is determined

by the film thickness (l, in cm), dopant concentration (C, in wt %), film density (ρ,

approximately equal to that of PMMA 1.2 g/cm^3), and molecular weight of TS (M_w,

210.3 g/mol).

$$N_{t0} = \frac{l\, \rho\, C}{M_w} \qquad (3\text{-}3)$$

As for the film studied in Figure 3.1, whose thickness and dopant concentration are

1.5 μm and 7 wt %, respectively, the ideal minimum radiant exposure to transform

all trans molecules to cis in the film is calculated to be 20 mJ/cm^2. Based on this

value, radiation time can be estimated for specific irradiance, i.e. four seconds is

needed for irradiance of 5 mW/cm^2. Experimentally, η and ε_t must be less than

100%, and the conversion ratio of trans-cis is less than 100%. Taking into the

account of this, much long time is needed to achieve complete conversion. However,

total conversion is not practical and also not necessary because irradiation of too high

power or long time exposure is required. Nevertheless, experimental value of radiant

exposure is normally at least two orders of magnitude larger than the ideal minimum

value to ensure maximum conversion.

Table 3.1 lists refractive indices of TS doped poly(MMA/BzMA/EMA 90/4/6 mol%)

film before and after UV laser irradiation for TS concentration with 0-7.0 wt % . To

achieve high conversion, the film is irradiated at high irradiance (117 mW/cm^2) for

prolonged time (300 s). The absolute RI of the films increases as raising TS

concentration—about 2×10^{-3} RIU increase per 1 wt% concentration increase. The RI

reduction induced by laser irradiation also linearly increases as raising TS concentration, about 4×10^{-4} RIU reduction for 1.0 wt % TS (Figure 3.2). This value is fairly consistent with previous results [23, 51]. Tao et al report a change of -24×10^{-4} in RI of the 5 wt % of TS doped films (4.8 μm) made of the same copolymer irradiated by 325 nm laser (28 mJ/cm^2 pulse energy, 10 Hz) for one minute [51]. Using a UV lamp, Yu et al irradiate 1.0 wt % of TS doped poly(MMA/EMA/BzMA 90/4/6 mol%) films, and observed a drop of 3×10^{-4} in RI for 1.0 wt % TS (9×10^{-4} for 2.0 wt % TS) [23]. All of these data confirm that the RI of the TS doped films can be modulated by UV irradiation, even by UV lamps.

Table 3.1 RI change of TS doped poly(MMA/BzMA/EMA 90/4/6 mol%) film of 3.2 μm in thickness (Irradiance 117 mW/cm^2; irradiation time 300 s)

TS concentration (wt %)	RI Before Irradiation (TE mode)	RI After Irradiation (TE mode)	RI Modulation
0.0	1.4882	1.4882	0
0.7	1.4897	1.4894	-0.0003
1.8	1.4920	1.4914	-0.0006
3.0	1.4943	1.4930	-0.0013
5.0	1.4985	1.4967	-0.0018
7.0	1.5013	1.4984	-0.0029
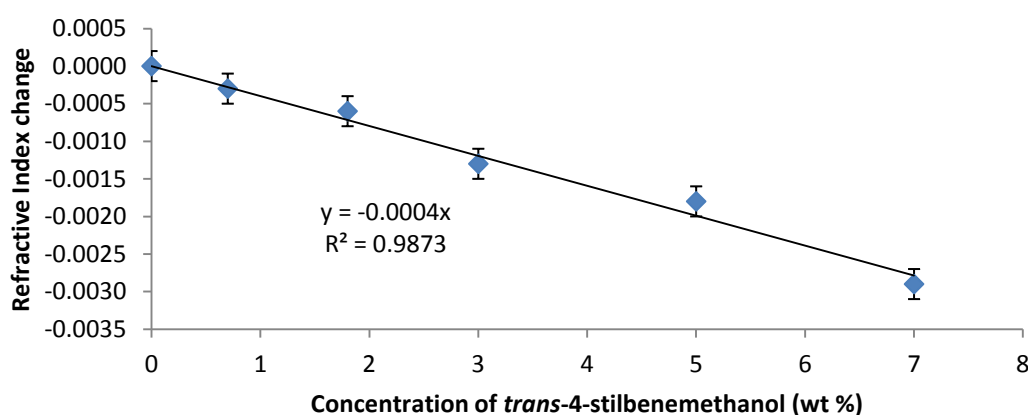
Figure 3.2 The RI change of the thin films (~3 μm) induced by UV laser irradiation for different TS concentration.

3.2.2. **Surface grating on thin films**

Surface gratings were observed when the spin-coated films were irradiated by phase masked exposure. Diffraction of the irradiated area behind the phase mask confirmed the formation of Bragg gratings, but whether the grating was surface kind or volume one was uncertain. Therefore, the surface morphology of the grating area on spin-coated films was examined by AFM. Figure 3.3 and Figure 3.4 show the micrographs of gratings formed by three phase masks with different pitches. Surface gratings are observed for all gratings in spite of small difference microscopically. The structure of periodic strip is noticeable for all samples, but there are even somewhat repeated structures along the strip for the surface grating written using 570 nm phase mask. The morphology difference of three surface gratings might be due to different diffraction patterns of the used phase masks because the three used phase masks have different diffraction ratios for each order.

(a)   (b)
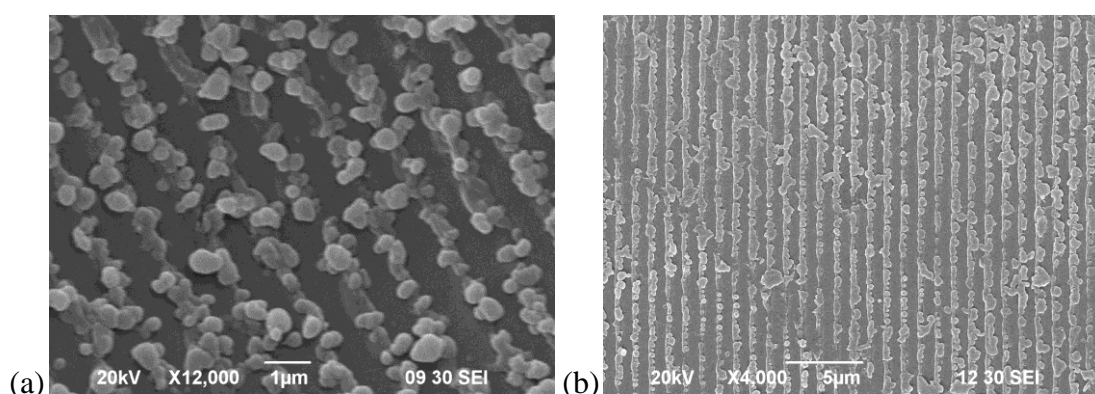
Figure 3.3 AFM photograph of the surface grating written on 7 wt% TS doped thin film using two phase masks with different pitch: (a) 1046.5 nm; and (b) 1070 nm. Irradiation conditions: irradiance 30 mW/cm^2; irradiation time 10s**.**
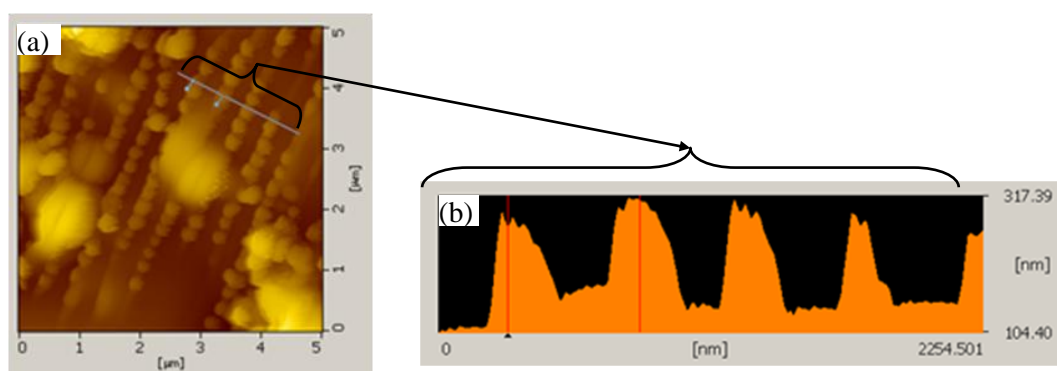
Figure 3.4 Morphology of surface relief grating written on 7 wt% TS doped PMMA film: (a) top view; (b) side view of grating. The height of the surface relief is about 300 nm. The period of the phase mask is 570 nm. Irradiation conditions: irradiance 35 mW/cm^2, irradiation time 10s.

The formation mechanism of these surface gratings on TS doped films should be close to, if not the same, the formation of surface relief gratings (SRG) on azobenzene doped polymer film considering the chemical structure similarity between TS and azobenzene [135]. Both of them conduct trans-cis transition under UV irradiation at certain wavelength. Formation mechanism of SRG on azo dyes doped polymer films is a complicated and hot topic [56], thus, further study of SRG on TS doped films might also be of great scientific importance. However, detailed study of SRG is out of the scope of the present study, and observation of surface gratings on film makes the formation of volume grating in film doubtful for the diffraction might be due to surface gratings.

To verify the formation of volume gratings in thin films, refractive index matching liquid was applied on the grating surface to eliminate surface gratings and to suppress its diffraction. Fortunately, diffraction was still observed, indicating the formation of volume gratings in film in spite of reduced diffraction intensity. To further confirm the formation of volume grating in films, the sandwiched films are

prepared, which is covered by a piece of cover glass to completely prevent formation of SRGs.

3.2.3. **Volume holographic gratings in sandwiched films**

Two kinds of volume grating, namely, Bragg grating and long period grating, are successfully written in the sandwiched films using the phase mask technique and the interferometric technique. Figure 3.5 shows the Bragg diffraction by a volume Bragg grating, or volume holographic grating (VHG), written in the sandwiched film using the interferometric system. Since formation of the surface gratings is completely prevented, diffraction must be due to volume gratings. By changing the intersecting angle of two separated laser beams, the shortest period achieved is about 350 nm. Figure 3.6 exhibits the diffraction of a red laser beam by the amplitude mask and the long period gratings written in a sandwiched film.
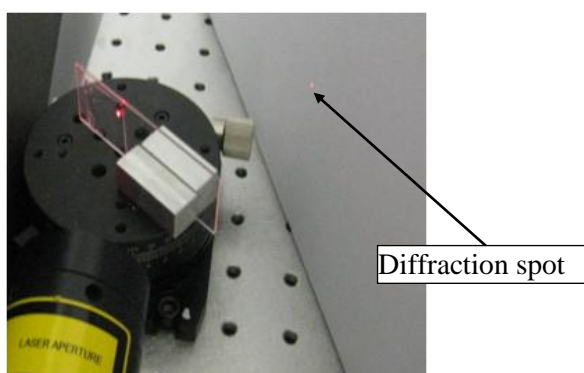
Figure 3.5 Bragg diffraction of grating written in *tran*-4-stilbenemethanol doped PMMA film sandwiched between glass slide and cover glass
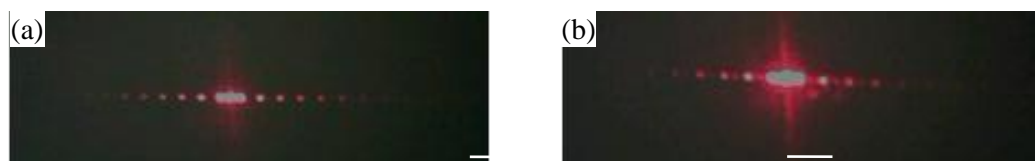
Figure 3.6 Diffraction of (a) 375 μm amplitude mask and (b) film grating written by 375 μm amplitude mask

3.3. **Summary**

In conclusion, this chapter studies the photosensitivity of the TS doped film. It has been confirmed that the RI of TS doped copolymer films on glass slide decreases after irradiation, and the magnitude of reduction linearly increases as raising TS dopant concentration. Moreover, volume holographic gratings are written in the sandwiched films using both the phase mask technique and the interferometric method. Also, long period gratings are written in the sandwiched films using amplitude masks.

CHAPTER 4 PREPARATION   OF   PHOTOSENSITIVE SINGLE-MODE POLYMER OPTICAL FIBERS

This chapter aims to prepare photosensitive single-mode POFs for inscription of Bragg gratings. The most concerned qualities of the POFs are optical properties including the numerical aperture (NA) determined by RIP, the diameter of fiber core, and fiber loss. Ideally, the fabricated fibers have the same NA and core diameter as the most commonly used single-mode silica fiber (e.g. SMF-28e, Dow Corning), so that they are fully compatible with fiber optic instruments that are designed for silica fibers. Therefore, the RIP of the fabricated fibers are closely examined and optimized. Also, the fluctuation of fiber diameter is investigated because it has tremendous impact on the repeatability of the following experiments like grating inscription. In addition, the attenuation of fibers is measured and reduced by various measures.

4.1. **Experiment**

4.1.1. **Fiber preparation**

The two-step preform-drawing method was used to prepare fibers [49]. The preform was formed by Teflon thread method, and heat-drawn to fibers on the drawing tower.

4.1.1.1. Chemicals

In addition to chemicals mentioned in 3.1.1, 2,2,2-trifluoroethyl methacrylate (TFEMA; 98% purity) was also bought from ILUSA.

4.1.1.2. Monomer purification

Monomer purification aims to remove inhibitor and moisture in liquid monomers—MMA, EMA, BzMA and TFEMA. The inhibitor, which is added in monomers to prevent polymerization during transport and store, needs to be removed prior to usage. The first approach to remove inhibitor was to wash monomers with alkaline solution. The experimental procedure is as follows: (1) Sodium hydroxide (10 g) was dissolved into deionized water (190 g) to obtain alkaline solution; (2) To a 250 mL separatory funnel was added 200 mL of monomer liquid and 50 mL of the prepared alkaline solution, the separatory funnel was gently shaken and set aside to allow for the complete separation, and then the water phase (bottom layer) was released through the tap, and this washing process was repeated for two more times; (3) The monomer was washed with 50 mL of deionized water in the same manner as alkaline solution for three times to remove any residual sodium hydroxide.

This alkaline-washing approach was not used later because it was not suitable for BzMA, because the density of BzMA (1.04 g/mL at 25 ℃) is very close to that of water, and the two phases separate extremely slowly during alkaline and water washing. Therefore inhibitor remover columns (Sigma-Aldrich) were applied to remove the inhibitor. The procedure is quite simple, that is, the monomer was added drop-wise into the column and collected at the bottom.

After removing the inhibitor, the second step of purification is to remove moisture in the monomers using desiccant: (1) to the monomer liquid (~200 mL) was added 30 g of Na_2SO_4, and the mixture was set aside for two days to remove the most moisture; (2) the mixture was filtered, and then 10 g of CaH_2 was added to the monomer liquid.

The mixture was filtered again after no bubble (hydrogen produced by the reaction between CaH_2 and H_2O) was observed; (3) the purified monomer was stored in a refrigerator for use.

4.1.1.3. Preparation of cladding preform

The cladding preform was polymerized in a test tube by Teflon thread method. Figure 4.1 shows a prepared cladding preform in a test tube. The fabrication process involves two major steps: (1) fixing a PTFE thread at the bottom of a test tube; (2) polymerizing cladding. The detailed experimental procedures are as follows.

A PTFE thread of 0.8 mm in diameter was guided through the central hole of a PTFE slice and a knot was tied to prevent the threat sliding out. The PTFE slice was then placed at the bottom of a test tube with an inner diameter of about 130 mm. About 2 g of cladding polymerization solution (described in the next paragraph) was added into the test tube, and the test tube was heated at 90 ℃ for one day to fix the Teflon slice. Epoxy adhesive was also tested to stick the PTFE slice to, but it was found that the epoxy adhesive created a lot of bubbles at elevated temperature during polymerization, so the epoxy adhesive was not used. Because the PTFE slice tilted some time and the Teflon wire deviated from center at the bottom of the test tube, a second slice was used to position the wire at center of the test tube, as shown in Figure 4.1.

The second step is to prepare polymerization solution and polymerize the preform in the test tube fixed with the PTFE thread. To the solution of MMA (57.1 g, 0.57 mol) and TFEMA (5.0 g, 0.03 mol) were added lauroyl peroxide (71.8 mg, 0.18 mmol) and 1-butanethiol (161 μL, 1.5 mmol). The solution was filtered using PTFE filter

with 0.2 μm pore size (Cole Parmer) into the test tube. The PTFE thread was stretched straight and stunk to the test tube top with adhesive tapes, and the tube open was covered and sealed uses a finger cot. Then the test tube was heated in an oil bath at 65 ℃ for 2 h, then 60 ℃ for 10 h, 70 ℃ for 36 h, 80 ℃ for 8 h, 90 ℃ for 8 h, 100 ℃ for 8 h, 110 ℃ for 12, and finally 115 ℃ for 12 h. After polymerization (Figure 4.1), the test tube was scratched using a glass knife and shattered to break, and the cladding preform was obtained.
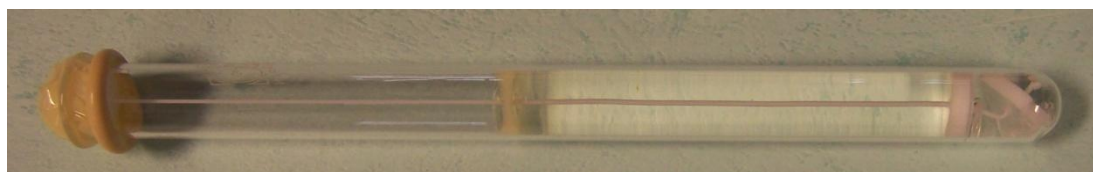
Figure 4.1 Photo of a fabricated cladding preform still in the test tube. The test tube was sealed by a finger cot to prevent vaporization of monomers during polymerization.

4.1.1.4. Polymerization of fiber core

The core of polymer fiber was polymerized from monomers in the central hole of cladding. Initially, the solution was not prepolymerized and the procedure is as follows. The bottom end of the central hole of the cladding preform was sealed using epoxy adhesive. The core polymerization solution was prepared by mixing the following reagents: monomers (0.1 mol; pure methyl methacrylate or with other monomer as specified), lauroyl peroxide (12.0 mg, 0.03 mmol), 1-butanethiol (26.8 μL, 0.25 mmol), and TS (70.0 mg, 0.33 mmol). The mixture was placed in an ultrasonic cleaner for five minute to fully dissolve TS. Then the solution was filtered through the PTFE filter and injected into the cladding hole via a syringe with long needle. The cladding preform was inserted into a slightly larger test tube, and the test tube was then heated in an oil bath at 50 ℃ for 24h, then 65 ℃ for 24 h, 80 ℃ for 8 h, 90 ℃ for 8 h, 100 ℃ for 8 h, 110 ℃ for 12 h, and 120 ℃ for 12 h. Finally, the

fiber preform was formed and ready for fiber drawing. The resultant fibers, drawn from the preform fabricated like this process, exhibits graded RIP, and also a much larger core diameter than the desired due to the swelling and diffusion of core monomers into the cladding preform during core polymerization. Though this swelling and diffusion process can be exploited to fabricate graded-index POFs, it is not favorable in present study. Hence, the core solution was prepolymerized before injected into the cladding hole.

However, the procedure in the above paragraph was not suitable anymore because the prepolymerized solution became very sticky and it was almost impossible to use syringe to inject it into the cladding preform. Hence the experimental procedure was modified. The prepolymerized solution, as prepared in the above paragraph, was heated in a test tube (inner diameter slightly larger than the cladding preform) at 90 ℃ for 2 h. Then the cladding preform was inserted into the test tube and gently pressed so that the prepolymerized solution was pressed into the preform. The bottom end of the cladding preform was wrapped with PTFE sealing tape to prevent the solution flow upward into the gap between the out surface of the cladding preform and the test tube. The test tube was heated at 90 ℃ for another 6 h, and then 100 ℃ for 8 h, 110 ℃ for 12 h, 120 ℃ for 12 h. After polymerization, the test tube was shattered to obtain the preform.

4.1.1.5. *Fiber drawing*

The preform was drawn to fiber by use of a drawing tower as shown in Figure 4.2. Prior to drawing preform to fiber, the preform was heated at 70 ℃ under vacuum for four days because this process was found effectively reducing the fiber attenuation,

especially for the visible light range. Then the preform was fed into the heating jacket continuously by a motor, and the tip was heated to melt, and the melted preform tip was drawn to fiber around a PVC roller (outer diameter 35 cm) driven by another motor. Three parameters were under control during the drawing process, namely, the drawing temperature, the preform feeding speed and the fiber drawing speed. The drawing temperature here is actually the temperature of the heating jacket since the temperature sensor was mounted in the jacket. As a result, the drawing temperature was much higher than the melting point of the fiber (about 160 ℃ for PMMA). The drawing temperature was chosen so that the drawing process could be continuous. Continuous drawing is essential since stable drawing condition could only be reached after a certain time of drawing. Too low temperature resulted in large drawing tension and fibers easily broke, whereas too high temperature produced melted preform not viscous enough to draw, and also high temperature degraded polymers. The drawing speed and the preform feeding speed are correlated via the desired fiber diameter and the preform diameter on the basis of conservation of mass and unchanged density:

$$\frac{D_f}{D_p} = \left(\frac{v_p}{v_f}\right)^2 \tag{4-1}$$

Where D_f is the fiber diameter; D_p is the preform diameter; v_p is the preform feeding speed; v_f is the fiber drawing speed. Experimentally, the preform feeding and fiber drawing speed were set as low as possible because high speed might lead to fiber vibration. Additionally, the drawing temperature and speed were correlated. A specific drawing temperature matched a drawing speed so that heat transfer between the heating jacket and preform reached the equilibrium state, that is, no heat

accumulated on preform and the temperature of the preform kept constant. Even theoretically, it might not be possible to calculate the optimal drawing conditions, because the drawing process involves the simulation of heat transfer from oven to preform (including radiation and convection heat transfer), air flow due to temperature gradient, and extensional flow of the polymer. By trial and error, the typical parameters for drawing single-mode fibers (about 130 μm in diameter) were as follows: the drawing temperature 350 ℃, the preform feeding speed 0.3 mm/min, the drawing speed 3000 mm/min.

In order to reduce the fluctuation of fiber diameter, a PTFE cap was mounted on the heating jacket, as shown in Figure 4.2. After using this cap, the drawing temperature was decreased to 220 ℃, while the preform feeding speed and the fiber drawing speed was not changed.
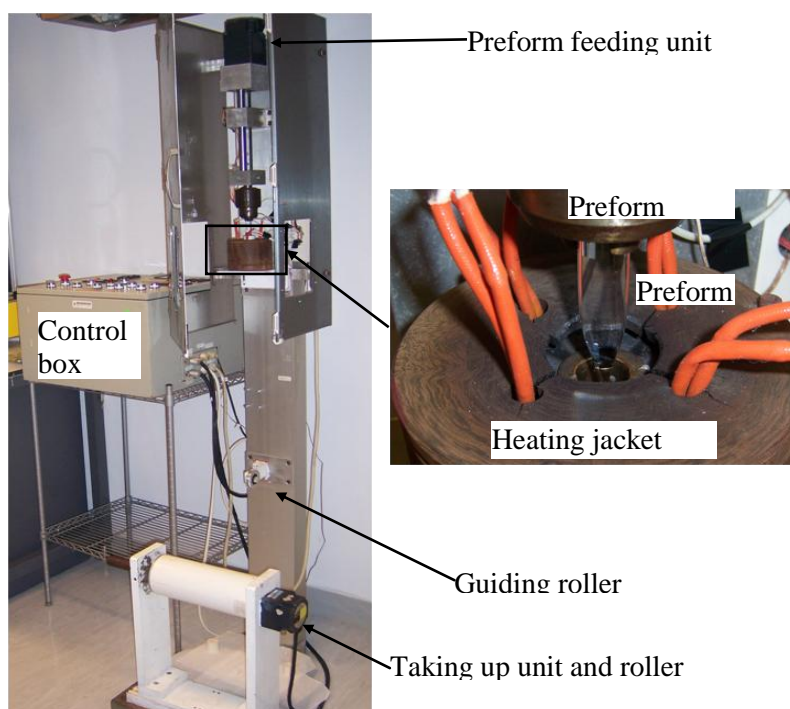
Figure 4.2 Fiber drawing tower

4.1.2. **Fiber annealing**

The temperature profile of one annealing cycle, as shown in Figure 4.3, is the same as that used in [93]. The as-drawn fiber was heated to 80 ℃ within 0.5 h in a climate chamber (C7-600, Votsch). The temperature was kept for 2 h at 80 ℃ before slowly decreased to room temperature within 8 h.
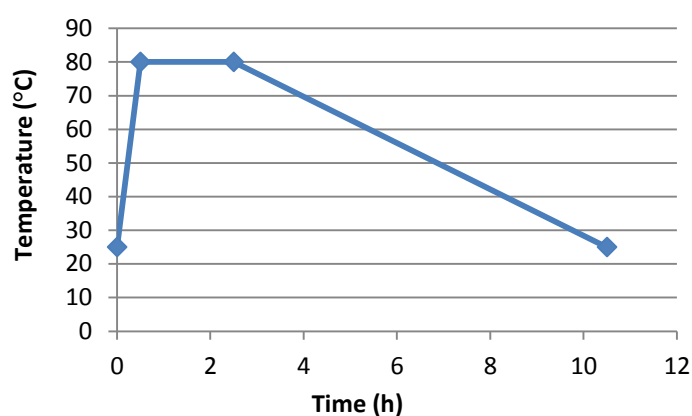
Figure 4.3 Temperature profile of one annealing cycle

4.1.3. **Refractive index profile measurement**

The RIP of fabricated fibers was measured on S14 Refractive Index Profiler (Photon Kinetics, Inc). The principle of the measuring system is based on the refracted near-field technique [136, 137]. The measurement wavelength is 632.8 nm. A fiber with a relative larger diameter (~250 μm) rather than single-mode fibers was used in measurement for easy handling.

4.1.4. **Fiber attenuation measurement**

The attenuation of the fabricated single-mode POFs was measured using the cut-back method and the experiment setup is shown in Figure 4.4. The attenuation at various wavelengths was measured using three broad band light sources, which were

centered at 670 nm, 975 nm, and 1310/1550 nm, respectively. The fiber was cut back at least three times so that three points were obtained and fitted to calculate the attenuation. The transmitted light was measured using an optical spectrum analyzer (ANDO 6317). It is assumed that there was no coupling loss between the POF and the multi-mode fiber (MMF) due to the core diameter of MMF (60) μm being much larger than that of POF (about 10 μm).

Figure 4.4 Diagram of the experimental setup to measure attenuation of single-mode POFs. Light was coupled into POFs via single-mode fiber (SMF) from light source, and collected by multi-mode fiber (MMF) and transmitted to OSA to record spectrum. Coupling between SMF and POF was fixed using UV adhesive, while the other end of POF was cut and connected to MMF.

4.2. Results and Discussion

4.2.1. Single mode condition analysis

The core diameter and numerical aperture (NA) of the fabricated POFs are desired to be the same as that of SMF-28e, as mentioned at the start of this chapter, the most widely used single-mode step-index silica fiber. This is because there is no commercial connector based on single-mode POFs, and light has to be coupled into single-mode POFs via single-mode silica fibers. To maximize the coupling efficiency, the ideal parameters of the fabricated POFs should be the same as that of SMF-28e, typical specifications of which are listed in Table 4.1.

Table 4.1 Typical specifications of SMF-28e provided by manufacturer

Core diameter	8.2 μm
NA	0.13
Cladding diameter	125 μm
Refractive index of core	1.47
Refractive index difference between cladding and core	0.36%
Cut-off wavelength	1260 nm

As for PMMA based POFs, the RI difference between the core and cladding to satisfy single-mode condition should be recalculated because it is different from that of SMF-28e due to different absolute values of RI for silica and PMMA. The single-mode criteria is set by the V number for step-index fibers

$$V = \frac{2\pi a}{\lambda} NA = \frac{2\pi a}{\lambda} \sqrt{n_1^2 - n_2^2} \leq 2.405 \qquad (4\text{-}2)$$

Where a is the core radius, n_1 is the RI of core, and n_2 is the refractive index of cladding. To be the single mode, V should be equal to or less than 2.405. For PMMA based fibers, n_1 is about 1.49, so n_2 needs to be 1.485 to obtain 2.405 for V at 1300 nm (a=4.1 μm), that is, the RI difference between cladding and core should be equal to or less than 5×10^{-3} to satisfy the single-mode condition for PMMA based fibers with 8.2 μm core.

4.2.2. **Refractive index profile optimization**

Figure 4.5 shows the RIP of a fiber fabricated without prepolymerization of core monomers, which has a core of TS doped poly(MMA/BzMA 90/10 mol%) and a cladding of pure PMMA. BzMA was copolymerized in the fiber core to increase its RI. The index profile is graded-index rather than step-index, and the largest index difference is 6.3×10^{-3}, which is close to the value of 5×10^{-3} required for single mode operation. The measured fiber has a large core/cladding diameter ratio, namely,

28/193 (=19/130). This value means that even if the fiber is drawn to 130 μm, the core diameter is still as large as 19 μm. Alternatively, the cladding diameter will be only 55 μm to make the fiber core 8 μm, but such fibers are too thin to handle. The reason for the graded index profile and large core diameter originates from the swelling and diffusion of core monomers into the cladding preform. Though this swelling and diffusion process has been exploited to fabricate graded-index POFs, it is not favorable for the present study.
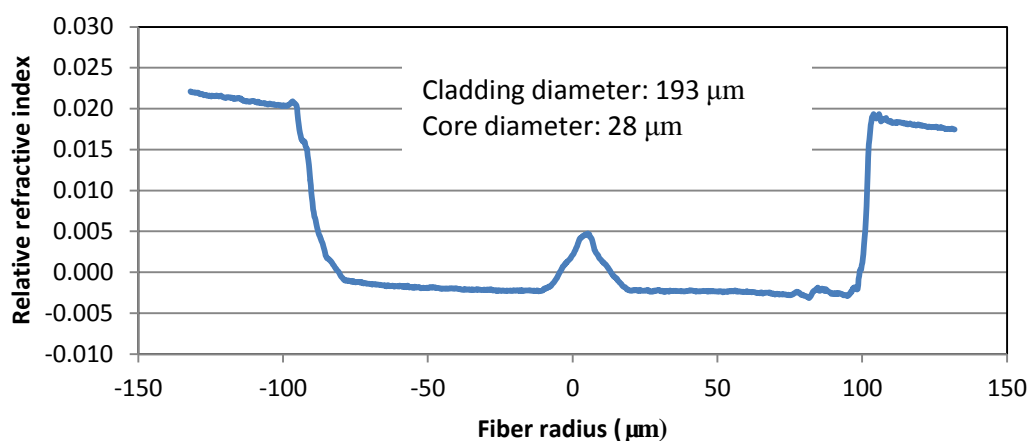
Figure 4.5 RIP of the fiber with poly(MMA/BzMA, 90/10 mol%, 0.7 wt% TS) core and PMMA cladding. The largest index difference is close to that of single mode silica fiber, but the profile is graded and core/cladding diameter ratio is almost two times as that of standard single mode step-index silica fiber.

In order to prevent swelling and diffusion process during core polymerization, the polymerization solution for core was prepolymerized and then injected into the cladding preform. After prepolymerization, most molecules in the polymerization solution were oligomers and the solution became viscous, so swelling and diffusion became difficult during the fabrication process. Figure 4.6 shows the index profile of a fiber with core prepolymerized. The fiber became step-index, and the core/cladding diameter ratio decreased to 10/130, suggesting prepolymerization of core can effectively prevent swelling and diffusion of monomers into the cladding preform.

Nevertheless, the core/cladding diameter ratio is still larger than that of the PTFE thread to test tube (8/130), which means that the prepolymerization technique does not completely prevent the swelling and diffusion process. The largest index difference increased to 12×10^{-3} due to the reduced fiber diameter, and it needs to be decreased to satisfy single-mode condition.
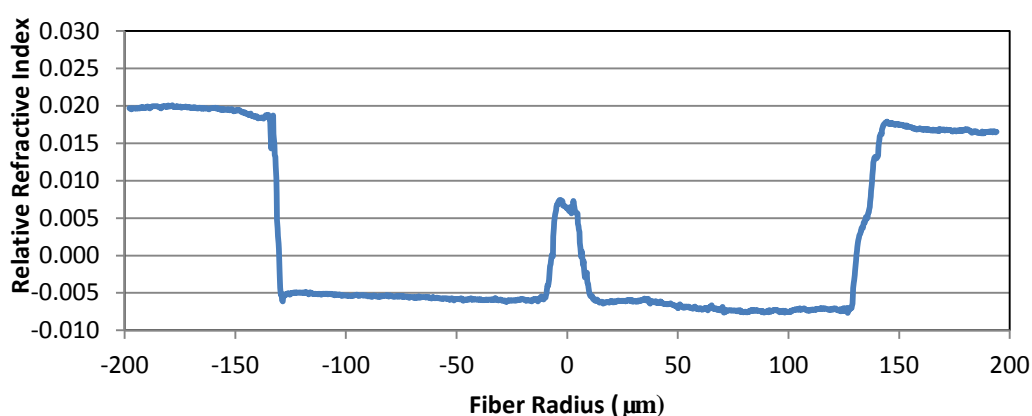
Figure 4.6 RIP of fiber with poly(MMA/BzMA 90/10 mol%, 0.7 wt% TS) core and PMMA cladding. The core was prepolymerized before it was injected into cladding hole.

Grating inscription on fibers with index profile of Figure 4.6 shows that BzMA exhibits certain photosensitivity under high power and long time irradiation of 325 nm laser, even the fiber is not doped with TS. Because photosensitivity induced by BzMA component might lead to the degradation of the fiber core, and thus wave guiding property, BzMA was not copolymerized to MMA to form fiber core. Rather than add other monomers into fiber core to increase the index of core, TFEMA was copolymerized with MMA in cladding since TFEMA has lower RI than MMA, whereas fiber core is PMMA doped with TS. The RIP of this kind of fiber is shown in Figure 4.7. The largest index difference between core and cladding is about 6×10^{-3}, and the profile is much more close to step-index. The diameter ratio of core/cladding is calculated to be 8.7/130 (16/239). Figure 4.8 shows the end of such a fiber drawn

to about 133 μm when the other end was directly coupled to a single-mode light source emitting red light. The diameter of guided light is measured as 11.6 mm, still larger than 8 μm for single-mode condition.
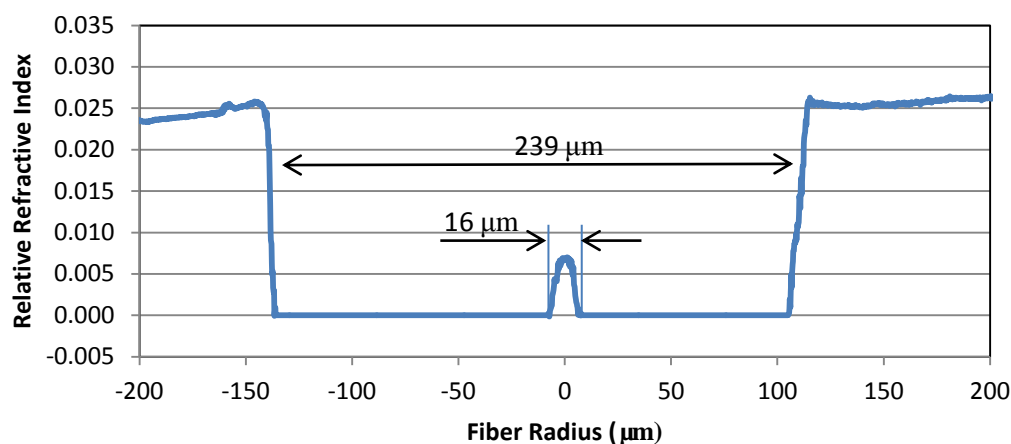
Figure 4.7 RIP of the fiber with poly(MMA, 0.7 wt% TS) core and poly(MMA/TFEMA 95/5 mol%) cladding. The core was prepolymerized before it was injected into cladding hole.
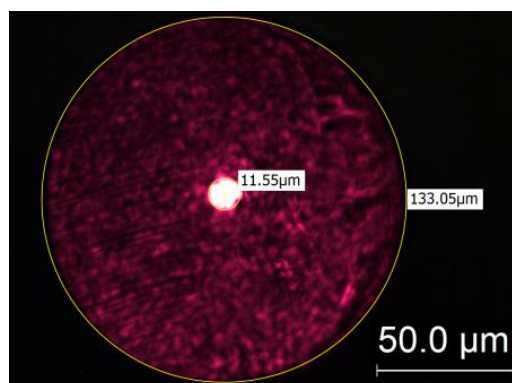
Figure 4.8 Photo of a typical fiber end cut by a hot knife when the other end connected to single-mode light source.

4.2.3. **Impact of annealing on refractive index profile**

The as-drawn fibers were annealed to release residual stress formed during fiber drawing, and thus to improve the thermal stability of the fibers and Bragg grating in them. Residual stress in the fibers arises mostly from the thermal stress induced by a difference in thermal expansion coefficients between core and cladding and

mechanical stress produced by a difference in the viscoelastic properties of the two regions [138]. It not only has impact on thermal [139] and mechanical behavior [140, 141], but also can affect the optical properties of the fibers, and change RI through the stress-optic effect [35, 142].

Annealing treatment is an effective method to remove residual stress by heating the polymer at elevated temperature and then cooling gradually. Since residual stress correlates with RI through stress-optic effect, annealing may have effect on the RIP of the fibers. Figure 4.9 shows RIP of the as-drawn fiber and after the annealing treatment. The index profile essentially maintains the main shape even after 20 times annealing.
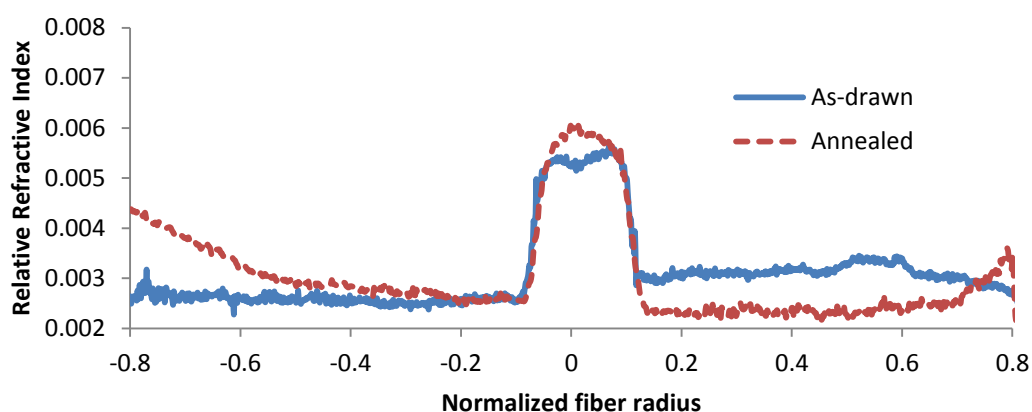
Figure 4.9 RIPs of an as-drawn fiber and after annealed 20 times.

4.2.4. **Fiber diameter fluctuation and control**

The as-drawn fibers had large diameter fluctuation initially. Figure 4.10 shows the diameter distribution along a 250 μm fiber for the whole drawing process, and Figure 4.11 demonstrates the diameter fluctuation measured in the short range using a micrometer. At the beginning of the drawing process, fiber diameter decreases and fluctuates at the same time due to the deformation of the preform. After about 40 min,

the diameter still varies dramatically around 250 μm, and the standard deviation of the diameter is calculated to be as large as 18 μm, which is 7% of the average diameter. Fourier analysis of the data in Figure 4.10 and Figure 4.11 reveals that the diameter fluctuates randomly.

This large diameter fluctuation might be tolerable for 250 μm drawing, for at least fibers can be drawn continuously. But for thin fiber (130 μm), this large diameter fluctuation is catastrophic, and fibers easily broke during drawing. Figure 4.12 presents an attempt, one of many others, to draw 130 μm fibers. The fiber broke and could not be drawn continuously even at when the drawing temperature was raised to 400 ℃. The probable cause for this random fluctuation lies in the unsteady air flow through the heating ferrule during drawing [81, 82]. Since the heated air flowed upwardly without block, turbulent air flow could lead to unsteady heat transfer from the oven to preform, and consequently random diameter fluctuation.
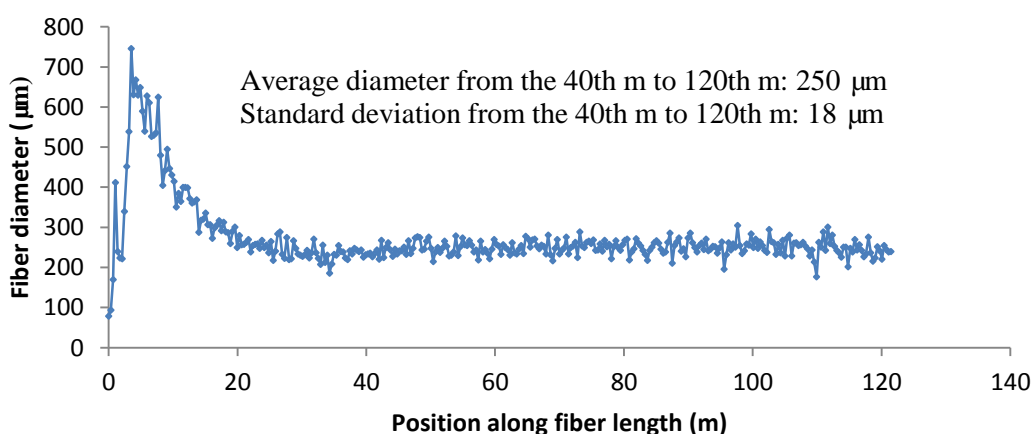
Figure 4.10 Diameter of the as-drawn fiber measured per 35 cm along the fiber for the whole drawing process. Drawing conditions are as follows: Preform feeding speed 0.6 mm/min, fiber drawing speed 1575 mm/min, preform diameter 13.5 mm.
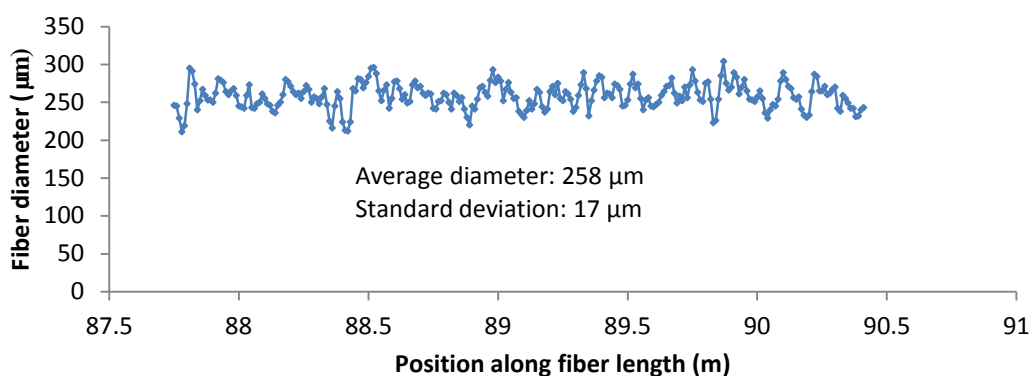
Figure 4.11 Diameter of the drawn fiber measured per centimeter along fiber for 2.5 m after the drawing process reached steady condition
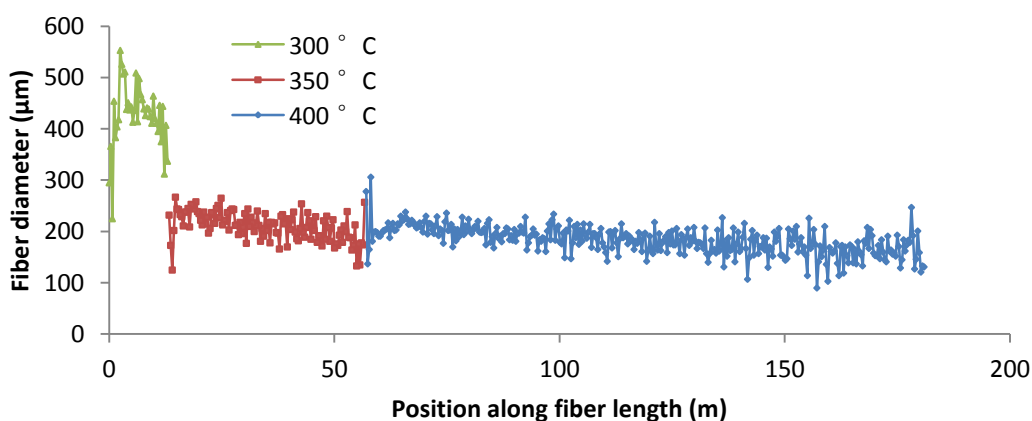
Figure 4.12 Diameter distribution of the fiber drawn from a single preform at three drawing temperatures. The drawing temperature was 300 ℃ at first, and the fiber broke after drawing for a while; then the temperature was increased to 350 ℃, and the fiber still broke; at 400 ℃, the fiber broke again before the diameter stabilized.

The first tested approach to prevent the turbulent air flow within the heating jacket was to fix a plastic tube with an adjustable diaphragm under the heating jacket (Figure 4.13). It was hoped that the air flow into the jacket can be blocked as the aperture of diaphragm was reduced during the drawing process. But it was found that fibers started to vibrate violently when reducing the aperture. The smaller the aperture was, the stronger the vibration became. Strong vibration of fibers leads to uneven diameter, and make the fiber even more vulnerable to break. Hence this approach was not feasible.
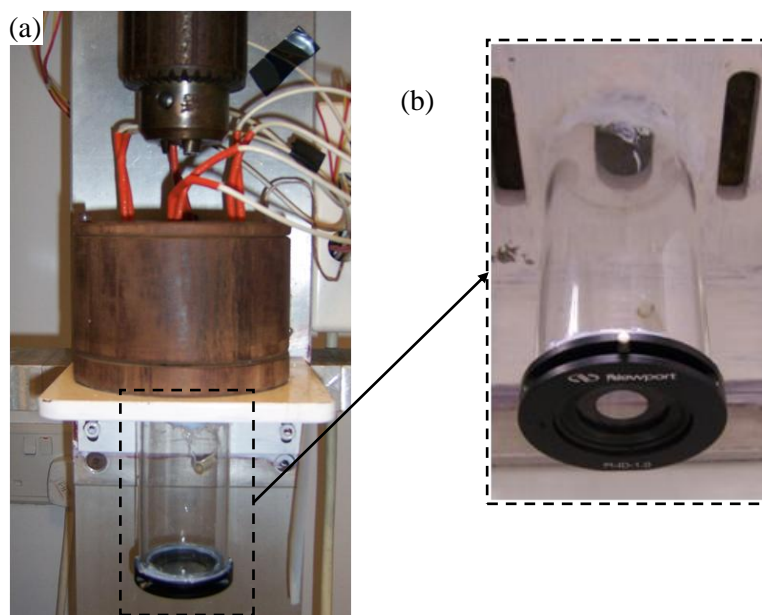
Figure 4.13 A plastic tube with an adjustable diaphragm was adhered under the heating jacket to prevent air to flow into the jacket.

The second method was to place a PTFE cap on the top of the heating jacket, as shown Figure 4.14. The preform was fed into the heating jacket through the central hole of the PTFE cap. To avoid direct contact between the preform and the cap, the hole of the cap is slightly larger than the preform. After adding the cap, the preform could be continuously drawn to 130 μm fibers, and also the drawing temperature was reduced to around 220 ℃, which was more than 100 ℃ lower than that without using the cap. Figure 4.15 shows the diameter distribution of a 120 μm fiber for 100 cm, with a standard deviation of 3.4 μm. To compare with the case without using the cap, a fiber in diameter of 250 μm was drawn, and its diameter was measured and shown in Figure 4.16. The standard deviation is 10 μm, which is almost half of the value without using the cap (18 μm), though still quite large.
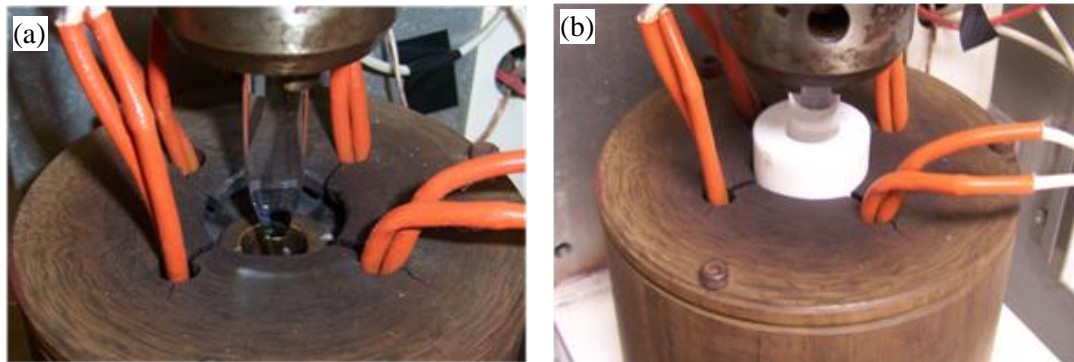
Figure 4.14 Heating jacket (a) with and (b) without the PTFE cap
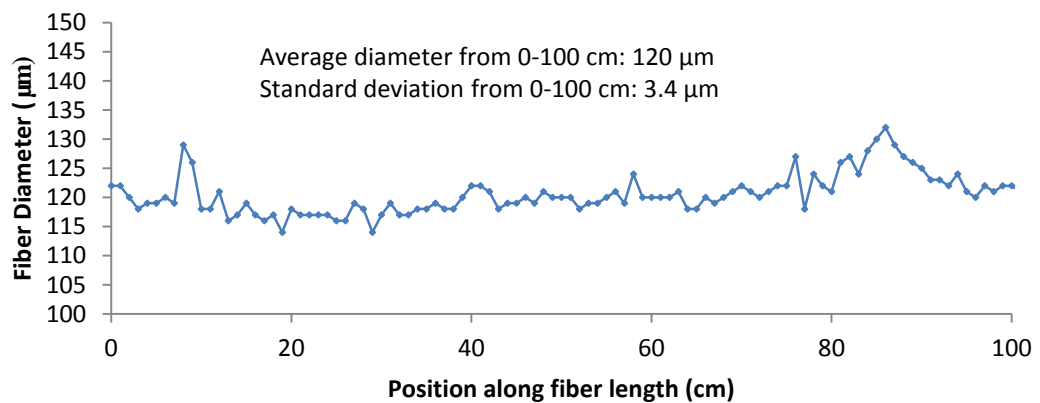
Figure 4.15 Diameter distribution of a fiber for 100 cm measured per 1 cm when the PTFE cap is used (Drawing temperature 250 ℃, feeding speed 0.30 mm/min, drawing speed 3000 mm/min, and preform diameter 13.5 mm)
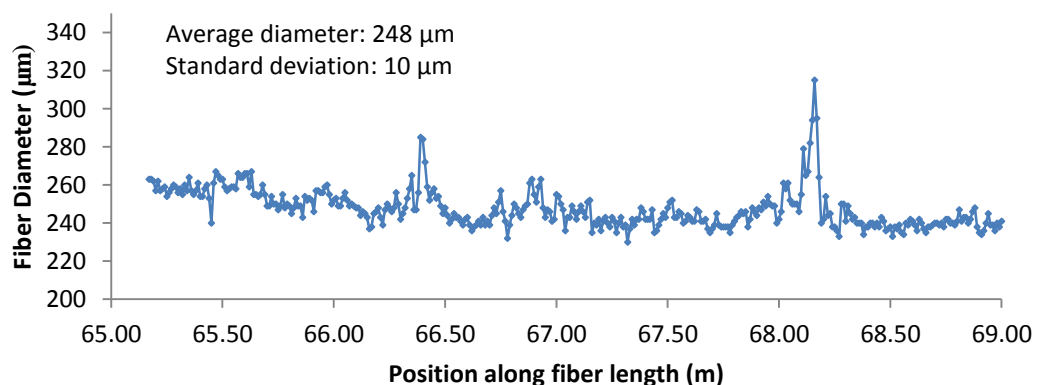
Figure 4.16 Diameter distribution of POF when the PTFE cap is used. Drawing temperature 210 ℃, feeding speed 0.40 mm/min, drawing speed 1109 mm/min, preform diameter 13.4 mm. Peaks in the diameter distribution are caused by manually moving the roller, around which fibers was wrapped.

4.2.5. **Attenuation of POFs**

The POF for attenuation measurement in this section has a core of poly(MMA, 0.7 wt%) and a cladding of poly(MMA/TFEMA 95/5 mol%). The fiber diameter is around 130 μm and the core diameter is approximately 12 μm (Figure 4.8). The RIP is shown in Figure 4.7.

Figure 4.17 shows the attenuation of the fabricated POFs at various wavelength ranges using three light sources, and the attenuation at 650, 1310 and 1550 nm are 19, 49, 121 dB/m, respectively (Figure 4.18). The loss at 650 nm is two times larger than the value of 10 dB/m reported in [95], where the fibers were also drawn from preform fabricated by Teflon-wire method. It is more than two orders of magnitude higher than the absorption loss of PMMA at 650 nm, which is only about 0.1 dB/m [94]. With regards to 1310 and 1550 nm, the measured loss is on the same order of absorption loss (~100 dB/m) report in [94].
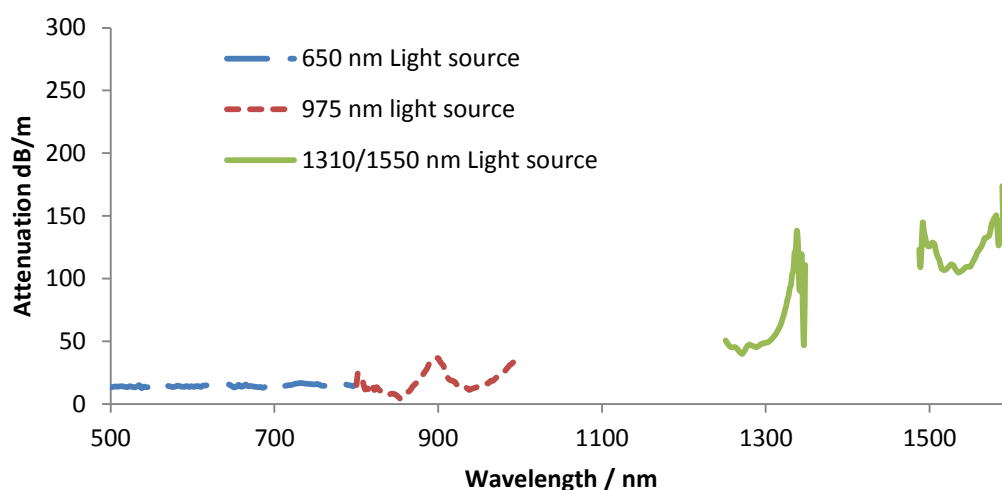
Figure 4.17 Attenuation spectrum of the POFs with poly(MMA, 0.7 wt% TS) core and poly(MMA/TFEMA 95/5 mol%) cladding.
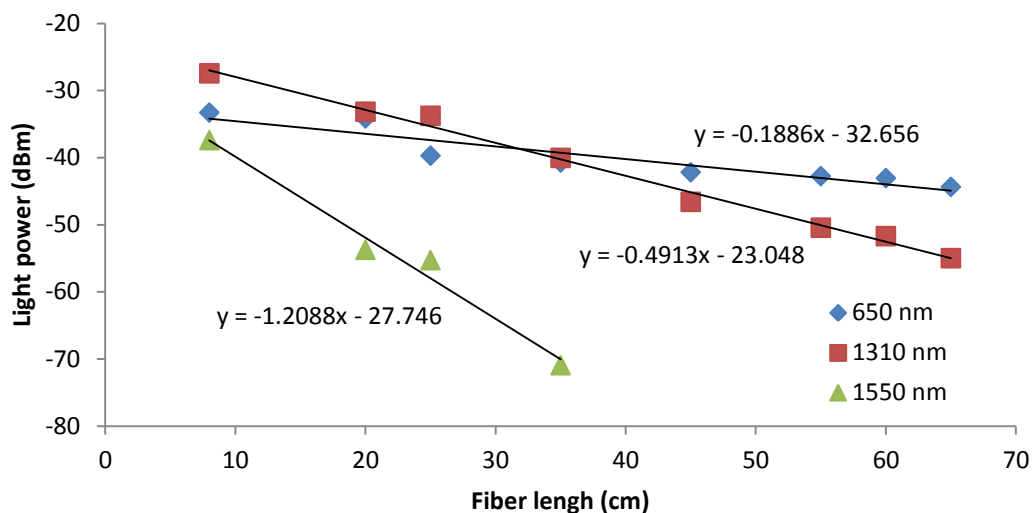
Figure 4.18 Attenuation of the fibers at 650, 1310 and 1550 nm. The loss at 650, 1310 and 1550 nm is 19, 49 and 121 dB/m, respectively.
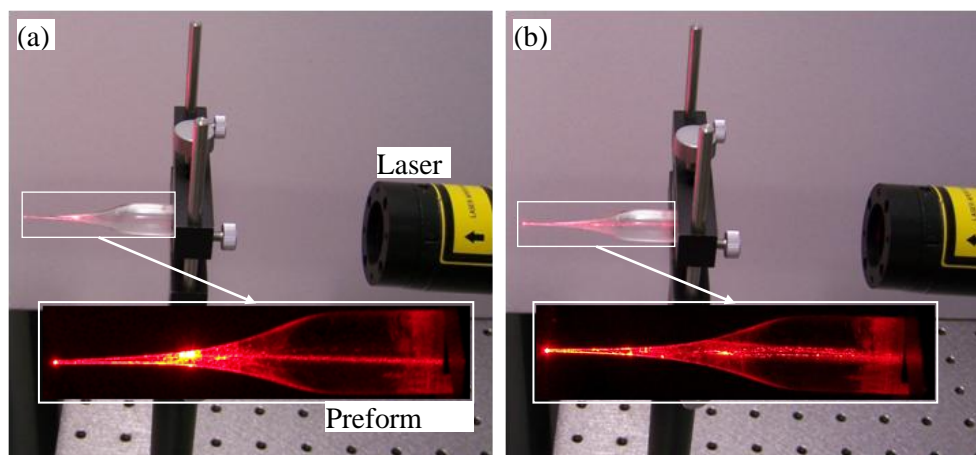
Figure 4.19 Scattering of red laser by (a) cladding and (b) core of a fiber preform. The insets show the photos that were taken when the room light is off.

The most probable reason for this high loss, especially for 650 nm, is caused by scattering because the absorption loss is not at this high level. This hypothesis was tested by an experimental setup illustrated in Figure 4.19. A red laser beam is launched into a short segment of perform after drawing fiber, and the scattering light was recorded using a digital camera. When laser beam was launched into cladding, the scattered light of laser beam observed from side was homogeneous. But when the beam was launched into the fiber core, macro scattering centers were noticed, and

most seemed at the interface between the cladding and core, suggesting inhomogeneous phase at the interface between the fiber core and cladding. This inhomogeneous region might be caused by the fact that cladding and core have slight different polymer and are not fully miscible.

Table 4.2 Attenuation of the fibers in various conditions at four wavelengths. The normal process means no heat treatment on preforms or fibers, and drawing conditions are as follows: drawing temperature 220 ℃, preform feeding speed 0.3 mm/min, fiber drawing speed 3 m/min.

Fabrication Procedures	Attenuation at 650 nm (dB/m)	Attenuation at 960 nm (dB/m)	Attenuation at 1310 nm (dB/m)	Attenuation at 1550 nm (dB/m)
Normal process	19	16	49	121
The drawing temperature was raised to 230 ℃	14	16	33	82
The preform heated at 70 ℃ under reduced pressure for 4 days prior to drawing	1.7	3.3	31	49
The preform heated at 70 ℃ under reduced pressure for 4 days prior to drawing, and the fiber was annealed once	1.2	8.2	53	56
The preform heated at 70 ℃ under reduced pressure for 4 days prior to drawing, and the fiber was annealed six times	4.3	11	34	82
The preform heated at 110 ℃ under reduced pressure for 5 days	0.6	11	28	82
The preform heated at 110 ℃ under reduced pressure for 9 days	0.7	8.3	31	88

Various treatments on preforms or fibers, such as raising the drawing temperature, heating the preform prior to drawing under vacuum and annealing fibers, were tested to reduce the attenuation of fibers, and the result are shown in Table 4.2. Raising the drawing temperature resulted very minor reduce in attenuation, and also, this method was not suitable experimentally because the viscosity of the melt preform at high temperature was too low to draw. Heating the preform prior to fiber drawing was found an effective way to reduce the fiber loss, especially for the loss at visible range.

The preform was heated under vacuum to remove any residual small molecules. Two temperatures were tested, one below and one above T_g of the preform, namely, 70 and 110 ℃. Heat-treatment on preform at 70 ℃ in vacuum for four days decreases the attenuation at 650 nm almost one order, and treatment at 110 ℃ decreases the attenuation for 650 nm 20 times lower than that without any treatment of preforms or fibers. However, the loss reduction at 1310 nm and 1550 nm is quite small, suggesting that the high loss at 1310 nm and 1550 nm range might be absorption-dominant.

4.3. **Summary**

Photosensitive single-mode POFs have been fabricated by the preform-drawing method. The RIP of the fabricated fibers was closely examined and controlled, and the step-index profile was achieved by prepolymerizing the core monomers. The diameter fluctuation of the fabricated fibers has been significantly reduced by a minor modification to the drawing tower—adding a PTFE cap on the heating jacket. The attenuation of the as-fabricated POFs was found very high. Various measures were tested to reduce attenuation, and it has been found that heating the preform prior to drawing fiber can significantly reduce the loss at 650 nm, more than one order in magnitude. The attenuation of the fabricated POFs at 1300 nm and 1550 nm range is still very high. The minimum loss values obtained for 1310 nm and 1550 nm are 31 and 49 dB/m, respectively.

CHAPTER 5 POLYMER FIBER BRAGG GRATING

This chapter deals with the PFBGs, including their fabrication and characterization. The main objective is to study the formation process of Bragg gratings in POFs doped with *trans*-4-stilbenemethanol. The grating formation process has been thoroughly investigated to find the most influential factors that affect the inscription process, and also to understand the grating formation mechanism. In addition, the fabricated gratings are characterized by studying their thermal and strain response.

5.1. Experiment

5.1.1. Grating inscription

5.1.1.1. Inscription system

The phase mask technique was used to fabricate PFBGs, and the writing system is shown in Figure 5.1. A continuous He-Cd laser (Kimmon IK3802R-G) was used for grating inscription, which emits a multimode laser beam at 325 nm with a width of 0.35 nm. The laser beam was focused along the fiber length by a plano-convex lens (focal length 250 mm), while ND filters (Thorlabs FW2AND) were inserted to attenuate the laser and control irradiation irradiance. The beam was then reflected by a mirror and irradiated on fiber through the phase mask. The reflecting mirror was fixed on a motorized linear stage so that the laser beam could be scanned along the length of the fiber to obtain gratings longer than the beam width. In most experiments, the reflection spectrum of the formed grating was monitored during the inscription process by using a broadband light source because of the low reflectivity of the fabricated PFBGs. An optical spectrum analyzer (OSA, ANDO 6315A) and a

1×2 coupler (Newport F-CPL-B12355) were used to record reflection spectrum. Light from the light source was launched into the polymer fiber from a butt-coupled SMF-28e fiber, because of large diameter variation, the fabricated single-mode polymer fiber could not be directly connected to the light source or other fiber optic instruments. The coupling between the POFs and SMF-28e was fixed by a UV adhesive (NOA65, Norland)
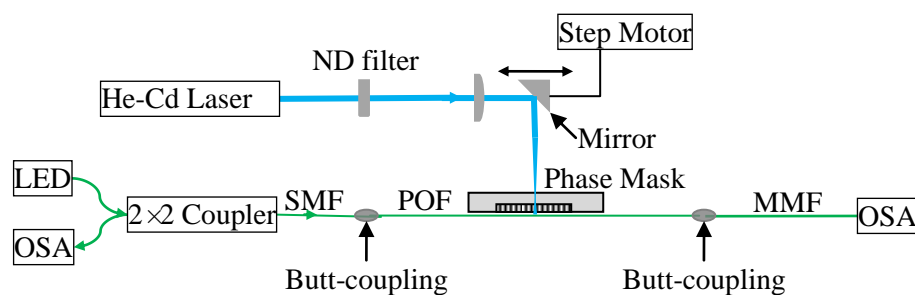
Figure 5.1 Diagram of the PFBG writing system. The whole system is built on an optical table (RS 3000^{TM}, Newport) to ensure mechanical stability.

The alignment of the phase mask and the polymer fiber is illustrated in Figure 5.2. The fiber was fixed on a V-groove of 125 μm, and the phase mask was placed on two layers of polyimide tape. The diameter of the used fiber was ~130 μm, and so there was a gap between the phase mask and the fiber. The phase mask was aligned in this way to avoid direct contact with fiber and hence to prevent the phase mask from contamination.
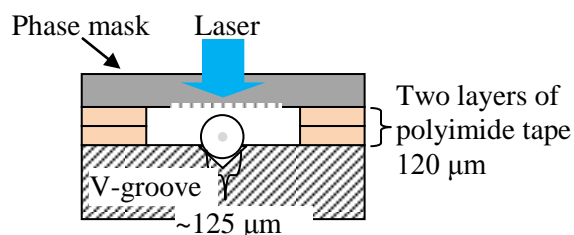
Figure 5.2 Schematic diagram of the alignment of the fiber and the phase mask

5.1.1.2. POFs for grating inscription

Two major kinds of POFs were used for grating inscription: (1) the POF that had poly(MMA/EMA/BzMA) core and PMMA cladding; (2) the POF that had PMMA core doped with 0.7 wt % TS and a cladding of poly(MMA/TFEMA 95/5 mol/mol). The later one was used in most experiments. Its RIP is shown in Figure 4.7, and the diameter of fiber core and cladding are about 12 μm and 130 μm, respectively (Figure 4.8).

5.1.1.3. Laser beam and irradiance of writing

The intensity distribution of the laser beam is illustrated in Figure 5.3. It was focused on the fiber along fiber length by a plano-convex lens with a focus length of 25 cm. The distance from the lens to the fiber was about 30 cm, and the resultant beam was in elliptical shape with a major radius of 1.5 mm and a minor radius of 0.3 mm. The average irradiance on the fiber was estimated to be approximately 2×10^4 mW/cm^2.
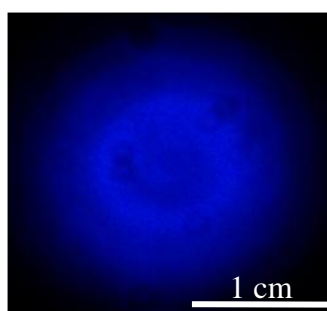
Figure 5.3 Intensity distribution of the He-Cd laser beam. The output laser beam was magnified by a biconcave lens and irradiated on a piece of paper, and the spot on the paper was recorded by a digital camera.

5.1.1.4. Coupling of POF to SMF-28e

To write Bragg gratings in a polymer fiber, the fiber was cut by a hot blade to get a flat end. The fiber was fixed on a V-groove block of a MicroBlock 3-Axis Positioner

(Thorlabs MBT-616), and butt-coupled to a SMF-28e fiber pigtail fixed on another 3-Axis Positioner. The coupling between SMF-28e and the single-mode polymer fiber was checked and adjusted by the observation of clear far field pattern when SMF-28e was connected to a light source emitting red light (Figure 5.4). If the other end of the polymer fiber was also cut and the fibers were connected in the way shown in Figure 5.1, the back reflection of the polymer fiber end can also be detected by the OSA.
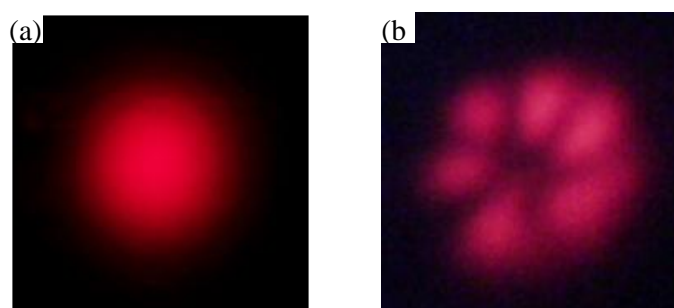
Figure 5.4 Far field patterns of two fabricated polymer fibers: (a) ~130 μm fiber with a 12 μm core, (b) ~180 μm fiber with a 17 μm core. Only the fundamental mode was observed for fiber around 130 μm, where as other modes could be observed for fiber around 180 μm. Observation of these patterns was used to assure good coupling between the polymer fiber and the silica fiber.

5.1.1.5. *Measurement of reflection spectrum and Bragg peaks*

Two OSAs were used to record the reflection or transmission spectrum of FBGs: ANDO AQ6315A and ANDO AQ6331. Due to low reflectivity of the fabricated PFBGs, the reflection spectrum was more easily detected than transmission and hence monitored in most experiments. The model 6315A was used in most experiments for its high wavelength resolution (50 pm) and broad scanning range (350-1750 nm), whereas the model AQ6317 only covers 1200-1700nm. A FBG interrogator (I-MON-512E, Ibsen) was also used to monitor the Bragg peaks (1280-1340 nm), and its wavelength resolution and accuracy are 1 and 5 pm, respectively.

Since the wavelength error for repeated measurement is normally equal to or less than the accuracy of the optical spectrum analyzer or the fiber Bragg grating interrogator, the wavelength reading was recorded once in most experiments. Two light sources were used to monitor PFBGs. Their emitting spectra are shown in Figure 5.5.
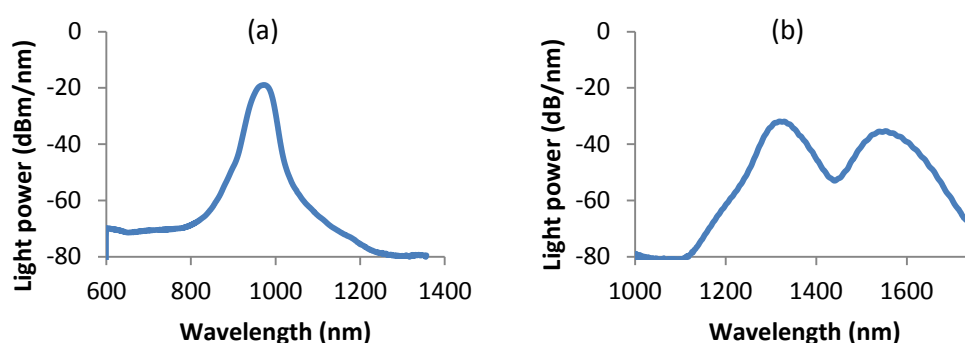
Figure 5.5 Spectra of two used light sources: (a) the light source at 975 nm; (b) the light source emitting 1310 and 1550 nm light

Table 5.1 Period and diffraction ratio of phase masks for 325 nm laser

Phase Mask		Diffraction ratio of 325 nm laser (%)			
NO.	Period (nm)	0th	1st	2nd	3rd
PM573	573	11.4%	44.3%	-	-
PM884	884	0.5%	39.2%	10.6%	-
PM647	647	25.5%	35.6%	1.7%	-
PM1000	1000	9.0%	36.0%	4.8%	4.7%
PM1047I [a]	1046.5	0.6%	40.3%	3.2%	6.3%
PM1047B [b]	1046.5	4.0%	40.5%	2.7%	4.9%
PM1059	1058.6	48.7%	23.6%	0.5%	1.6%
PM1061	1061	10.7%	40.6%	1.4%	2.7%
PM1070	1070	20.8%	35.0%	1.7%	2.9%

[a]: manufactured by Ibsen Photonics
[b]: manufactured by BRAGG Photonics

5.1.1.6. Phase masks

A series of phase masks were used to write Bragg gratings, whose pitch and the measured diffraction ratio for 325 nm are listed in Table 5.1. The diffraction ratio

was experimentally determined by measuring the power of each diffraction order. Two of them were designed for operation at 325 nm, namely, PM884 and PM1047I, and they have zeroth order diffraction <1%. Hence, they were used most to produce Bragg gratings in polymer fiber around 1310 and 1550 nm, respectively. PM647 was also used to write gratings around 960 nm, as the PMMA based fibers have lower attenuation at this wavelength than around 1300 and 1550 nm. Other masks that have high zeroth order diffraction were used in the investigation.

5.1.1.7. *Microstructure observation of PFBGs*

The microstructure of the fabricated Bragg gratings in polymer fibers was observed by using an optical microscope (Nikon Optiphot-Pol Polarizing Microscope) equipped with a digital camera (Leica DFC290 HD). To observe the grating structure in a fiber core, the fiber was immersed in a few drops of index matching oil on a glass slide, and the focus of observation was adjusted to the fiber core.
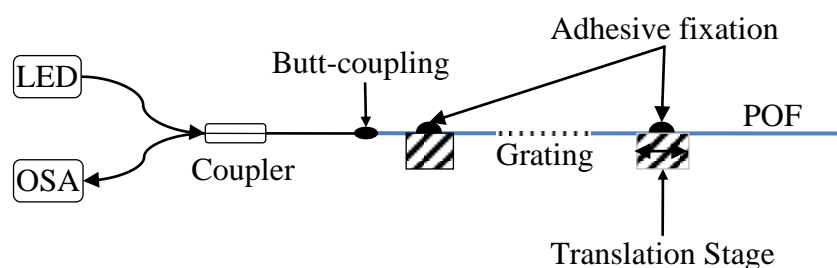
Figure 5.6 Diagram of the experimental setup to measure strain response of PFBGs

5.1.2. **Strain response measurement**

Figure 5.6 shows the experimental setup for measuring strain response of the PFBGs. One end of the polymer fiber with grating was adhered on an XYZ stage, and the other end was fixed on a translation stage. Light from the LED light source was

launched into the polymer fiber butt-coupled to a SMF-28e fiber. Wavelength shift of the Bragg reflection was measured by an OSA during stretching.

5.1.3. **Thermal response measurement**

Initially, thermal response of PFBGs was tested using the experimental setup in Figure 5.7. A thermoelectric Peltier (Melcor, CP1.4-127-045L) was employed to heat the grating in polymer fiber, which was directly placed on the heating device. The surface temperature of the cooler was monitored by a temperature probe (Testo 110 NTC Thermometer, Testo AG).
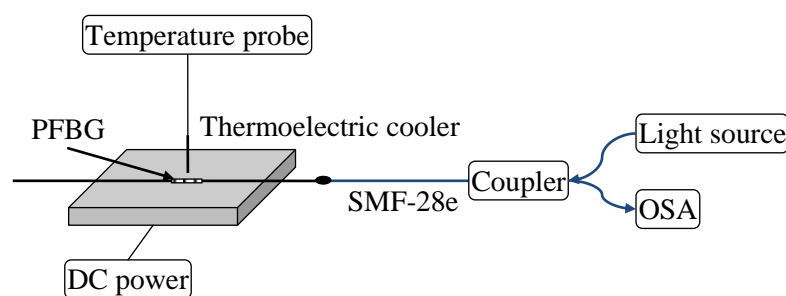
Figure 5.7 Diagram of the experimental setup for measurement of thermal response of PFBGs by the thermoelectric Peltier

5.1.4. **Humidity response measurement**

Humidity response of PFBGs was measured by varying the relative humidity of the environment surrounding PFBGs. The relative humidity was controlled by the climatic chamber (Votsch C7-600), where PFBGs were placed. The climatic chamber can control RH within 10%~98% for temperature from 10 to 90 ℃, with a precision of 1% and 1 ℃ for RH and temperature, respectively.

5.2. **Results and Discussion**

The contents of this section are mainly arranged in the order of the research sequence, as shown in Table 5.2. Subsections 5.2.1 to 5.2.3 are about some factors that influence the PFBG inscription, and hence are to address the problem of how to successfully write PFBGs. Subsections 5.2.4 to 5.2.7 are concerned with the inscription process, including the formation dynamics during long-time UV exposure, and the observed microstructure of PFBGs, and RI modulation of the fiber core by UV exposure. The subsection 5.2.9 reports the relaxation process of PFBGs after inscription and discusses several hypotheses for this process. The last four subsections present responses of PFBGs to temperature, humidity, strain and stress, and salt concentration.

Table 5.2 Structure of the results and discussion section

Contents	Sections
Key factors to inscribe PFBGs	5.2.1 Crucial factors in PFBG inscription 5.2.2 Material for fiber core 5.2.3 Influence of zeroth order diffraction of phase mask on grating inscription
Inscription process (During UV exposure)	5.2.4 Grating formation dynamics 5.2.5 Microstructure of PFBGs 5.2.6 Simulation of the near field of phase masks 5.2.7 Transmission spectrum and estimation of index modulation
Post-inscription (after UV exposure)	5.2.8 Grating relaxation of PFBGs 5.2.9 Annealing induced wavelength shift
PFBG characterization	5.2.10 Thermal response of PFBGs 5.2.11 Humidity response of PFBGs 5.2.12 Strain & Stress response of PFBGs 5.2.13 Response of PFBGs to salt solution

5.2.1. **Crucial factors in PFBG inscription**

By a large amount of trials and errors, two most crucial factors that influence PFBG inscription were identified: (1) quality of POFs; (2) cleaving and coupling of POFs to single-mode silica fiber. The POFs to inscribe Bragg gratings muse be, at least close to, single mode. Large fiber core would lead to dramatic coupling loss between POFs and single-mode silica fibers, making reflection peak observation difficult. As for the fabricated POFs that has core of PMMA doped with 0.7 wt % TS and cladding of poly(MMA/TFEMA 95/5 mol/mol), Bragg gratings could be inscribed in fibers approximately 180 μm in diameter. Bragg peaks could not be monitored for fibers thicker than 180 μm, although Bragg gratings might have been formed.

Another key factor is coupling POFs to single-mode silica fibers. To monitor either the reflection or transmission spectrum of PFBGs, light had to be launched into the core of polymer fibers. Because of large diameter variation, the fabricated POFs could not be directly connected to fiber optic instruments via bare fiber coupler. Therefore, the fabricated fibers had to be butt-coupled to SMF-28e fiber manually. Due to small fiber core (around 10 μm), micropositioner is necessary to achieve fine alignment. Before coupling, polymer fibers had to be cleaved manually to obtain a flat end face (reliable and easy-to-use cleavers for silica fibers are available). A recommended method is to cleave POFs using a hot blade, and this method was used in this study. It would be best to polish the end after cutting, but handling thin POFs to polish is troublesome. This cleaving and coupling issue is a major challenge to the real application of PFBGs.

5.2.2. **Material for fiber core**

Initially, the fiber core was composed of the copolymer of MMA, EMA and BzMA as reported previously [23]. The purpose of adding EMA in fiber core was to improve melting flow property due to its lower T_g (~65 ℃), and BzMA was added to increase RI and enhancing UV absorption because of the phenyl group [49]. However, the reactivity ratios of these three monomers are unknown, and what kind of copolymer is formed is uncertain. In addition, gratings were also written in fibers that had core of poly(MMA/BzMA) without TS (Figure 5.8), suggesting that the RI of the copolymer changed by UV irradiation. The RI change of the copolymer most likely originated from BzMA monomer because BzMA absorbed UV. This kind of grating is not desirable since it would reduce the RI of the core and destroy the wave guiding condition of the fibers. Therefore, in this study, TFEMA (5 mol%) is copolymerized with MMA (95 mol%) as fiber cladding, while the fiber core was composed of pure PMMA doped with 0.7 wt % TS.
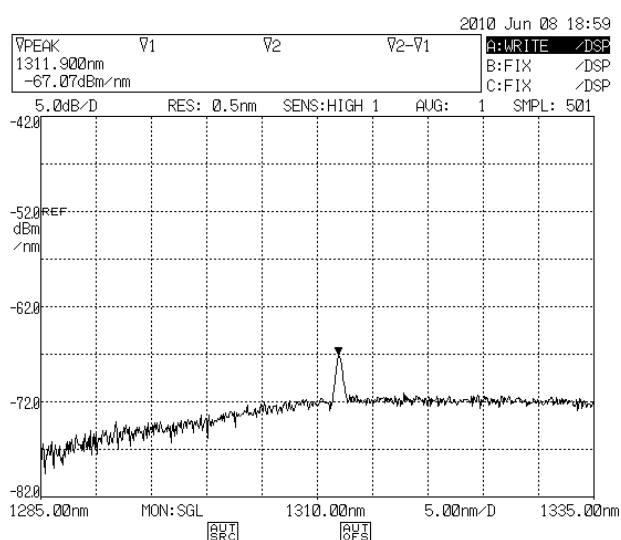
Figure 5.8 Reflection spectrum of the grating written in fiber with poly(MMA/BzMA 95/5 mol%) core and PMMA cladding (irradiation time 15 min)

5.2.3. **Influence of zeroth order diffraction of phase mask on PFBG inscription**

The phase mask for FBG inscription was normally required to have less than 5% zeroth order diffraction [1]. A theoretical analysis predicted that even 0.1% of zeroth order component would have substantial effects on the grating inscription [106]. In earlier period of this study, the failure of writing and observing Bragg gratings in POFs was ascribed to this effect, because the phase masks in Table 5.1 all have zeroth order larger than 0.1%, even for the phase masks designed for 325 nm. Other phase masks, four of which were not designed for 325 nm either, were used to fabricate gratings. However, later experiments show that all the phase masks wrote successfully gratings in polymer fibers except PM573. The grating produced by PM573 was not observed because the Bragg wavelength of the produced grating was beyond the wavelength range of available light sources. Figure 5.9 displays reflection peaks of gratings written by five phase mask in a single polymer fiber. The highest zero order diffraction is 38% for PM1058, two times higher than each first order. But PFBGs were written in fiber using it, and reflection intensity is on the same level to PM1047I, which is designed for 325 nm operation.
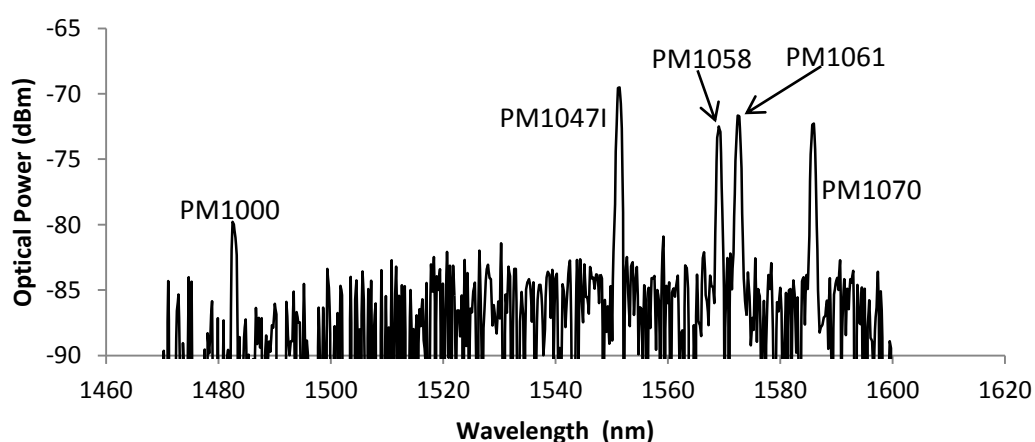
Figure 5.9 Reflection spectra of five PFBGs written on one fiber using PM1000, PM1047I, PM1058, PM1061, PM1070

Figure 5.10 shows the reflection spectrum of a grating written by using PM647, which has a zeroth order diffraction of 26%. The produced FBG has a peak wavelength at 962 nm, and a FWHM (full width at half maximum) of ~1 nm. As for PMMA based fibers, FBGs at this wavelength range are preferable to those at 1300 or 1500 nm because of lower attenuation. However, most fiber optic instruments operate around 1300 nm and 1550 nm, namely, O band and C band in fiber optic communication.
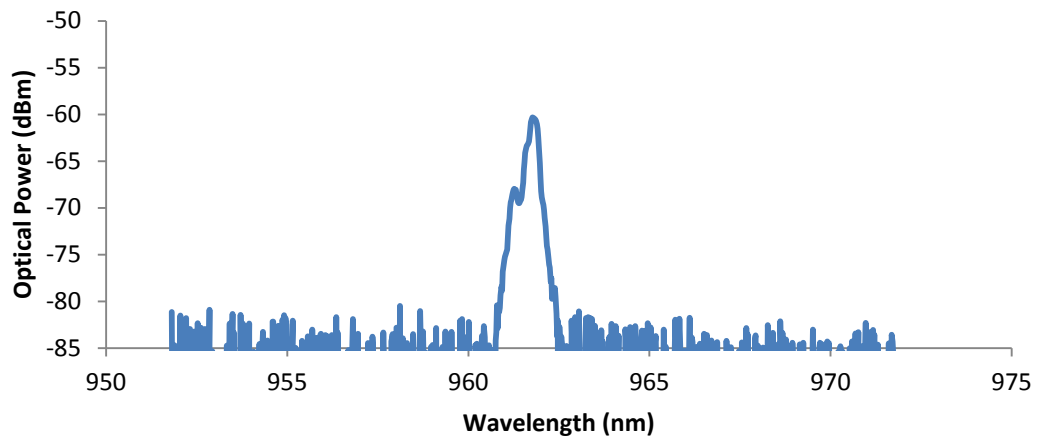
Figure 5.10 Reflection spectrum of a PFBG written by PM647

(a) (b)
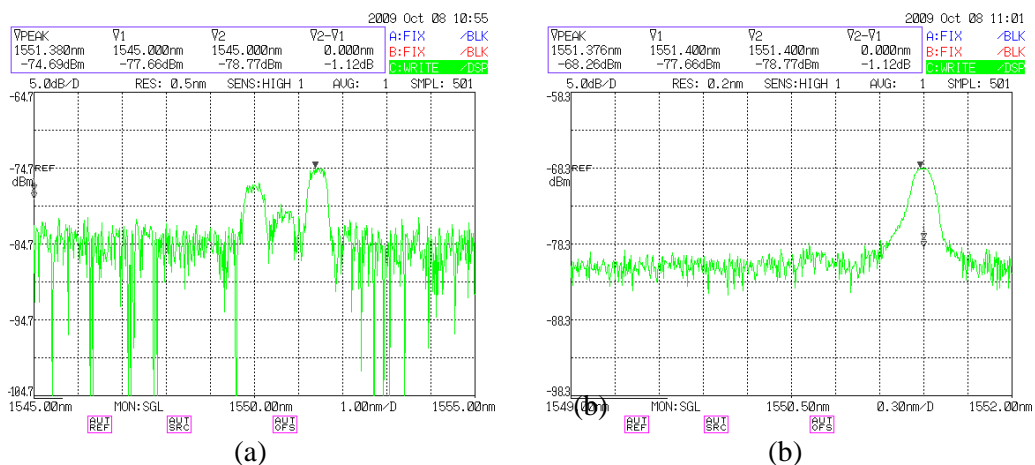
Figure 5.11 Two reflection spectrum (the screen shot of OSA) of a grating in 180 μm fiber under different coupling conditions

The spectrum in Figure 5.10 has a noticeable side peak, and more than one reflection peaks are also observed in many other experiments. These multiple peaks are thought to be due to the multi-mode nature of the used fibers [24, 25]. Figure 5.11 shows two reflection spectra of a PFBG in fiber of ~180 μm in diameter. When intensity of one peak was increased by adjusting position of the polymer fiber, another peak disappeared. It implies that multi-peak was due to multi-mode nature of the used fiber. Under certain coupling, the Bragg grating reflects light into various modes of the fiber so that multiple peaks were produced.

5.2.4. **Formation dynamics of PFBGs**

Figure 5.12 shows the reflection spectra of a grating during inscription using PM884 in a fully annealed fiber, which has a ~12 μm core of PMMA doped with 0.7 wt % TS and a ~130 μm cladding of poly(MMA/TFEMA 95/5 mol/mol). The Bragg wavelength and peak power change during the whole writing process are plotted in Figure 5.13. The whole formation process could be divided into two stages. The first stage consisted of the first 20 min of UV exposure. The reflection peak appeared immediately after the UV exposure started, and increased quickly within a few minutes, and reached a highest value. Only one peak was observed, and its bandwidth was less than 1 nm. Then the peak started to decrease, and the slight decrease continued for about 15 min. Then the second stage started. The Bragg peak started to increase quickly again and continued for 20 min, and the peak power was almost 10 dB higher than the previous highest value. In the mean time, the reflection spectrum broadens dramatically and many peaks appeared at shorter wavelength. After 40 min, the peak power of the reflection spectrum dropped very slowly, while the width broadened dramatically. Finally, the Bragg peak reduced to noise level.

The similar trend was recorded for inscription process using PM1047I and PM647. The result for PM647 is shown in Figure 5.14.
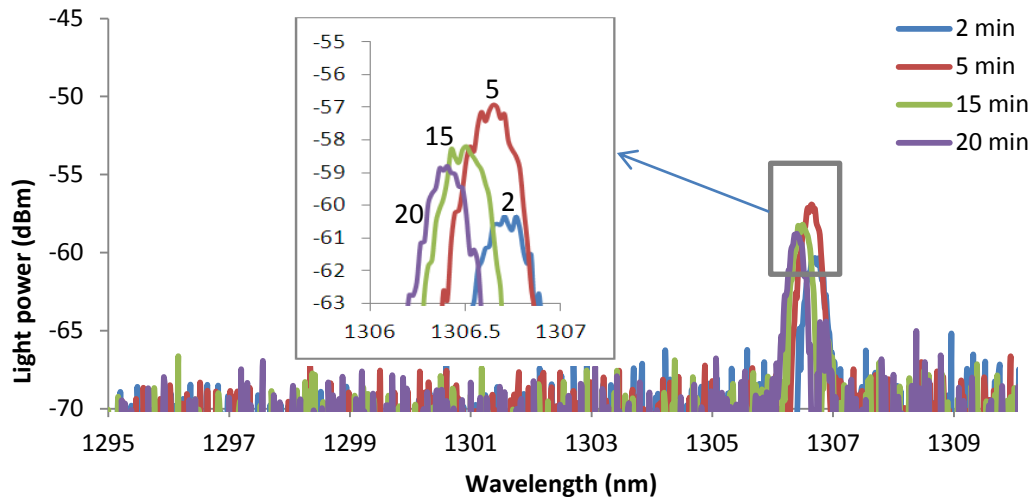
(a) For exposure time of 2, 5, 15, 20 min
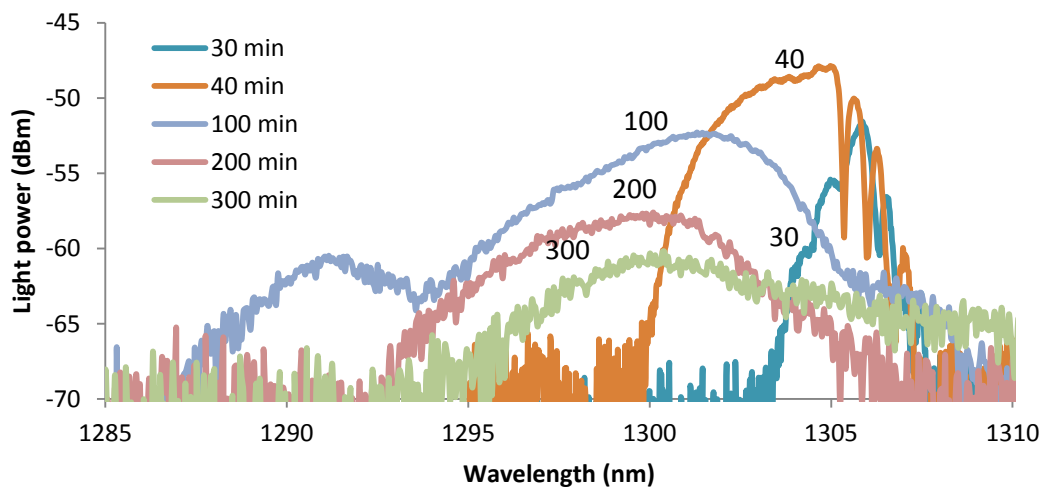
(b) For exposure time of 30, 40, 100, 200 and 300 min.

Figure 5.12 The reflection spectra of a grating during inscription at various writing time.
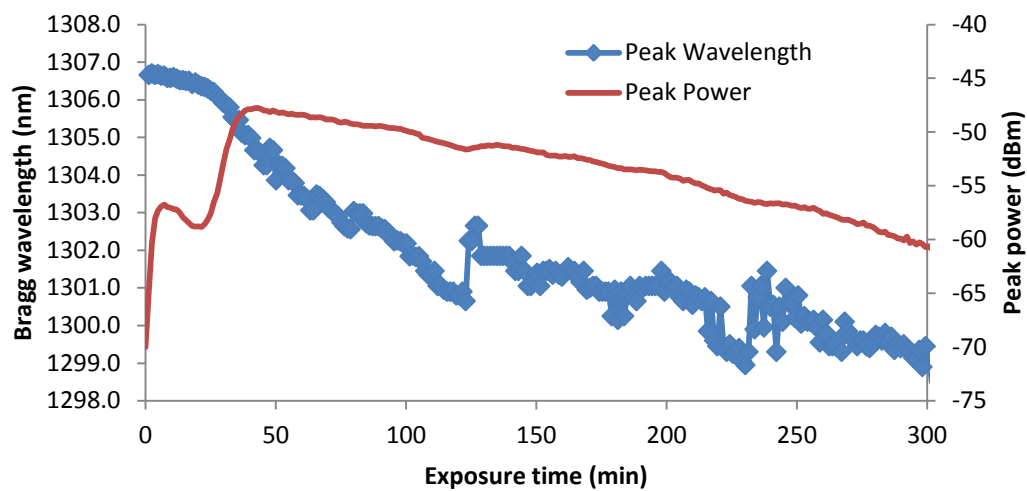
Figure 5.13 Bragg wavelength and peak power of a PFBG during phase masked UV exposure (PM884)
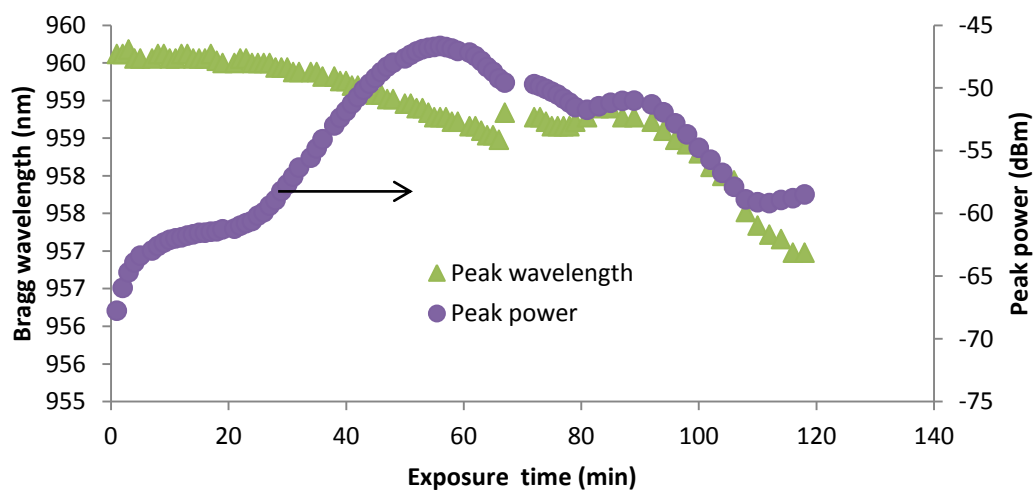
Figure 5.14 Bragg wavelength and peak power of a PFBG during phase masked UV exposure (PM647)

Complete picture for this formation dynamics cannot be given yet. Nevertheless, I will take effort here to explain. The rapid increase of the peak power immediately after UV exposure starts most likely arises from the photoisomerization of TS molecules. The subsequent decrease can be ascribed to the over irradiation, that is, photoisomerization of TS molecules within the destructive area of the interference pattern. An indirect evidence for this explanation is the Bragg wavelength shift and the calculated RI modulation. The Bragg wavelength shift is about 0.3 nm (1306.7 to

1306.4 nm) for the first 20 min of exposure (Figure 5.13). Based on this value, the RI

modulation is estimated as 2×10^{-4} using the following equation based on Bragg law

$$\Delta n = \Delta\lambda/(2\Lambda) \tag{5-1}$$

This value of index modulation is close to the index modulation on film doped with

0.7 wt % TS (3×10^{-4}).

The second peak of the Bragg peak power must associate with the laser-induced

effects on the host polymer—PMMA, because any photochemical effect on TS

molecules would not be able to cause a Bragg wavelength shift as large as 6 nm. A

doping concentration of 0.7 wt % TS increases the RI of PMMA by 1.5×10^{-3} as

previously measure, and the largest Bragg wavelength shift is only 1.3 nm even all

TS molecules are degraded. Large negative shift of Bragg wavelength after 20 min of

exposure suggests the main laser effect on PMMA is photodegradation. The decrease

after increase is also due to over irradiation and erase of Bragg gratings.

5.2.5. **Microstructure of PFBGs**

Figure 5.15 shows the microstructure of one grating written in polymer fiber using

PM884 after 60 min of exposure. Rather than a one-dimensional uniform grating, a

two-dimensional grating is observed. Two series of grating with the same period as

phase mask was observed along fiber axis while there is a half period shift between

them. The period along the grating depth (direction normal to the phase mask plane)

is measured to be 3.3 μm. However, the microstructure of a grating inscribed by

PM1047I exhibits a different pattern, as shown in Figure 5.16. A uniform one-

dimensional structure is observed, and the period of the grating equals to that of phase mask.
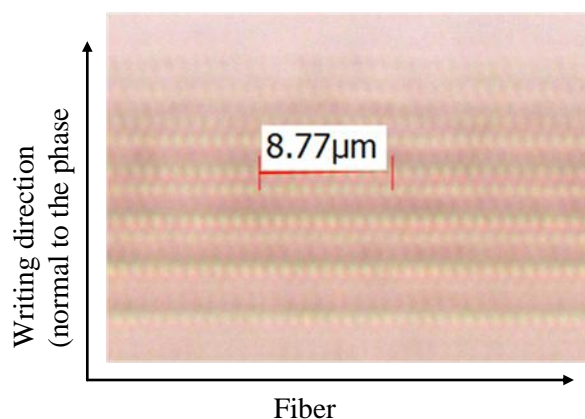
Figure 5.15 Micrograph of one grating written in polymer fiber with core of poly(MMA, 2.0 wt% TS) and cladding of poly(MMA/TFEMA 90/10 mol%) using 884 nm phase mask. The irradiance of writing is 2×10^4 mW/cm^2, and irradiation time is 60 min.
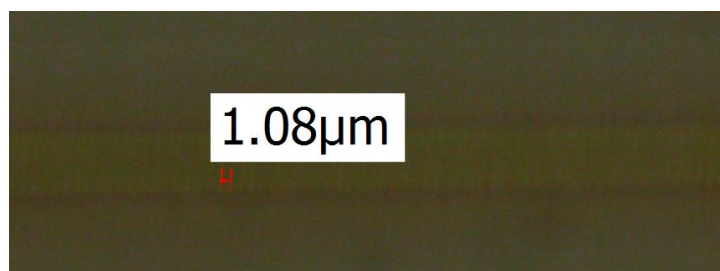
Figure 5.16 Micrograph of grating written in POF with core of poly(MMA, 2.0 wt% TS) and cladding of poly(MMA/TFEMA 90/10 mol%) using 1046.5 nm phase mask (Ibsen). The irradiance of writing is 2×10^4 mW/cm^2, and irradiation time is 60 min.

The above two micrographs of gratings were obtained after long time of irradiation at high irradiance. In the mean time, the cladding of the fiber is severely damaged, especially at the region that is close to the phase mask (Figure 5.17). Close observation shows many cavities and particles, suggesting the degradation of the cladding under long-time irradiation. This kind of damage is noticeable as early as 8 min after writing at this level of irradiance (2×10^4 mW/cm^2). Hence, the normal writing time at this irradiance is set at 5 min, though 40 min of writing produces gratings with much higher reflectivity.

(a) Fiber

(b) Cladding near surface
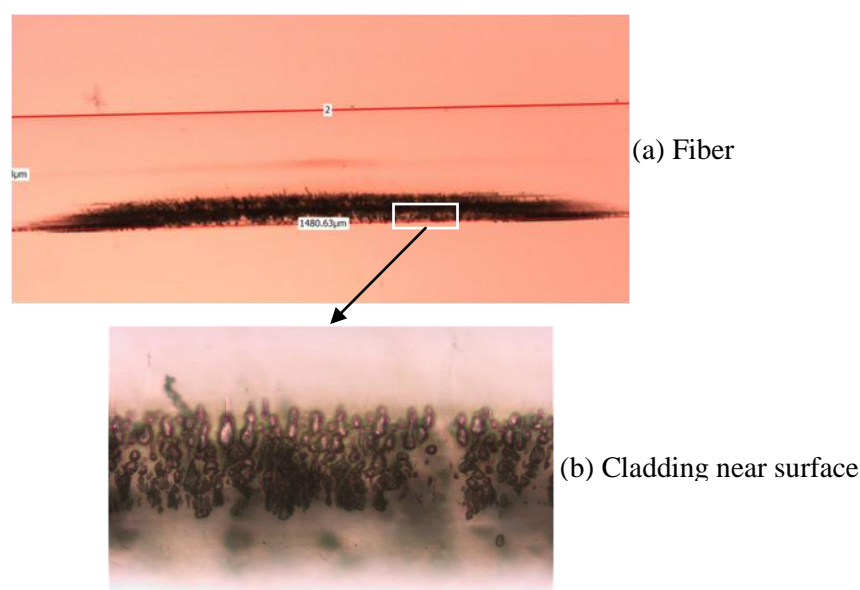
Figure 5.17 Degradation of fiber cladding under 325 nm laser at high irradiance of 2.3×10^2 mw/mm^2 (irradiated 40 min)

5.2.6. **Simulation of the near-field of phase masks**

To explain the observed microstructure and determine the influence of the zeroth order diffraction, the near-field of the phase mask was simulated. The simulation method in [143] was adopted. The near-field of the phase mask is regarded as the interference pattern of all diffraction orders. In the literature, the linewidth of the laser source is considered, but in our simulation, the effect of linewidth was not considered because the linewidth of the used He-Cd laser is fixed 0.35 pm. The laser source was also considered linearly polarized, since the used laser has high linear polarization ratio of 500:1. Another assumption is that the diffraction ration of +1 equals to that of -1, also for the second and third diffraction orders. This is reasonable due to the symmetry. Diffraction ratio of the phase mask was measured and used for simulation (Table 5.1).
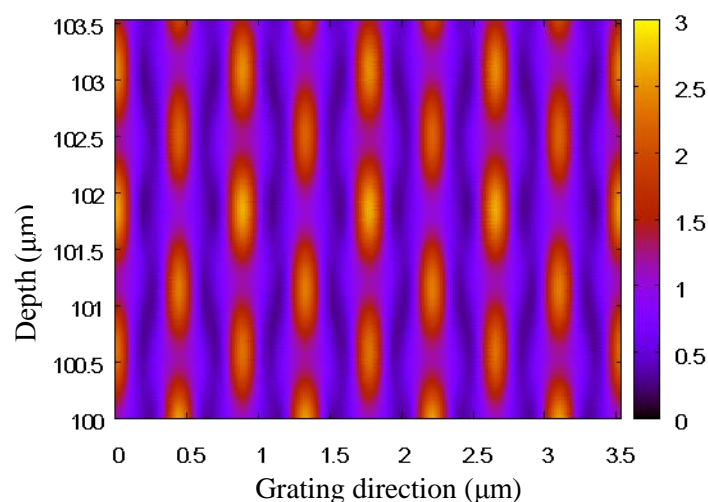
Figure 5.18 Simulated near-field of the PM884. Bright color represents high light intensity.

Figure 5.18 shows the simulation result of the PM884 considering all diffraction orders. The zeroth order diffraction of this mask is only 0.5 %, so the main influence is the second order diffraction (11% to each 2nd order). Due to the second order diffraction, the interference pattern is no longer parallel lines. The resulted pattern is much like the observed microstructure of Bragg grating written in some polymer fibers.

Figure 5.19 shows the simulated near field of the phase mask with 1046.5 nm pitch. The simulation result suggests that the period the near filed is half of the phase mask, which is different to the experiment result obtained from Figure 5.16. This phase mask diffracts most light into the first order with little light to other orders (0th order 0.6%, 2nd order 3.2%, 3rd 6.3%), therefore the interference pattern is dominated by laser in +1 and -1 order, and according the period of pattern is half of phase mask pitch. Nevertheless, the impact of other orders is still noticeable, and the light intensity along each constructive interference fringe is not evenly distributed.
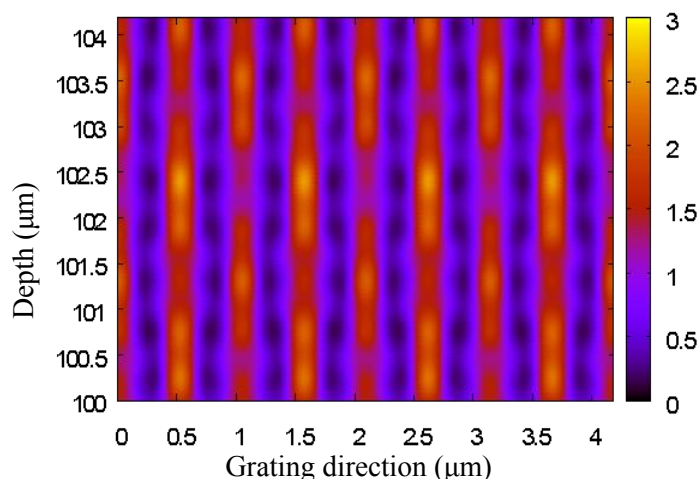
Figure 5.19 Simulated near-field of the PM1047I. Though the intensity along each fringe is not uniform, the major period of the pattern is equal to half of the phase mask pitch.

5.2.7. **Estimation of index modulation of fiber core by UV exposure**

The reflectivity of the fabricated gratings is rather low compared to the value predicted by the RI modulation measure on film. Figure 5.20 shows the transmission spectrum of a grating (10 cm in length) with a relatively high reflectivity. The reflectivity is -4 dB, which is about 60% reflection. The maximum reflectivity (first order) of uniform Bragg grating follows

$$R = tanh^2 \left(\frac{\pi \, \Delta n \, \eta(V)}{\lambda} L \right)$$

(5-2)

Where R is reflectivity, which is 0.6 for the grating in Figure 5.20; Δn is the modulation of refractive index; $\eta(V)$ represents the fraction of the integrated fundamental-mode intensity contained in the core; L is the grating length, 10 mm here. For rough estimation, η(V) is assumed to be unit here. Based on the above assumption, the index modulation in the grating was estimated to be 5×10^{-5}. This value is almost one order lower than the value measured on film. The RI modulation on 0.7 wt% TS doped PMMA film was measured to be 3×10^{-4}. The reason might be

photoisomerization of the TS even in the destructive interference region due to the influence of other order diffraction other than first order.

Many other experiments were tried to write gratings with high reflectivity, but none of them is higher than the one in Figure 5.20. Figure 5.21 shows the result of an even longer grating (15 mm), and Figure 5.22 displays the result of a grating at 1307 nm. Though reflection can be observed in transmission spectra, the reflectivity is less than 3 dB. Moreover, the repeatability of these experiments is low, and the main reason is definitely the deviation for fiber samples, though the quality of the fabricated fibers has been improved significantly.
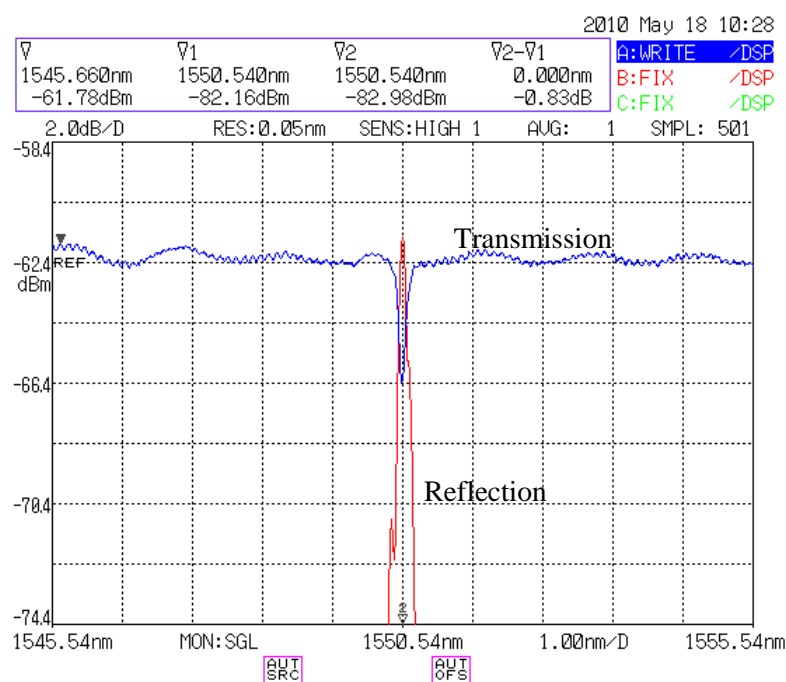
Figure 5.20 Transmission and reflection spectra of a grating written in polymer fiber, which has the core of poly(MMA/BzMA 95/5 mol%, 0.7 wt% TS) and 150 μm cladding of PMMA. The grating written by scanning technique is 10 mm in length.
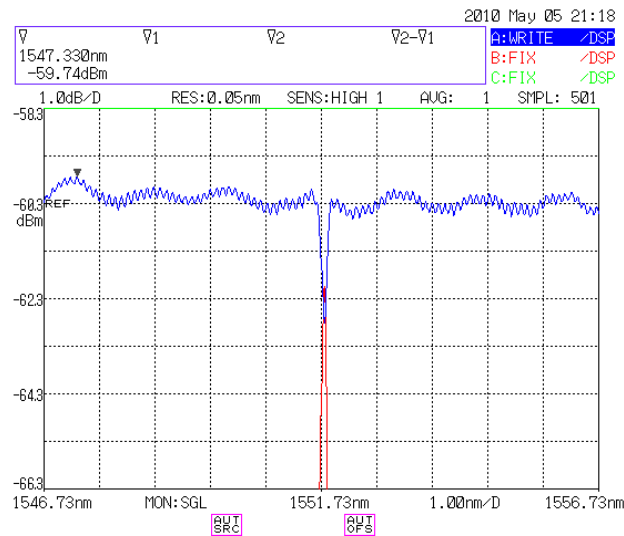
Figure 5.21 Transmission and reflection spectra of a grating (fiber diameter 120 μm. Grating length 15 mm. Scanning speed 2.5 μm/s).
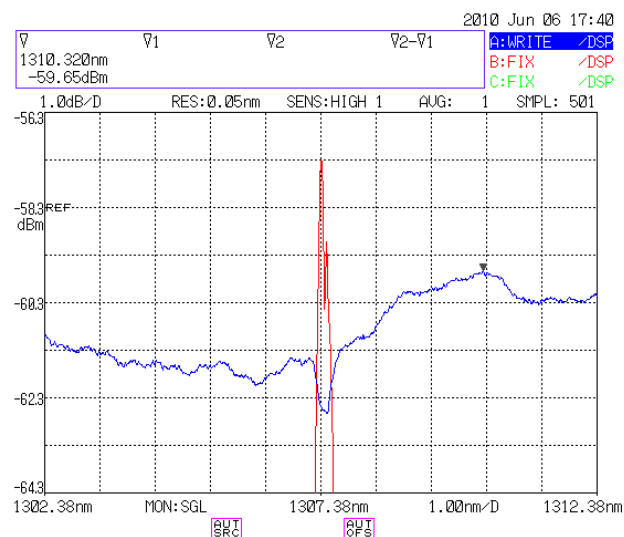
Figure 5.22 Transmission and reflection spectra of the grating at 1307 nm

5.2.8. **Relaxation of PFBGs after UV exposure**

It was noted that the Bragg peak of the fabricated gratings faded away immediately after inscription and then recovered slowly, as shown in Figure 5.23. Similar phenomenon, referred as relaxation, has been well studied for the laser-induced holographic gratings in polymer films doped with azobenzene [59, 61, 144]. Since this fading and recovery process is closely related to the grating formation, the

phenomenon was examined in detail in order to reveal the physical or chemical process behind.

Figure 5.23 shows the relaxation of a PFBG after 5 min of phase masked exposure. The reflection peak of the grating grows rapidly during writing. After exposure, the peak power decreases steadily, and the Bragg peak vanishes after 5 h. However, the reflection peak appears about 12 hours after inscription and becomes strong over dozens of hours. The Bragg wavelength did not change significantly considering the resolution of the wavelength measurement (50 pm) and the fluctuation of room temperature, and also relative humidity that was later found having tremendous impact on the PFBGs.
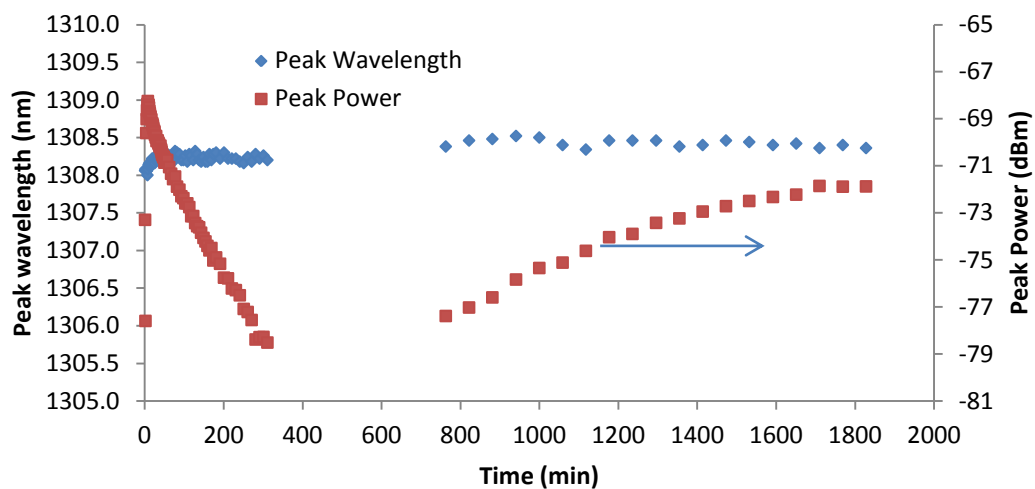
Figure 5.23 Bragg wavelength and peak power a PFBG during 5 min of writing and after it.

Firstly it was thought that this relaxation process might occur particularly for the grating that had been written for 5 min. However, it also occurred for grating that had been written for 1, 15, and 30 min, as shown in Figure 5.24. The gratings written for 1 or 5 min almost completely disappeared after 300-400 min and fully recovered. The grating written for 15 min faded at lower speed and recovered its reflectivity

very slowly. The grating written for 30 min decreased at the same speed as those written for 1 or 5 min, but recovered extremely slowly. Its peak power completely returned almost two weeks after inscription.
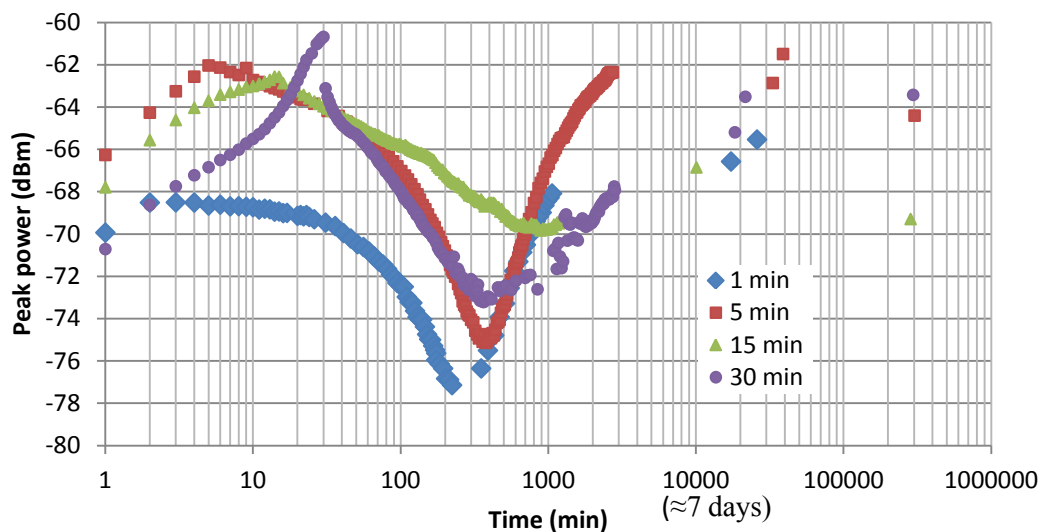
Figure 5.24 Peak power of Bragg reflection for four gratings that had been written for 1, 5, 15, and 30 min. The peak power of the grating that had been written for 30 min jumped after inscription was due to reduced butt-coupling between the polymer fiber and the silica fiber during handling.

The same relaxation process was observed for the grating at other Bragg wavelength ranges. Figure 5.25 shows the case for a grating of 960 nm. The fading time, from the time of stopping UV exposure to the Bragg peak dropping to the lowest, was slightly shorter than that for the grating around 1310 nm. After the relaxation process, the power of the Bragg peak returned to the value immediately after UV exposure.

The grating written in fibers without annealing treatment exhibited the same behavior, as shown in Figure 5.26. The peak of the Bragg reflection reduced to the noise level 6 h after writing, and fully recovered after two days.
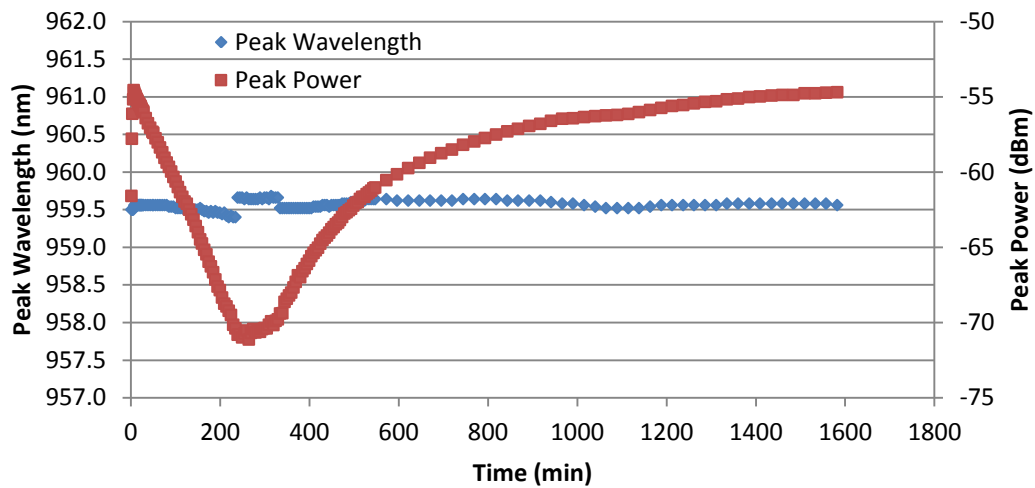
Figure 5.25 Wavelength and power of the Bragg peak for a grating at 961 nm during and after inscription. Bragg peak decreased to the lowest level 4 h after inscription, and rose to the level after writing after almost two days.
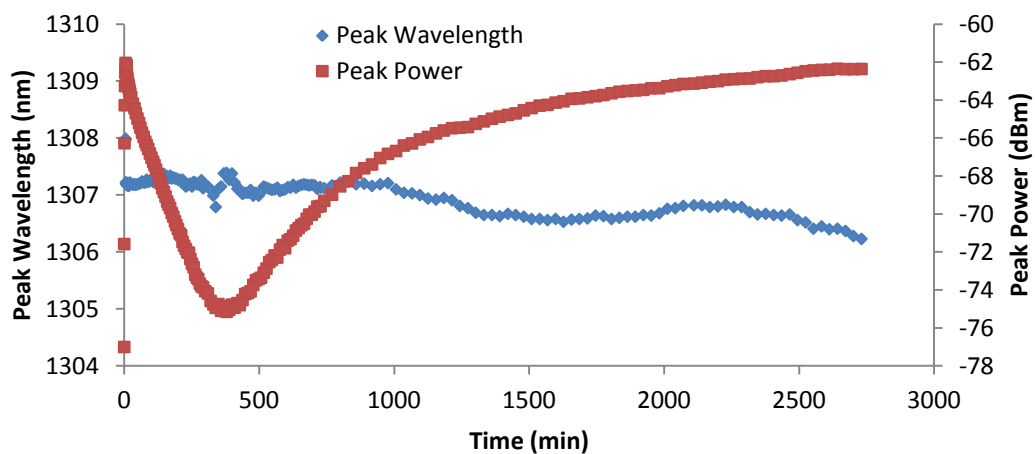
Figure 5.26 Wavelength and power of the Bragg peak for a grating written in an as-drawn fiber, i.e. without annealing treatment.

The above results show that the relaxation process (fading plus recover) took one to two days, and during this period of time the grating had not reached the steady state. Consequently, the fabricated gratings could not be used or tested, or the result would not be reliable. Waiting two days for the inscribed gratings to reach steady state is acceptable, but speeding up this relaxation process is more desirable. The most intuitive measure to speed up the relaxation process was to heat the fabricated gratings, for almost any chemical or physical process is accelerated at elevated

temperature. Hence, the fabricated gratings are heated to two temperatures—40 and 60 ℃, about half an hour after writing. The relaxation processes at two respective temperatures are shown in Figure 5.27 and Figure 5.28. Obviously, the relaxation process was significantly accelerated by heating the fabricated gratings. It took less than 100 and 40 min for the inscribed grating to reach the lowest level, and the whole relaxation process completed within about 10 h and 2 h at 40 and 60 ℃, respectively. For the grating heated to 60 ℃, the peak power of its Bragg peak started to rapidly decrease when the temperature reached approximately 50 ℃. As for Bragg wavelength, it instantly shifted towards shorter wavelength during temperature increasing. The shift of the Bragg wavelength was about 1.5 nm for the grating that is heated from room temperature (23 ℃) to 40 ℃, and about 3.0 nm for the grating heated up to 60 ℃. This large wavelength shift was later found to be due to the RH decrease caused by increased temperature, for the RH was not controlled during these two experiments.
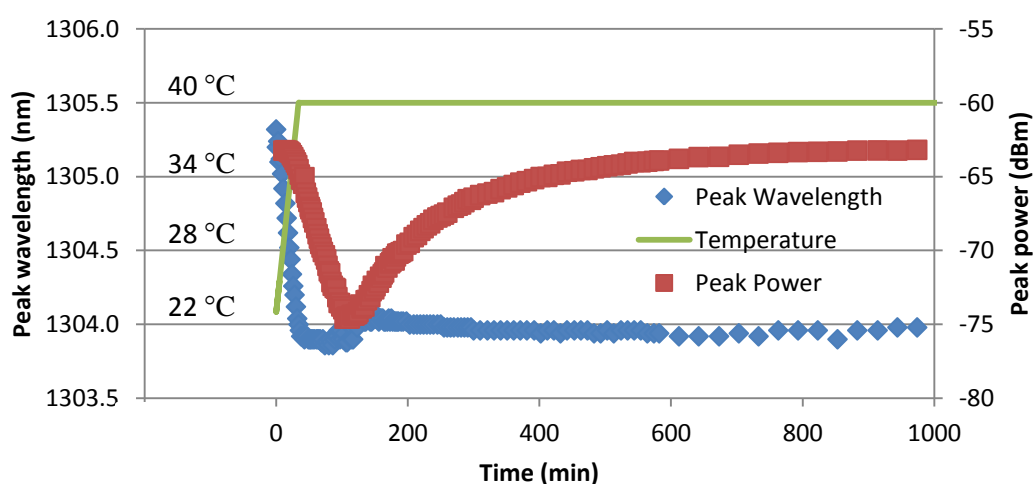
Figure 5.27 Relaxation of a fabricated grating at 40 ℃. The grating was written for 5 min, and then heated from room temperature to 40 ℃ within 30 min in the climate chamber without controlling relative humidity.
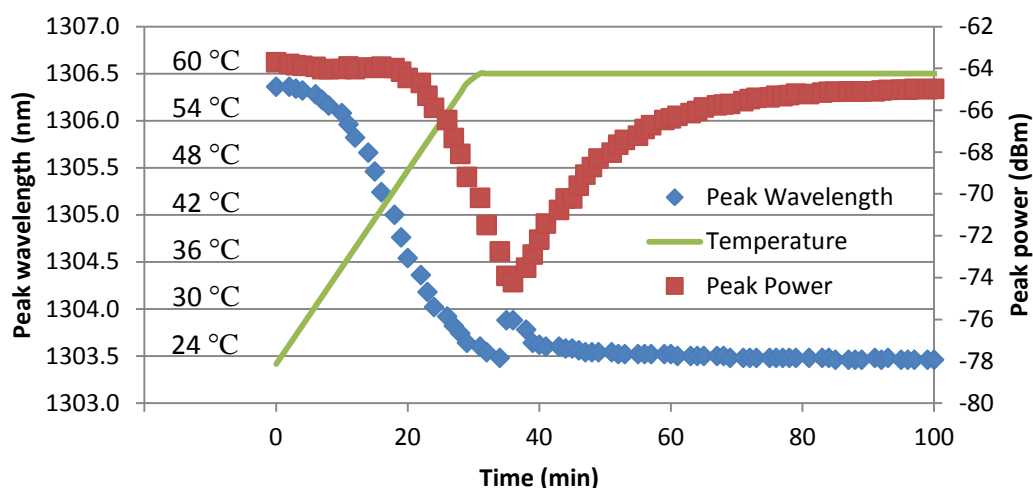
Figure 5.28 Relaxation of a fabricated grating at 60 ℃. The grating was heated from room temperature to 60 ℃ within 30 min and the temperature was remained 100 min.

To reveal relaxation mechanisms, several hypotheses were proposed and tested. The first speculated causes for this relaxation process is the moisture effect. To test this hypothesis, an as-inscribed grating was placed in a glass bottle dried by CaH_2 at room temperature, and the Bragg wavelength and peak power change is plotted in Figure 5.29. After the as-inscribed grating was placed in the dried bottle, the Bragg peak shifted towards shorter wavelength, from 1308 to 1304 within ~100 min. This blue-shift of Bragg wavelength was caused by moisture desorption. During this moisture desorption process, the peak power increased slightly at first, but decreased almost to the noise level of the OSA. This fading process took as long as 1000 min (≈17 h). Though the grating finally completely recovered, the recovery process took almost one week. The peak power of the reflection spectrum maintains constant two month later. This experiment suggests that the relaxation process is not solely caused by moisture sorption or desorption, meanwhile it shows that the relaxation process is accelerated by presence of moisture.
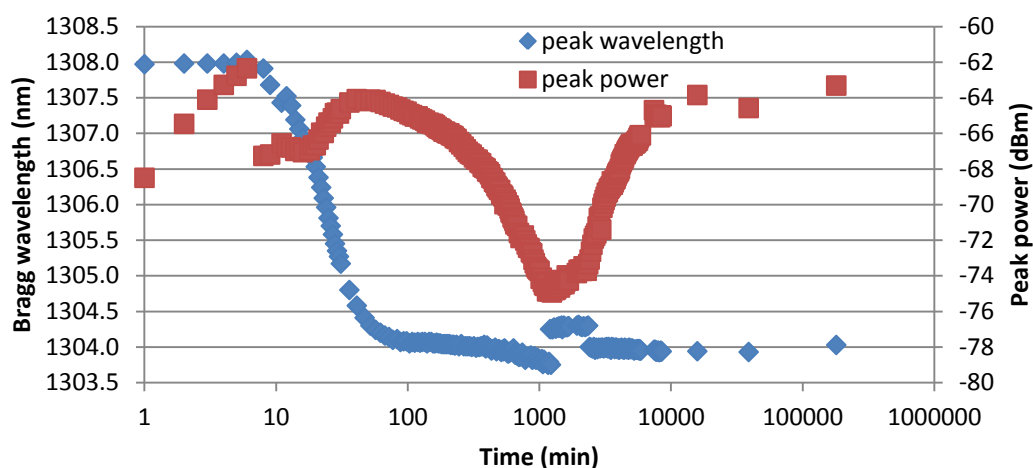
Figure 5.29 Relaxation of an as-inscribed grating at dry conditions. The grating had been written for 5 min. after writing. The grating was placed in a sealed bottle immediately after writing. The jump of peak power after writing is due to slight damage to butt-coupling.

The second hypothesis was that the relaxation process was caused by the diffusion or desorption of the volatile small molecules produced by photodegradation of fiber core. As-inscribed grating was vacuumed for 150 min a few minutes after inscription. The purpose of vacuuming is to accelerate the diffusion and desorption of small molecules, if those small molecules were produced. The wavelength and power of the Bragg peak was monitored in the whole process except during vacuuming, as shown in Figure 5.30. The Bragg peak returned to the original wavelength at 120 min, while the peak power decreased continuously for 300 min, then increase again. This relaxation process is essentially identical to the gratings at ambient conditions without vacuuming except delayed by 150 min of vacuuming. In short, the hypothesis of the diffusion and desorption of volatile small molecules produced by photodegradation during grating inscription does not hold.
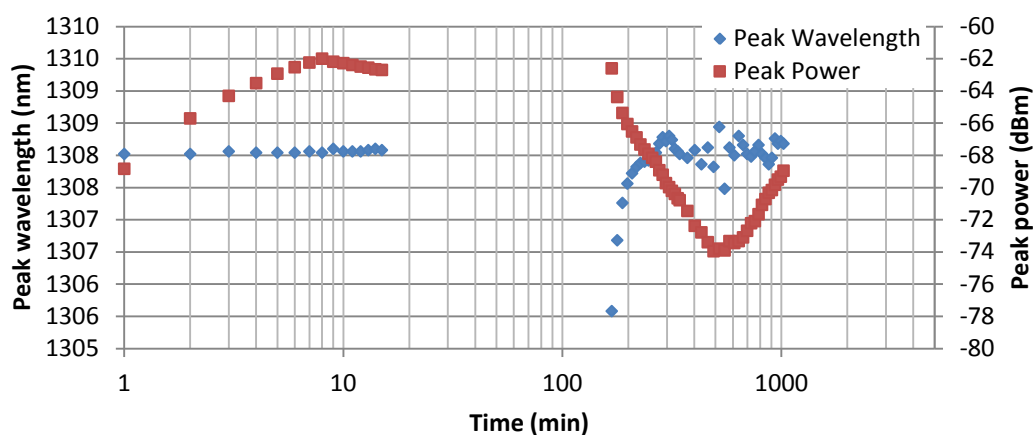
Figure 5.30 Relaxation of a grating after vacuuming. The grating was written for 8 min then vacuumed for 150 min.

The third hypothesis was the recovery of photo-active dopants. Literature reveals that the dye doped PMMA recovered after photodegradation, which was a time-dependent process similar to the relaxation process of PFBGs after inscription [145-148]. Fluorescence or amplified spontaneous emission of dye doped PMMA were found to partially or completely recover after photobleaching depending on dye types [145-147]. Fluorescence spectrum of Rhodamine B doped PMMA filer partially recovered its loss after intense laser irradiation [145]. The amplified spontaneous emission of PMMA doped with Disperse Orange 11 fully recovers after a couple of days [148].

However, the experimental result suggests that TS in POFs was not produced or formed during the relaxation after UV exposure. As shown in Figure 5.31, a POF was irradiated by laser beam directly, while the power of the fluorescent light at 406 nm was monitored by an OSA. The fluorescent power is an indirect measure of the concentration of TS because TS molecules absorb most light at 325 nm and emit fluorescent light. At beginning of irradiation, trans to cis photoisomerization dominated because most dopants existed in trans configuration and absorptivity of

325 nm light by trans isomer was much higher than that of cis isomer. As cis concentration increased, the trans-to-cis and cis-to-trans isomerization reached equilibrium. Within 50 s of irradiation the fluorescent light decreased almost 10 dB. As a rough estimation, the TS concentration decreased by 10 times. After 50 s of irradiation, the fiber was re-irradiated after one day, which was the typical completion time of the relaxation process at ambient conditions. The fluorescent light power of the second irradiation was almost equal to the value at end of the first irradiation, suggesting that TS concentration was invariant during the time between two irradiations. That is to say, no TS molecules were produced. This is consistent with the absorption spectrum study of the TS doped PMMA film on glass slide under UV irradiation, which revealed that the absorption spectrum of TS doped PMMA film after irradiation did not change upon the film being heated up to 80 ℃. The reason for this stability of *cis*-4-stilbenemethanol is the high activation energy of the thermal transition from cis to trans isomers, as has been discussed in Chapter 2.
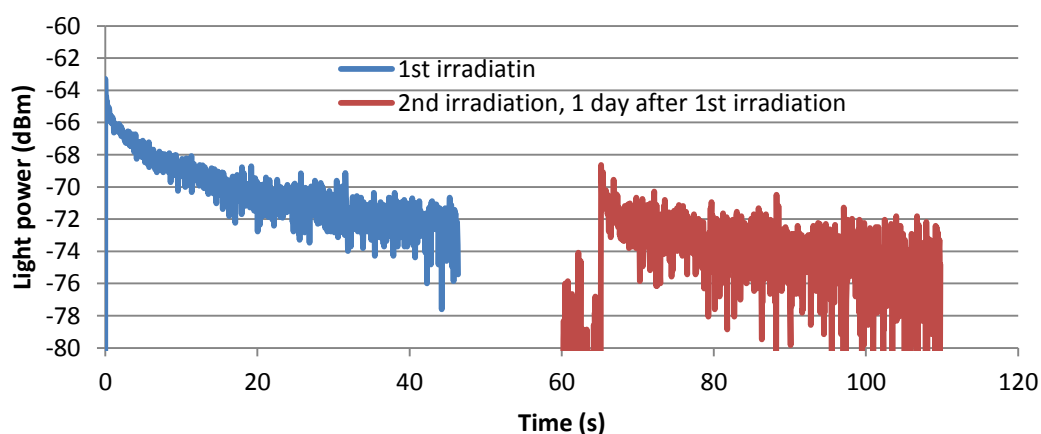
Figure 5.31 Fluorescent light power at 406 nm of the fabricated POF excited by laser without phase mask

The fourth possible reason for the relaxation after inscription is the release of the residual stress induced by photomechanical effect of the trans-to-cis

photoisomerization. Molecular simulation suggested that Connolly solvent-excluded volume of cis-4-stilbenemethanol was 2.5 % larger than that of TS, moreover, their geometries differed markedly (Table 5.3). Two benzene rings of TS molecule are in the same plane, whereas they are twisted with an angle in cis isomers. This means at least one benzene ring moves during photoisomerization. When TS molecules are doped in solid PMMA, the movement of benzene ring will exert force on macromolecules, producing mechanical stress on them. After irradiation or PFBG inscription, the spontaneous release of the residual stress leads to the change in effective refractive index, and hence the reflectivity of PFBGs and power of Bragg peaks.

Table 5.3 Molecular structure and volume of trans and cis configuration of 4-stilbenemethanol simulated by Chem3D Ultra 8.0

	trans-4-stilbenemethanol	*cis*-4-stilbenemethanol
3D model in free space filling mode		
Connolly Solvent Excluded Volume	180.62 A^3	185.11 A^3

5.2.9. Annealing induced Bragg wavelength shift of PFBGs

Bragg wavelength of PFBGs in PMMA fibers has been found to shift permanently at elevated temperatures [99, 105], and this is a stability issue in terms of PFBG applications. To prevent this phenomenon, the polymer fibers can be annealed before grating inscription, or gratings in polymer fiber can be annealed. The annealing process results in permanent shift of Bragg wavelength shift of PFBGs so that this relaxation process will not occur during application.

(a)   (b)
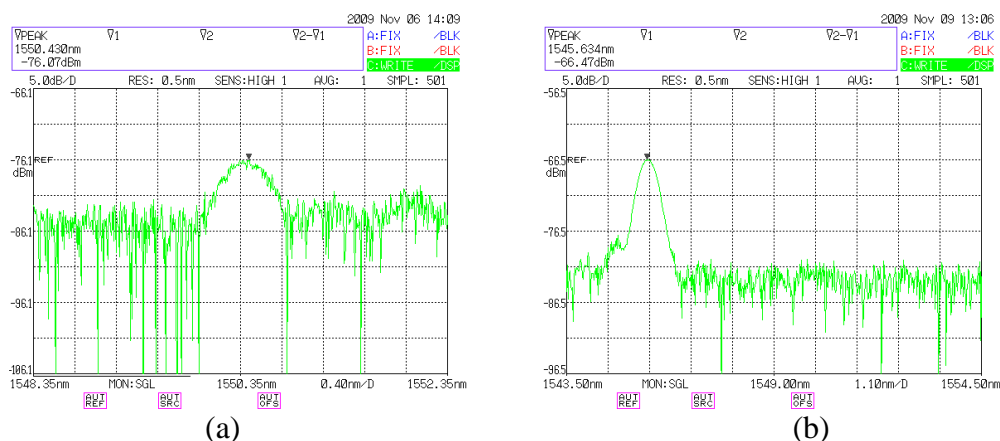
Figure 5.32 Reflection spectrum of a PFBG (a) before and (b) after one annealing cycle

Figure 5.32 shows the reflection spectra of a fabricated polymer FBG before and after annealing treatment. The Bragg peak shifted about 5 nm toward shorter wavelength. The shift of Bragg wavelength is due to the shrinkage of fiber during annealing. The shrinkage of the fiber heated at high temperature is evident, and also has been reported [12].

The above result only shows one annealing cycle, and it was found that the PFBGs still permanently shifted under further annealing. Figure 5.33 shows two samples of grating annealed for more than 40 times. Although the largest shift occurred during the first annealing, the reflection peak became stable after about 20 annealing cycles. And also, there is big variance between these two samples in terms of the shift of Bragg wavelength. The total wavelength shift of two samples is 20 nm and 35 nm, respectively. The large difference is also mainly caused by the variance in the fabricated fibers. A shift of 35 nm for 962 nm grating equals to shrinkage of 3.6% for the fiber. Considering this large shrinkage, the fabricated POFs were annealed for at least 20 times for grating inscription except specially noted.
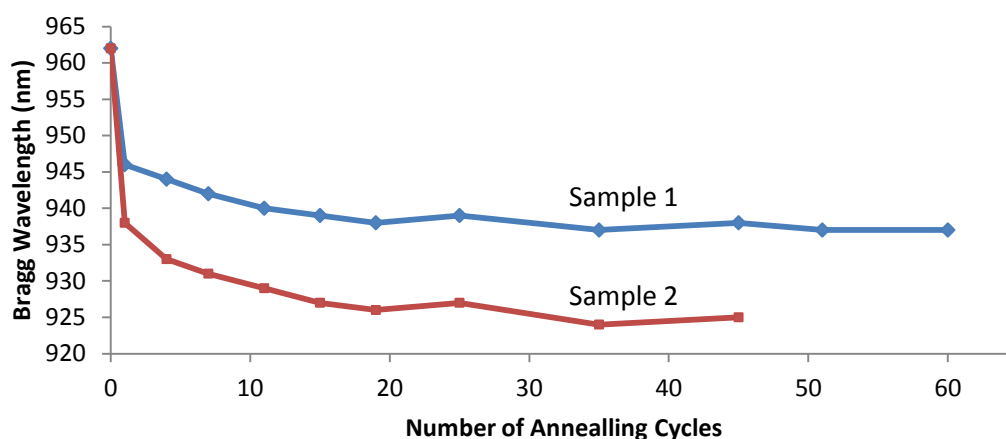
Figure 5.33 Bragg wavelength shift of two grating samples after repeated annealing

5.2.10. **Thermal response of PFBGs**

The thermal response was measured at ambient conditions, that is, PFBGs were heated on a Peltier device in an open space (Figure 5.7). It was found later that the result obtained by this method was not accurate, because the surrounding relative humidity, which was found having significant impact, would be changed by heating. Yuan and co-workers measured the RH above a resistive heater during increasing temperature; they found that the RH decreased from 66% at room temperature to 44% at 36 ℃ [149]. In order to avoid this uncontrolled variation, the thermal response was measured at constant relative humidity in a climate chamber, which controlled relative humidity within 10%-98% for temperature from 10 to 90 ℃. To measure the intrinsic temperature sensitivity of PFBGs, a PFBG was sealed in a test tube dried by CaH_2 and the test tube was heated in a water bath. Thermal response at these conditions will be discussed individually as follows.
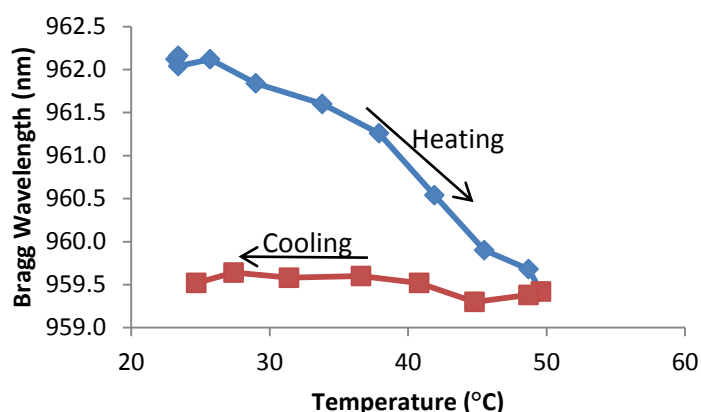
Figure 5.34 Thermal response of a PFBG in as-drawn polymer fiber

5.2.10.1. At ambient conditions

Figure 5.34 shows the thermal response of a PFBG in as-drawn polymer fiber heated and then cooled on the Peltier device. Upon heating, the Bragg wavelength shifted toward shorter wavelength as expected from the negative thermo-optic coefficient of PMMA. From 25 to 50 ℃, the Bragg wavelength shifted approximately 2.5 nm. However, the Bragg wavelength kept unchanged during cooling. This permanent wavelength shift of FBGs in as-drawn POFs upon heating has been reported [99, 105], and the reason was the release and thermal shrinkage of residual stress in fiber. Hence, as-drawn fibers were always annealed to remove the residual stress.

Figure 5.35 shows the thermal response of a PFBG written in fiber annealed for 23 times. The grating was heated from 21 to 48 ℃ within 60 min, while Bragg wavelength shifted from 961.3 to 959.8 nm. Then the temperature of the FBG was maintained for 40 min, and no shift of Bragg reflection peak was observed. After this isothermal process, the fiber was cooled to room temperature within another 60 min, but the Bragg wavelength did not simultaneously shift back to the original wavelength. It took more than 3 h for the Bragg peak to return to 961 nm. The first doubt for this slow back shift was the slow heat transfer between the surface of the

Peltier device and the fiber. Therefore, the cooling process was prolonged to 210 min, but still the Bragg peak did not fully recover after temperature was decreased to room temperature (Figure 5.36).
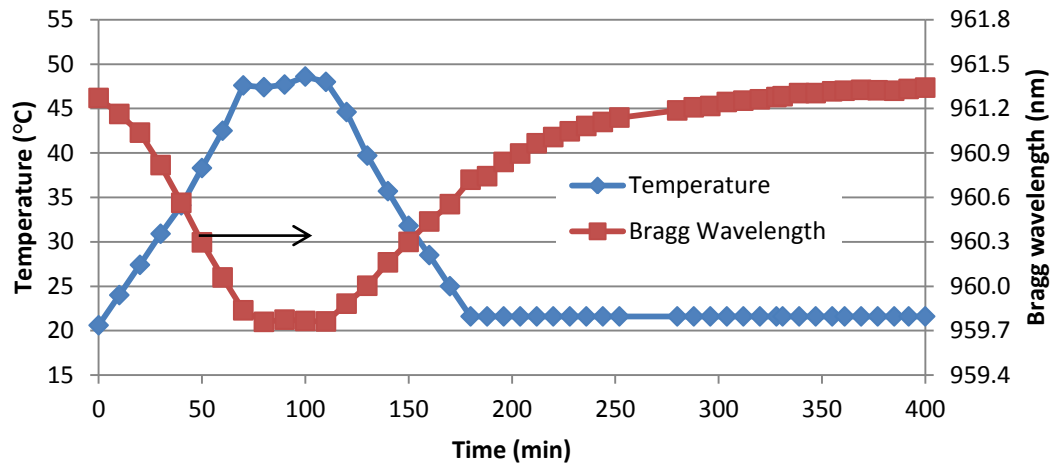
Figure 5.35 Thermal response of a PFBG in fiber after being annealed for 23 times
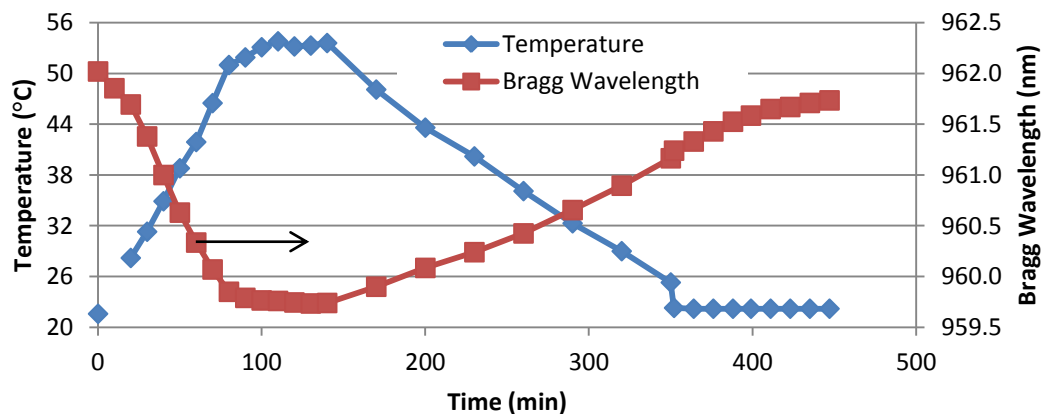
Figure 5.36 Thermal response of a PFBG written in fiber annealed for 23 times. Temperature of the fiber was slowly decreased from 53 ℃ to 22 ℃ within 210 min

Initially, this slow back-shift after thermal cycling processes was attributed to the slow shrinkage of the fiber after thermal expansion. In order to accelerate the shrinkage of the fiber, the fiber was embedded in epoxy resin, so that contract of epoxy could force the fiber shrink due to high modulus of epoxy and strong adhesion between epoxy and the fiber. Thermal response of two PFBGs embedded in epoxy

resin was illustrated in Figure 5.37 and Figure 5.38. One of them was written in fiber without annealing (Figure 5.37), and the other one was written in fiber annealed 20 times (Figure 5.38). After embedded in epoxy, Bragg peaks of two polymer PFBGs could return to the original wavelengths after a heating-cooling cycle, regardless of annealing treatment on POFs.

By this approach, the Bragg wavelength shift of PFBGs become reversible. Therefore the temperature sensitivity of embedded PFBGs was measured on the Peltier device, and the result is shown in Figure 5.39. Temperature sensitivity of a PFBG at 959 nm was measured as 110 pm/℃. This value is not the intrinsic temperature sensitivity of the fabricated FBGs since the fiber was embedded in epoxy resin, and the thermal expansion of the fiber was restricted by expansion of epoxy. Epoxy, on the other hand, delays variation in moisture content of the polymer fiber core. Nevertheless, this sensitivity value seems promising. It is one order of magnitude higher than that of FBGs in silica fiber (~10 pm/℃).
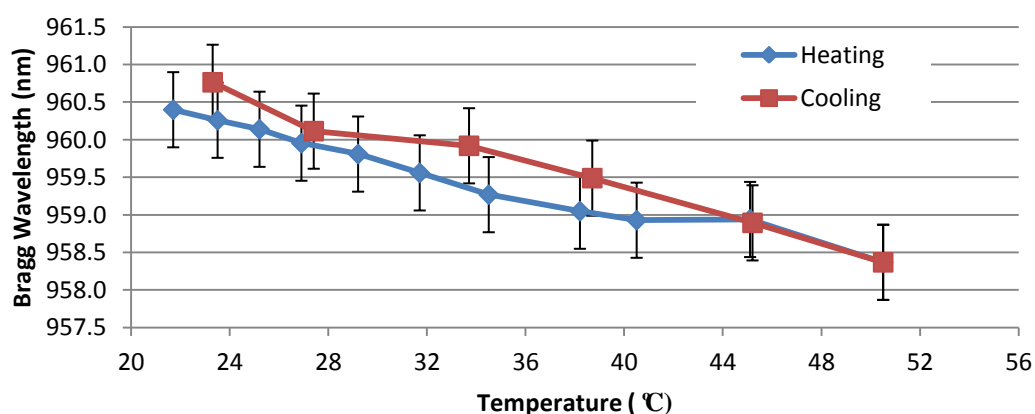
Figure 5.37 Thermal response of a PFBG embedded in epoxy. The grating was written in fiber without annealing treatment.
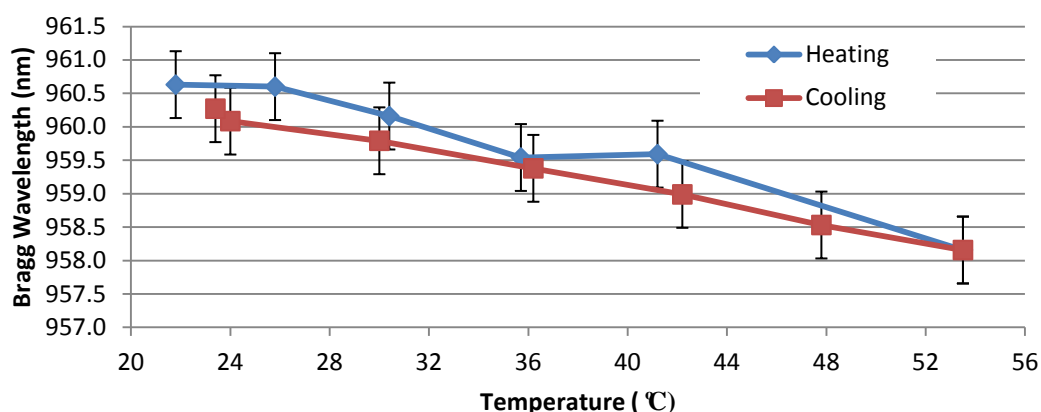
Figure 5.38 Thermal response of a PFBG embedded in epoxy. The grating was written in fiber annealed for 20 times
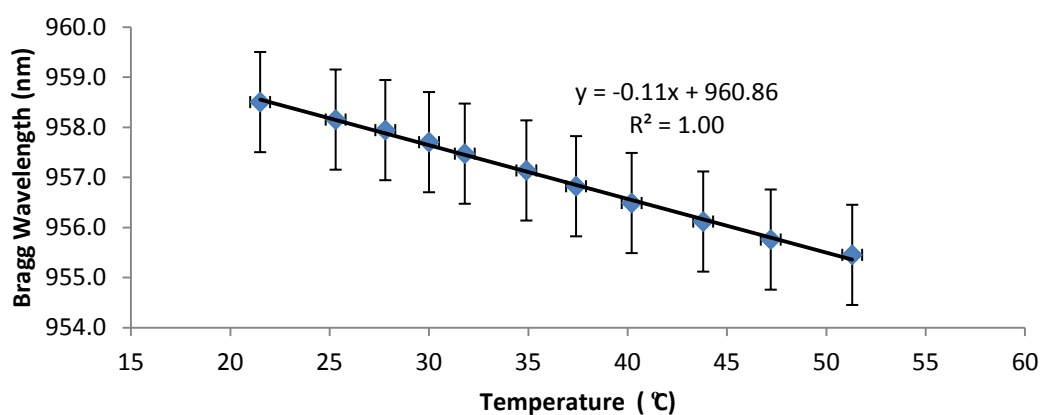
Figure 5.39 Temperature sensitivity of a PFBG at 959 nm embedded in epoxy resin

5.2.10.2. At constant relative humidity

After realization of the strong influence of moisture on PFBGs, temperature sensitivity was measured at constant RH. Temperature sensitivity of three PFBGs in a single fiber was measured at 60% RH. The grating shifts are quiet linear with temperature within the studied range. The three gratings have Bragg wavelength at 958, 1305, and 1545 nm, respectively, at 20 ℃ and 60% RH. Their temperature sensitivities are shown in Figure 5.40. Linear fitting shows that the temperature sensitivity ($\Delta\lambda/\Delta T$) was -6.4 pm/℃, -8.7 pm/℃ and -13.7 pm/℃ for three gratings, respectively. These values are almost one order lower than the values measured

without controlling humidity, suggesting that if moisture was not controlled, the grating shift might be mainly induced by reduced moisture pressure during temperature increase. Based on the sensitivity and Bragg wavelength, the calculated specific temperature sensitivity $((\Delta\lambda/\Delta T)/\lambda))$ was -6.7, -6.7 and -8.9 pm $\cdot °C^{-1} \cdot \mu m^{-1}$ for three gratings at 958, 1305 and 1545 nm, respectively.
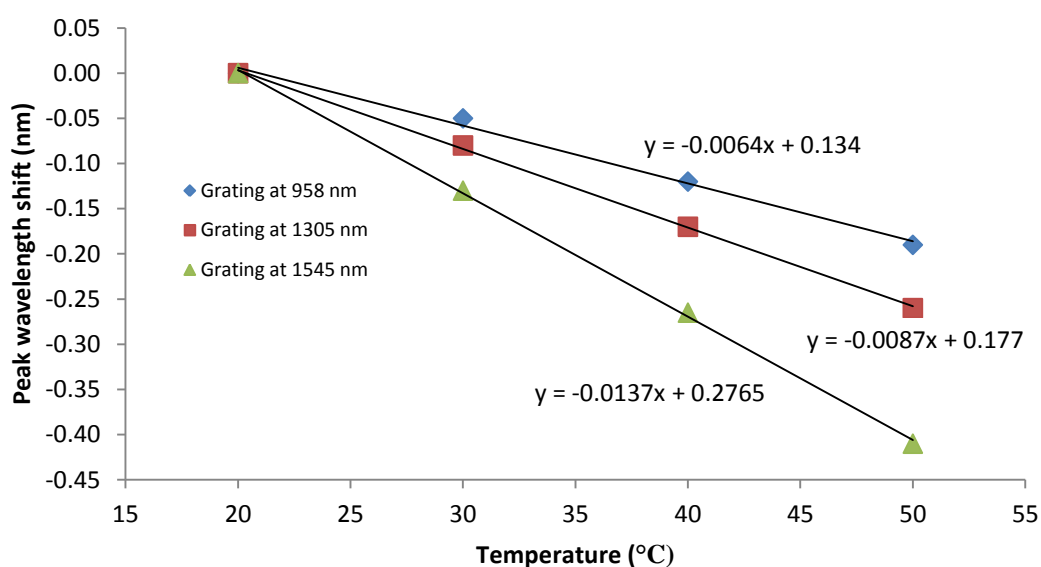
Figure 5.40 Wavelength shift plotted against temperature for three PFBGs at 60 %RH

5.2.10.3. At absolute dry conditions

The relative humidity was constant in all measurements of Figure 5.40, but the measured sensitivity is still moisture-related. To measure the intrinsic temperature sensitivity of PFBGs, the grating should be measured at absolute dry condition. Therefore, the fiber was placed in a sealed test tube that was dried by CaH_2, as shown in Figure 5.41. The sealed test tube was heated in a water bath to control temperature.
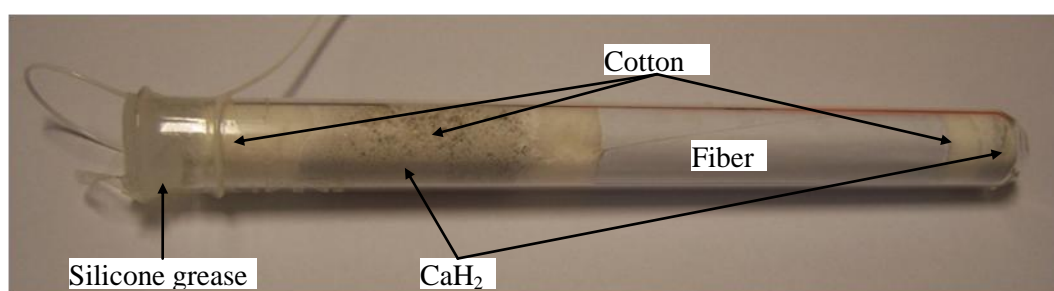
Figure 5.41 Photo of the test tube in which the FBG was placed. Calcium hydride was used to react with moisture, and the tube was sealed at top by sealing grease

The dry condition (0% RH) in the test tube was confirmed experimentally. As shown in Table 5.4, Bragg wavelengths of three gratings in a single fiber in the dried test tube and these in vacuum were the same taking into account of the resolution of the used OSA (0.05 nm, ANDO 6315A). This comparison, however, only suggests that CaH_2 could dry the sealed test tube to 0% RH. To confirm that the PFBG in the dried test tube was immune to the humidity change outside of the tube, the Bragg wavelength of a polymer FBG was monitored while changing the surrounding RH. No noticeable Bragg wavelength shift was observed for the grating inside the tube when the surrounding RH was increased from 20% to 80%. These two experiments assured the dry condition in the test tube when heating the test tube and the fiber inside, so that thermal response of the PFBG was measured at 0 %RH.

Table 5.4 Bragg wavelength of three gratings in vacuum and in the bottle dried by CaH_2

Grating No.	Phase Mask used	Peak wavelength at ambient condition (nm)	Peak wavelength in vacuum (nm)	Peak wavelength in bottle dried by CaH_2 (nm)
G960	PM647	959.88	957.02	956.96
G1304	PM884	1308.035	1304.22	1304.17
G1542	PM1047I	1546.485	1542.03	1541.99

Thermal response of such a PFBG in the dried test tube is shown in Figure 5.42. The grating was heated to 60 ℃ and maintained at this temperature until Bragg wavelength became steady and was recorded. The temperature was decreased to 0.8 ℃ in several steps, and then increased to 60 ℃ continuously within 60 min. After the thermal cycle, the Bragg wavelength almost completely returned. The Bragg wavelength during decreasing temperature was higher than that during heating, and this was caused by the temperature difference between the water bath and the fiber. Because the recorded temperature was that of the water, the temperature of the fiber was higher than that of water during cooling and lower during heating. The total wavelength shift from 0.8 to 60.0 ℃ was only 94 pm. The relationship between the temperature and Bragg wavelength was nonlinear. The higher the temperature, the bigger the wavelength shift per degree was.
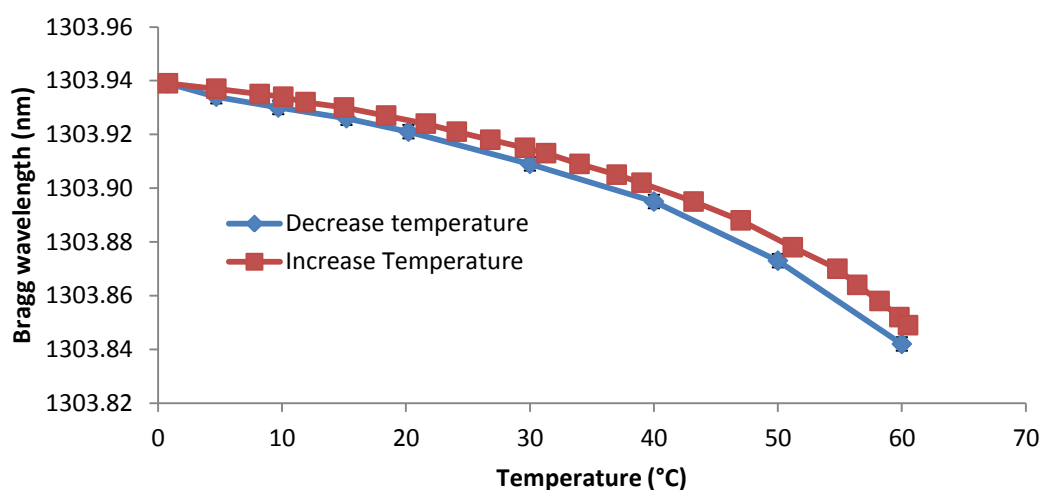
Figure 5.42 Thermal response of a polymer FBG at absolute dry condition

The temperature sensitivity, as shown in Figure 5.43, was calculated by fitting and differentiating the data during cooling in Figure 5.42. The absolute value of temperature sensitivity increases from 0.5 to 4 pm/℃ for temperature range of 0-60 ℃. From 0 to 40 ℃, the sensitivity linearly increases with temperature. Above

40 ℃, the slope of increase becomes steep. The temperature sensitivity at 20 ℃ is -1 pm/℃, which is one order of magnitude lower than that of FBGs in silica fibers (~10 pm/℃). Moreover, this temperature sensitivity at dry condition is almost two orders of magnitude lower than that of values previously reported for Bragg gratings in PMMA based fibers, most of which were measured at ambient conditions.
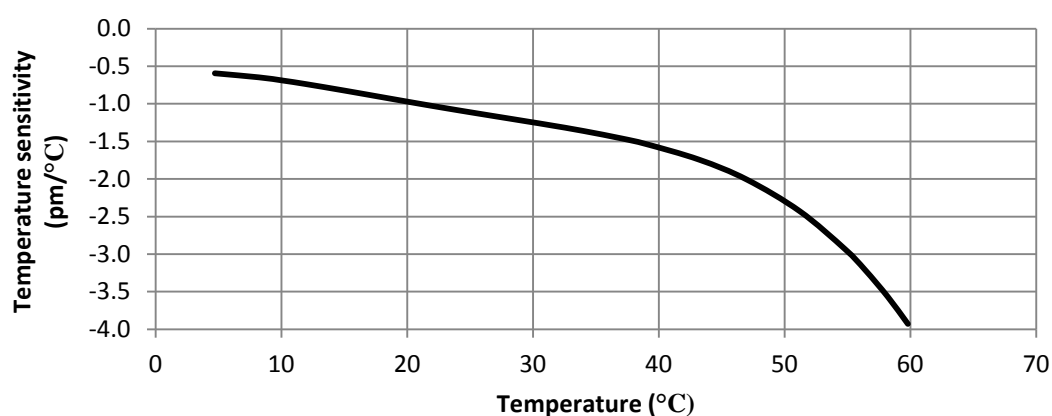
Figure 5.43 Temperature sensitivity of the PFBGs estimated from the data during cooling in Figure 5.42.
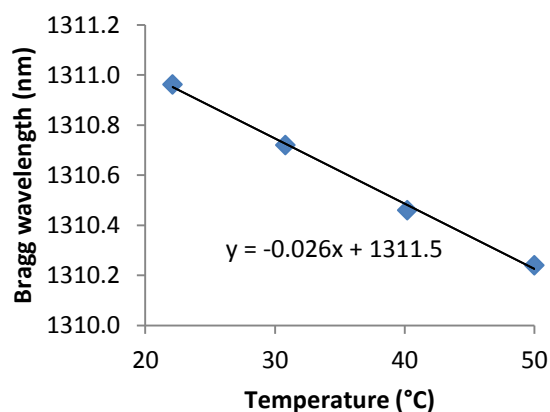
Figure 5.44 Temperature sensitivity of a polymer FBG in water

5.2.10.4. In water

The temperature sensitivity of the PFBGs was also measured in water, and the measured sensitivity was -26 pm/℃ with 20-50 ℃, as shown in Figure 5.44. This value is almost 20 times higher than that at dry condition, and several times higher

than that at 60% RH. The main reason for this high sensitivity in water is that the moisture content in fiber affects both the dimension and effective RI of the fiber core.

5.2.11. **Humidity response of PFBGs**

PMMA is well known for its moisture absorption, thus its impact on the Bragg grating cannot be ignored as in most previous studies. Only a very recent paper reported the influence of relative humidity on gratings in PMMA based optical fibers [103]. The grating peak wavelength shifted 8.1 nm after immersing grating in water from that in dry condition. The present study in earlier period also revealed that the temperature sensitivity of the grating is highly dependent on the surrounding relative humidity. Therefore, the impact of relative humidity on the gratings has been systematically studied, and the combined effect of relative humidity and temperature was examined.

Figure 5.45 shows the grating peak wavelength shift upon humidity change at four temperature levels for 20 ℃ to 50 ℃. The humidity was set to 20 %RH at first for four hours to ensure the grating reaching equilibrium state. It took as long as two hours for the grating stabilizing because the grating was in a quite different environment, especially large humidity difference. Then the relative humidity was gradually increased to 40 %RH within one hour and maintained for another four hour to record wavelength shift, and again to 60 %RH and 80 %RH. When increasing humidity, reflection peak shifted almost simultaneously with the humidity change with about 20 min lag, and remained constant during the ensuing isothermal process. It is evident that humidity has dramatic impact on grating resonance wavelength, and the grating peak shifted larger than 3 nm for all four temperature levels. It can be

noticed that the peak wavelength shifted very little upon temperature from 20 ℃ to 50 ℃.
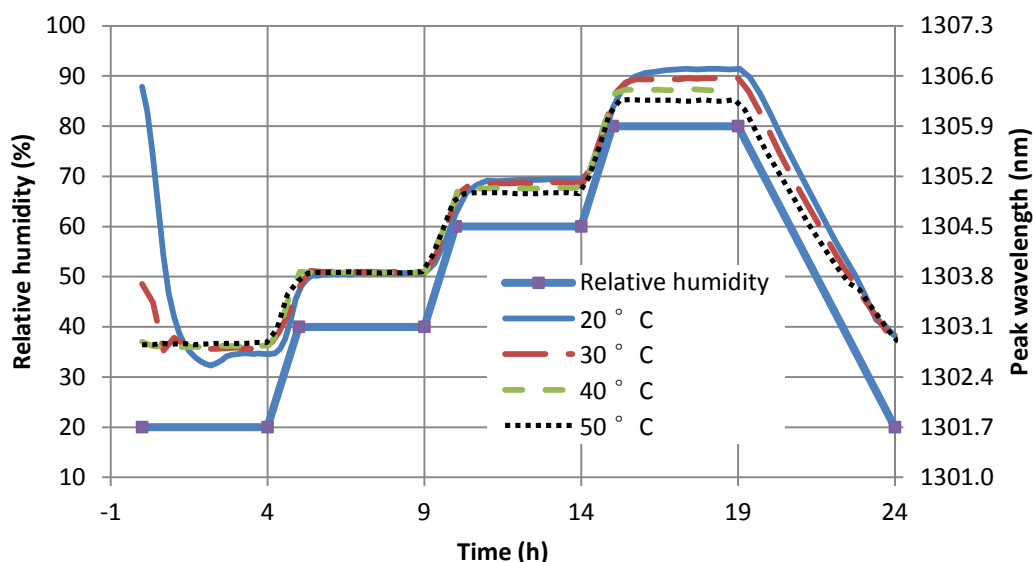
Figure 5.45 peak wavelength shift of the grating as relative humidity was increased and decreased at four temperature levels.

The relationship between peak wavelength on relative humidity and temperature was plotted in Figure 5.46. The slope of peak wavelength shift over relative humidity decreased slightly from 66.1 pm/%RH at 20 ℃ to 56.2 pm/%RH at 50 ℃, and this temperature-dependant variation has been also reported previously [133]. The slope of wavelength shift over humidity linearly decreased as temperature increasing, as shown in Figure 5.46(b).The slope of peak wavelength shift over RH decreased slightly from 6.61 nm at 20 ℃ to 5.62 nm at 50 ℃. That means the grating shifts 6.61 nm from absolute dry condition to completely saturated vapor at 20 ℃, and 5.62 nm at 50 ℃.
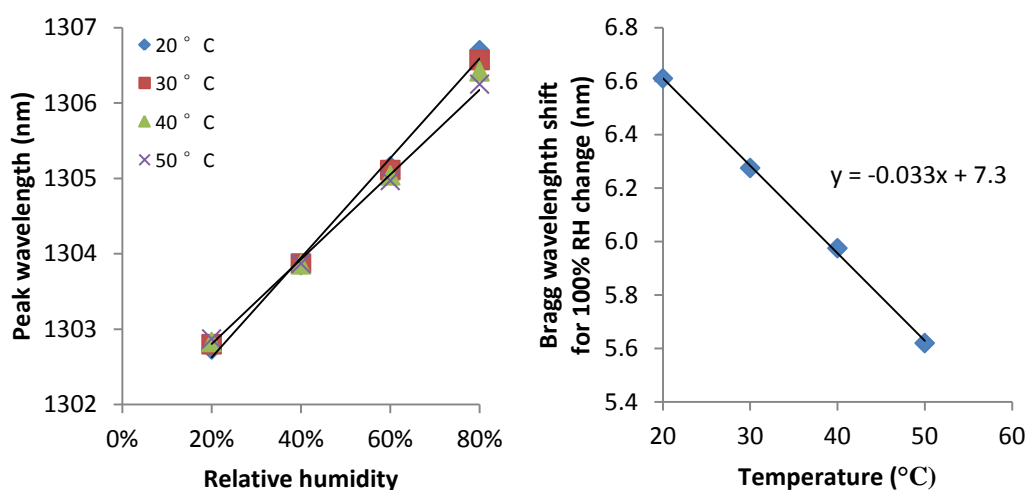
Figure 5.46 Relationship between peak wavelength and relative humidity at four temperature levels (a), and its dependence on temperature

Based on the characteristics of data in Figure 5.46, the resonance wavelength of the grating was fitted to the following equation using the least square method:

$$\lambda = 1301.07 + 7.26H + 0.012T - 0.033H \cdot T \qquad (5\text{-}3)$$

The R square value and standard error of the fitting is 0.9956 and 0.1. Statistical analysis was also adopted to test the dependence of the Bragg wavelength on humidity and temperature, and the result is shown in Table 5.5, suggesting high dependence of the Bragg wavelength on humidity.

Table 5.5 Result of statistical analysis on the the dependence of the Bragg wavelength on humidity and temperature (Data Analysis module of Excel 2007, two-factor without replication ANOVA)

Source of Variation	SS	df	MS	F	P-value	F crit
Humidity	9.748267	2	4.874133	753.732	7E-06	6.944272
Temperature	0.035267	2	0.017633	2.726804	0.17903	6.944272
Error	0.025867	4	0.006467			
Total	9.8094	8				

Its respective derivatives on humidity and temperature are

$$\frac{\partial \lambda}{\partial H} = 7.26 - 0.033\, T \qquad (5\text{-}4)$$

$$\frac{\partial \lambda}{\partial T} = 0.012 - 0.033\, H \qquad (5\text{-}5)$$

Where T is temperature in °C, and H represents relative humidity ranging from 0 to 100%. This relationship is quite different from the situation for silica FBGs. Polymer-coated silica FBGs had a linear additive relation of RH and temperature effects [150]. But for gratings in POFs, the effect of humidity and temperature is correlated, and this phenomenon is the result of humidity-dependent thermal expansion of PMMA [151].

Mathematically, the Bragg wavelength shift can be expressed in the following equation by solving derivative of Bragg law $\lambda = 2n\Lambda$

$$\frac{\partial \lambda}{\partial T} = 2n\frac{\partial \Lambda}{\partial T} + 2\Lambda\frac{\partial n}{\partial T} = \lambda(\alpha_\Lambda + \alpha_n) \qquad (5\text{-}6)$$

$$\frac{\partial \lambda}{\partial H} = 2n\frac{\partial \Lambda}{\partial H} + 2\Lambda\frac{\partial n}{\partial H} = \lambda(\beta_\Lambda + \beta_n) \qquad (5\text{-}7)$$

Where

$\alpha_\Lambda = \frac{1}{\Lambda}\frac{\partial \Lambda}{\partial T}$ is coefficient of thermal expansion in K^{-1}

$\alpha_n = \frac{1}{n}\frac{\partial n}{\partial T}$ is normalized thermo-optic coefficient in K^{-1}

$\beta_\Lambda = \frac{1}{\Lambda}\frac{\partial \Lambda}{\partial H}$ is the coefficient for expansion induced by humidity change

$\beta_n = \frac{1}{n}\frac{\partial n}{\partial H}$ is the coefficient for RI change induced by humidity change

Assuming λ=1301.07nm, the two sets of coefficient can be calculated as follows

$$\alpha_\Lambda + \alpha_n = 0.92 \times 10^{-5} - 2.54 \times 10^{-5}\, H \qquad (5\text{-}8)$$

$$\beta_\Lambda + \beta_n = 55.8 \times 10^{-5} - 2.54 \times 10^{-5}\, T \qquad (5\text{-}9)$$

Based on the above result, it can be estimated that at dry condition (H=0), the sum of α_Λ and α_n would be positive, suggesting that the CTE is larger than the absolute value of the thermo-optic coefficient. We estimate the normalized thermo-optic coefficient α_n of PMMA based on the results in [133], and found it to be 6.7×10^{-5}. It is slightly smaller than thermal expansion coefficient of 7.5×10^{-5}.

The above experimental result reveals that relative humidity has significant impact on the grating resonance wavelength, while the influence of temperature is much smaller. This is a piece of good news and also bad news. In one aspect, polymer optical fiber gratings have large humidity sensitivity, i.e. 66.1 pm/(%RH) for the grating with 1302.73 nm (20 ℃, 20 %RH) at 20 ℃. But the application might be only suitable for those slowly changed humidity environment because the moisture absorption and diffusion is much slow due to the existence of cladding. Removing cladding and exposing fiber core immediately to the environment may solve response time issue, and eventually providing practical humidity sensor. On the other hand, this large shift due to humidity might be a big issue for other sensing applications. One promising application for the polymer optical fiber grating is large strain sensor, where humidity compensation must be considered for real situation.
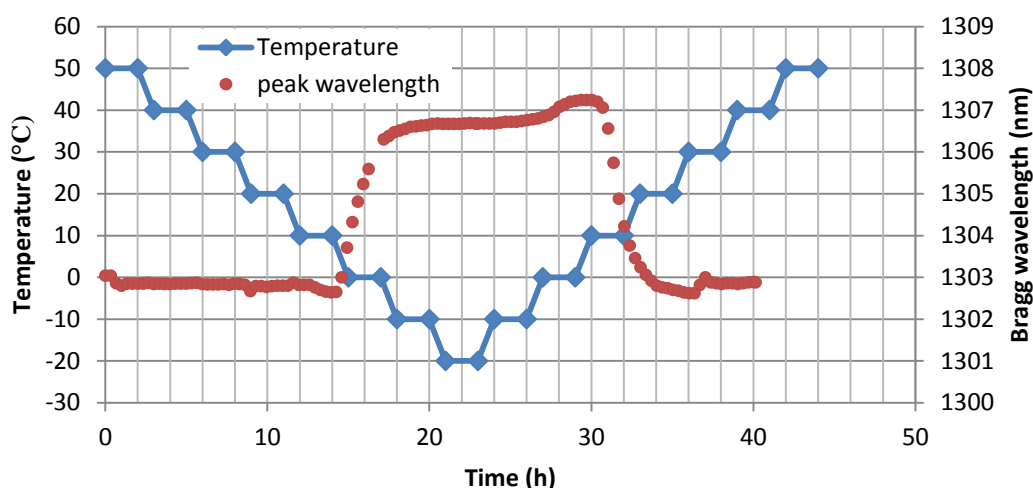
Figure 5.47 thermal response of a PFBG at a constant 20 %RH

Figure 5.47 shows result of PFBG at 20 %RH in the climatic chamber. From 50 °C to 10 °C, the Bragg wavelength shift is minimal. When the temperature was decreased from 10 °C to 0 °C, the Bragg wavelength shifted more than 3 nm towards longer wavelength. The reason for this wavelength jump is due to the RH change in the climatic chamber, because the RH in the chamber can only be controlled within the temperature range of 10-90 °C. In other words, the RH in the chamber below 10 °C is uncontrollable. Therefore, the Bragg wavelength of the fabricated grating at temperature from -20 °C to 10 °C shifted rather than kept steady. After the temperature was increased above 10 °C, the RH in the chamber maintains at 20% again and the Bragg wavelength of the grating kept constant.

Figure 5.48 shows the thermal response of a grating, while temperature was increased from 10 °C to 50 °C, for 2 h at each temperature level in the climate chamber. The chamber automatically increase temperature at end of each step at maximum speed of 3.5~4.0 °C/min. The peak wavelength was recorded per 10 min. The most peculiar character is at each process of temperature increasing, the peak wavelength blue-shifted rapidly within about 20 min, then reversed back completely

below 30 ℃, but only partially at 40 and 50 ℃. The results are much different from the situation with constant relative humidity. If the peak wavelengths after stabilizing was used, the temperature sensitivity was fitted to be 65 pm/℃ with poor linearity (R^2=0.9). But when the shorter wavelengths were used, the sensitivity is 96 pm/℃. Nevertheless, those results are and influenced by the measurement environment.
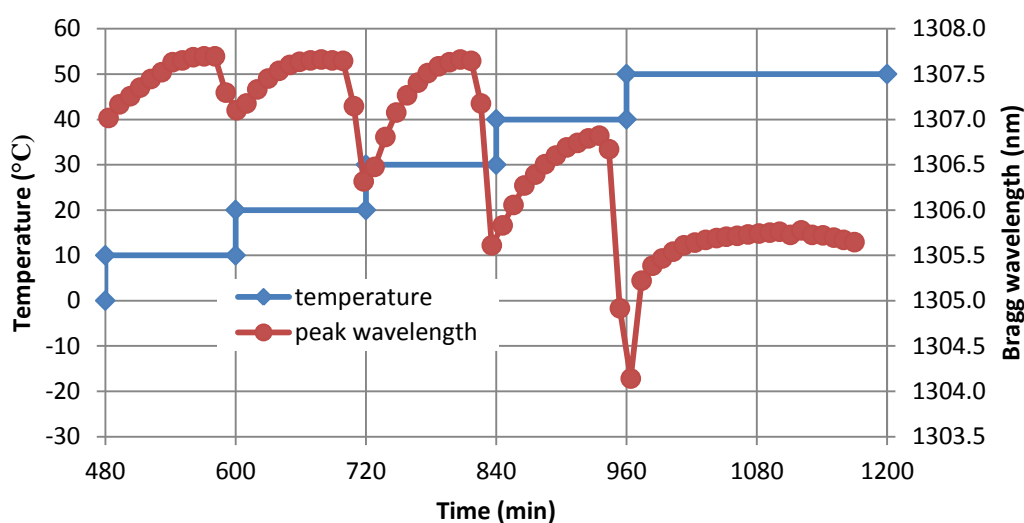
Figure 5.48 Thermal response of the PFBG without controlling relative humidity. (Environment relative humidity is around 60%).

These two examples show that without relative humidity control, the thermal response of PFBGs exhibits different behavior depending on the heating environment and conditions, because the relative humidity of an environment is always influenced by temperature change. This is very reason for the hysteresis of wavelength shift in Figure 5.35 and Figure 5.36. During heating on the Peltier device, the relative humidity surrounding fiber decreased, therefore, grating peak blue-shifted due to moisture desorption. However, absorption and diffusion process was much slow and takes several hours to reach equilibrium state in the fiber core even the temperature was decreased.

5.2.12. **Strain and stress response of PFBGs**

Figure 5.49 and Figure 5.50 show the strain response of two PFBGs written in as-drawn and annealed fiber, respectively. The response was measured by stretching the fiber by 0.5%, keeping for 30 min and then releasing. The strain was increased to 1.0% and so on. The largest strain that could be applied on the fiber was restricted by the bandwidth of the light source. For these two experiments, the light source centered at 970 nm and its upper limit is around 985 nm. Therefore, the as-drawn fiber was stretched to 3.5%, whereas the annealed fiber was stretched to 5.0%. However, the shifts of Bragg wavelength for both experiments were about 20 nm approaching the upper limit of the light source. For both gratings, hysteresis became noticeable when the strain reached 2.0%. For the grating in the annealed fiber, it took more than 3 h to recover to the original wavelength.
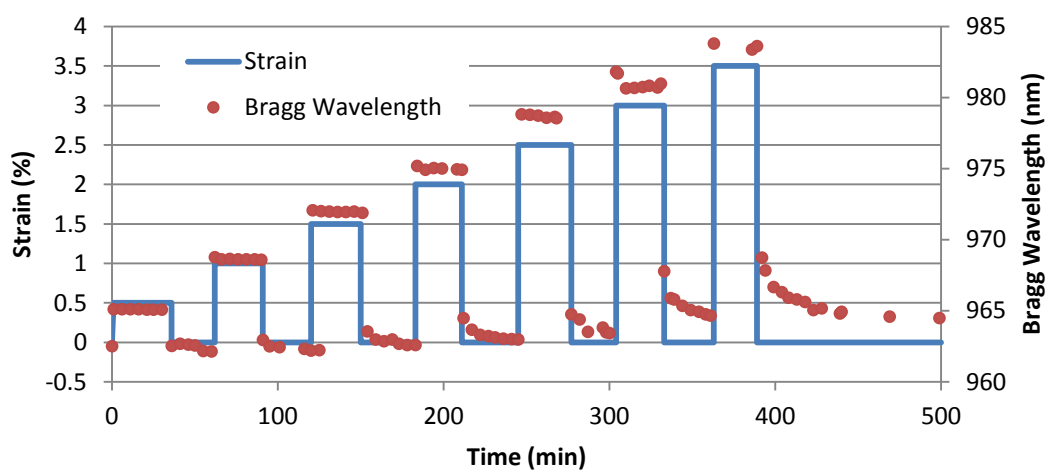
Figure 5.49 Strain response of a polymer FBG written in fiber without annealing
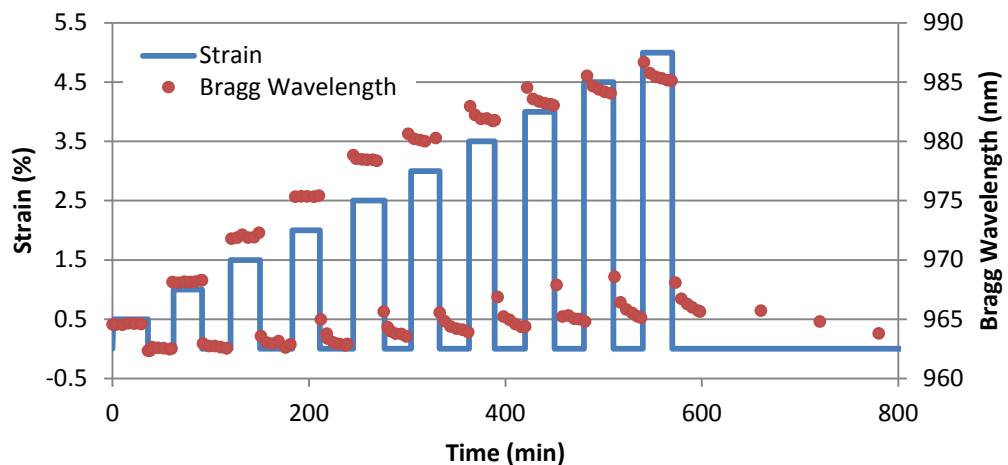
Figure 5.50 Strain response of a polymer FBG written in fiber annealed for 20 times

The relationship between the Bragg wavelength and strain for two gratings is shown in Figure 5.51. For the grating in the as-drawn fiber, the relationship is nearly linear. For the grating in the annealed fiber, the relation is quite linear below 2.5%, but slope decreases above it. Based on data in Figure 5.51, it seems that the gratings in as-drawn fiber and annealed fiber have the same strain sensitivity. But this result is a coincidence, because these two fiber samples are not from the same spool.
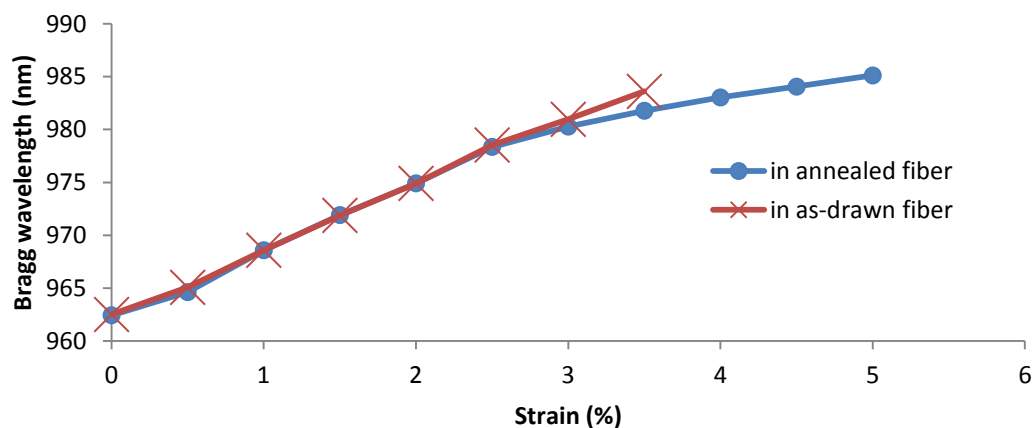
Figure 5.51 Bragg wavelength shift of PFBGs with 962 nm Bragg wavelength written in fiber annealed 20 times

After the fiber fabrication process was improved, the strain and stress sensitivity of PFBGs were measured. The strain and stress sensitivity for three gratings in a single

as-drawn fiber were shown in Figure 5.52 and Figure 5.53. The fiber was only stretched to 1.0% to prevent stress relaxation. Based on the strain sensitivity ($\Delta\lambda/\varepsilon$), the effective strain-optic coefficient P_e can be calculated by converting equation 2-2 to

$$Pe = 1 - \frac{\Delta\lambda}{\varepsilon}\frac{1}{\lambda} \tag{5-10}$$

By combining the strain and stress sensitivity of the grating, the Young's modulus of the fiber can be determined

$$\frac{\Delta\lambda}{\lambda} = (1 - Pe)\varepsilon = (1 - Pe)\frac{\sigma}{E} \tag{5-11}$$

$$E = (1 - Pe)\,\lambda/(\Delta\lambda/\sigma) \tag{5-12}$$

The strain and stress response of the grating after one cycle of annealing is shown in Figure 5.54 and Figure 5.55. The effective strain-optic coefficient and Young's modulus was also calculated. All results are summarized in Table 5.6.
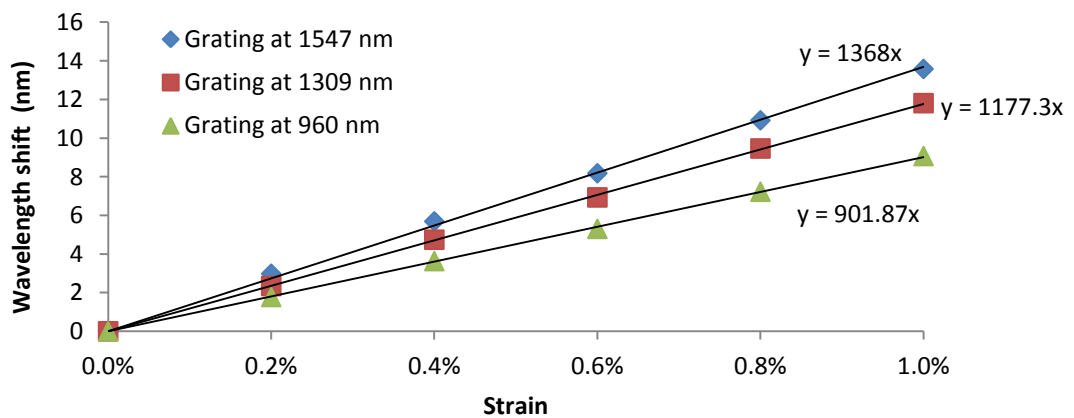
Figure 5.52 The strain response of three gratings at 1547, 1309 and 960 nm in a single fiber without annealing treatment. The strain sensitivity is fitted to be 1.35, 1.18 and 0.91 pm/µε for the three gratings respectively. The effective strain-optic coefficients at three wavelengths are calculated to be 0.13, 0.10 and 0.06.
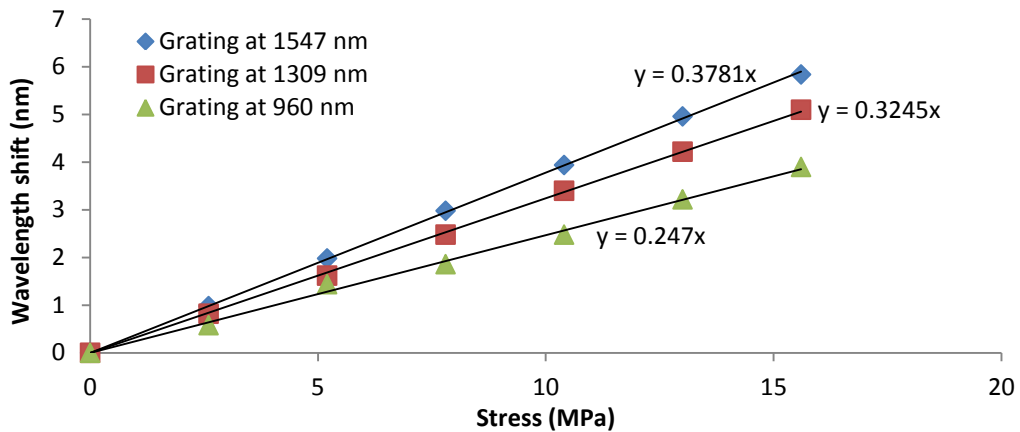
Figure 5.53 The stress response of three gratings at 1547, 1309 and 960 nm in a single fiber without annealing treatment. The stress sensitivity is 0.38, 0.32 and 0.25 nm/MPa for three gratings, respectively.
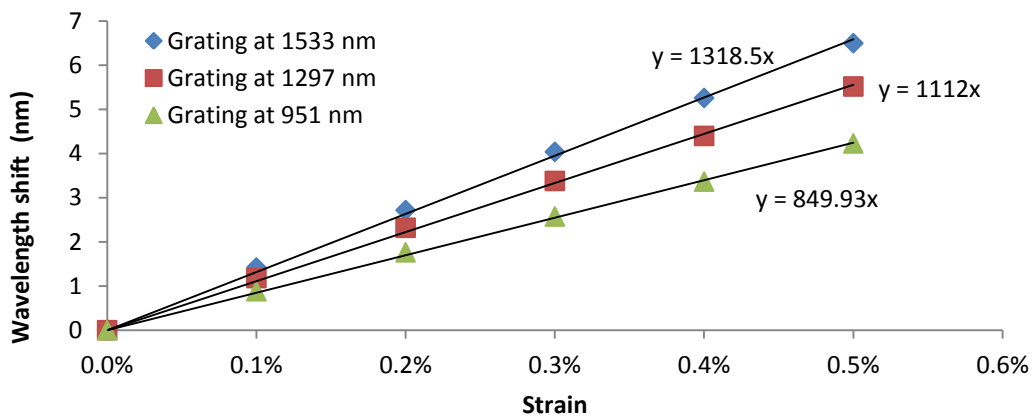
Figure 5.54 The strain response of three gratings at 1533, 1297 and 951 nm, resulted from 1547, 1309, and 960 nm after one cycle of annealing. The strain sensitivity at three wavelengths is 1.32, 1.11 and 0.85 pm/με, respectively.
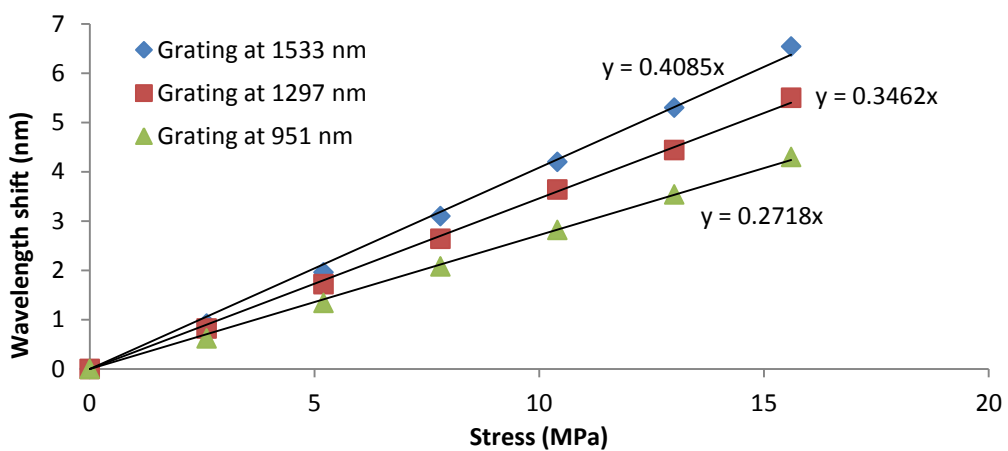
Figure 5.55 The stress response of three gratings three gratings at 1533, 1297 and 951 nm, resulted from 1547, 1309, and 960 nm after one cycle of annealing. The stress sensitivity is 0.41, 0.35 and 0.27 nm/MPa for the three gratings, respectively.

Table 5.6 Strain and stress sensitivity of three gratings before and after annealing

	Grating at 960 nm		Grating at 1309 nm		Grating at 1547 nm	
	Before annealing	After annealing	Before annealing	After annealing	Before annealing	After annealing
Bragg wavelength λ (nm)	960.2	951.3	1308.56	1296.8	1547.3	1533.0
Strain sensitivity $\Delta\lambda/\varepsilon$ (pm/με)	0.91	0.85	1.18	1.11	1.35	1.32
Stress sensitivity $\Delta\lambda/\sigma$ (nm/MPa)	0.25	0.27	0.33	0.35	0.38	0.41
Effective strain-optic coefficient Pe	0.05	0.11	0.10	0.14	0.13	0.14
Young's modulus E (GPa)	3.7	3.1	3.6	3.2	3.6	3.2

The effective strain-optic coefficients p_e at three wavelengths vary substantially. Also, it is increased by annealing treatment, and the magnitude of increase at three wavelengths is different. These results suggest that p_e for POFs is not only different from the homogeneous material, but also dependent on the processing. The results also show that the Young's modulus was decreased by the annealing treatment (3.6 GPa before annealing and 3.2 GPa after annealing).

Figure 5.56 shows the strain response of a FBG with 962 nm central wavelength written in the fiber without annealing when the fiber is continuously stretched. Bragg wavelength almost linearly shifts as the grating is stretched by 6.5%, and the central Bragg wavelength approaches the range limit of the optical spectrum of light source. Though Bragg reflection was too weak to measure beyond 6.5%, the fiber is further stretched, and elongation-at-break of the polymer fiber was measured to be as high as 25%. A single fiber can accommodate many Bragg gratings with a wide range of

central wavelength by combining stretching and annealing process. As shown in Figure 5.57, four PFBGs were inscribed in a single fiber. One of them was inscribed without stretching the fiber, whereas the others were written by stretching the fiber by 0.5%, 1.0% and 1.5%.
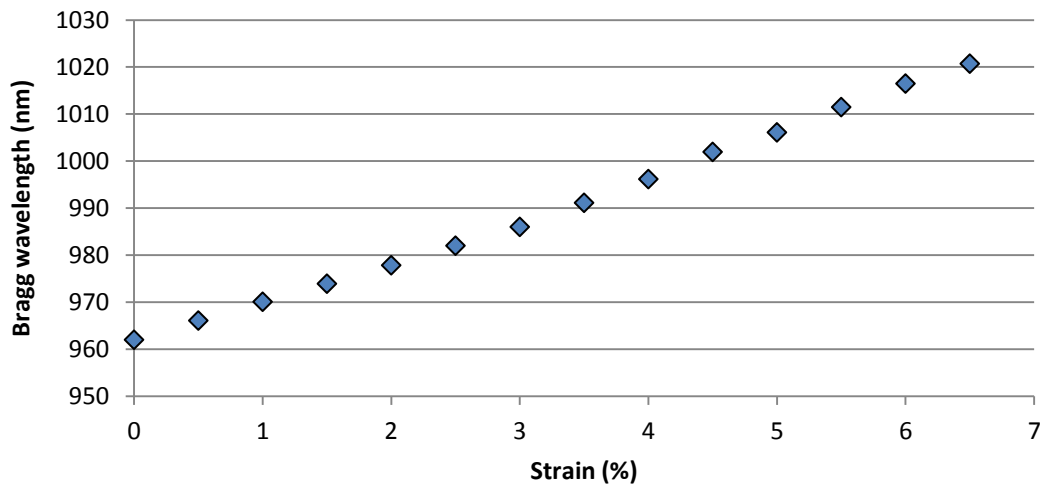
Figure 5.56 Strain response of a PFBG with 962 nm Bragg wavelength written in fiber without annealing
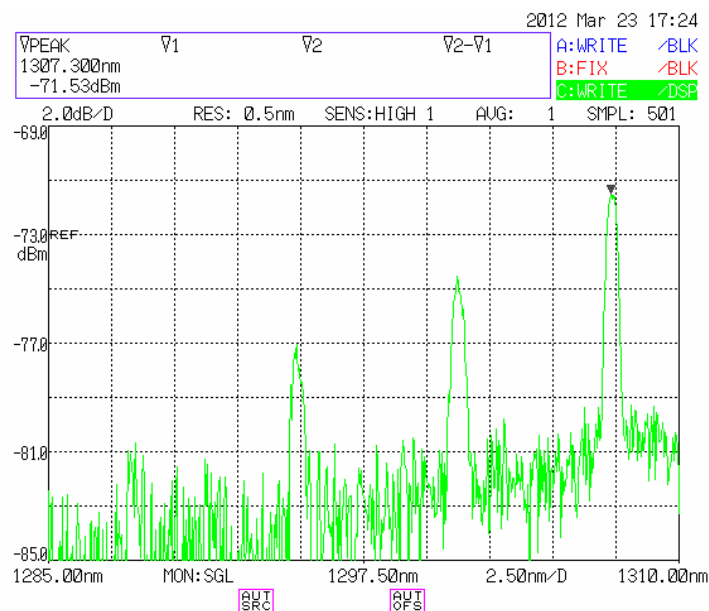
Figure 5.57 Reflection spectra of four PFBGs in a single fiber inscribed by stretching the fiber during inscription. The Bragg peak of 1288 nm grating was weak due to low power output of the used light source at this wavelength

Viscoelasticity of POFs takes effect during measurement of strain response. The above result of sensitivity was obtained by stretching the fiber continuously. Figure 5.49 and Figure 5.50 illustrate that the Bragg wavelength is also dependent upon strain history. For both as-drawn and annealed POFs, Bragg wavelength shift cannot reverse immediately after release when strain larger than 2 %. The recover process took as long as several hours after the fiber was stretched by 3.5 %.

5.2.13. **Response of PFBGs to salt solution**

Since the fabricated PFBGs are sensitive to the moisture content, its response to salt solutions with different salt concentration is explored. A PFBG was immersed in saturated NaCl aqueous solution first. The concentration of saturated solution is 5.4 mol/L (about 26.4%), which was calculated from equilibrium solubility of NaCl in water at room temperature, namely, 359 g/L. After the Bragg peak became steady, the wavelength was recorded. Then the saturated solution was added and mixed with deionized water to reduce the concentration. The grating was immersed and Bragg wavelength was measured. The result is shown in Figure 5.58. As the concentration is decreased, the Bragg peak shifts towards a longer wavelength. The total wavelength shift is about 2 nm from the saturated NaCl solution to pure water, which is equivalent to a sensitivity of 0.37 nm/M. This sensitivity value of PFBG is three times higher than the FBG in silica fiber coated with hydrogels (about 0.11 nm/M) [152], and more than 20 times higher than the FBG in silica fiber coated with polyimide (0.0165 nm/M) [153]. It is of same level with the polyimide-coated polarization-maintaining photonic crystal fiber Sagnac interferometer (0.742 nm/M) [154]. The negative wavelength shift upon increased salt concentration might be due

to desorption of water molecules from fiber, because the affinity between water and sodium chloride must be stronger than that between water and polymer fiber.
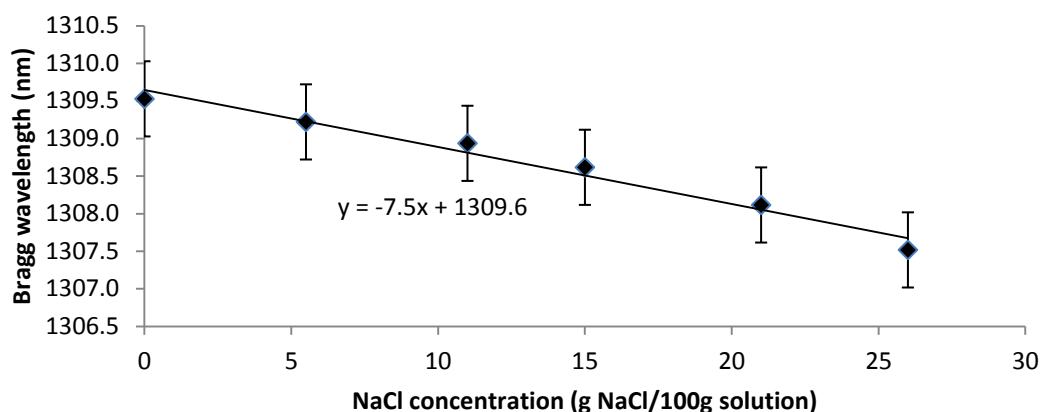
Figure 5.58 Bragg wavelength shift of a grating in NaCl solution at various concentrations

5.3. **Summary**

In this chapter, the formation process of the PFBGs in the PMMA based optical fibers doped with TS has been investigated, and the thermal, humidity and strain responses of the fabricated PFBGs were determined experimentally.

The impacts of properties of phase masks on PFBG inscription were studied experimentally and theoretically. First, PFBGs have been inscribed using phase masks that have a wide range of zeroth order diffractions, from 0.5% to 49%. This contradicts to the previous knowledge that the phase masks for FBG inscription should have <5% zeroth order diffraction. Secondly, the observed microstructure of the PFBGs was found to depend on phase masks, and hence the near-field patterns of phase masks were calculated based on their diffraction ratios. The calculation revealed that the near-field patterns were influenced by not only the zeroth order diffraction, but also the second and third orders. The simulated near-fields agreed with the observed microstructures of the fabricated PFBGs to a large extent.

128

Two distinctive stages were identified during the prolonged phase masked UV exposure to PMMA based POFs doped with TS. The Bragg peak appeared immediately as the UV exposure started, and reached the highest level after several minutes. Then the peak dropped slightly, and started to increases about 20 min after the UV exposure and reached the second highest value within another 20 min. Finally, the Bragg peak decreased slowly and vanished. The fiber was found to be severely damaged after long time exposure, and hence the PFBGs were inscribed by short-time exposure (e.g. 5 min).

After inscription, the PFBGs exhibit a fading and recovery or relaxation process. By heating PFBGs immediately after UV exposure, the completion time for the relaxation process was effectively reduced. Among several proposed hypotheses, the most probable reason for the relaxation process was ascribed to the residual stress relaxation of fiber core induced by TS photoisomerization.

Thermal and humidity effects on PFBGs were studied by experiments. It was found that the relative humidity had a tremendous impact on the PFBGs in PMMA based fibers. For example, the measured humidity sensitivity of a PFBG of 1303 nm was 66 pm/%RH at 20 ℃. The measured temperature sensitivity of the same PFBG at dry condition and at 60 %RH was only 1-3 and 8.7 pm/℃, respectively. They are almost two orders of magnitude lower than most values reported in literature. Moreover, the humidity and temperature were found to have a synergetic effect; that is, the temperature sensitivity was humidity-dependent and vice versa.

The effects of annealing on the POFs and PFBGs were examined. After a complete annealing treatment of 20 cycles, the Bragg wavelength shifted towards shorter

wavelength by as large as 35 nm for a grating of 960 nm. The effective strain-optic coefficient was increased by annealing, and magnitudes of increment at various wavelengths were found to be different.

Lastly, the fabricated PFBGs were found to be highly sensitive to salinity. The measured sensitivity of a 1308 nm PFBG to salinity was 0.37 nm/M, which is three times higher than silica FBGs coated with hydrogels, and more than 20 times higher than silica FBGs coated with polyimide, and on the same level with the polyimide-coated polarization-maintaining photonic crystal fiber Sagnac interferometer.

CHAPTER 6 SHEAR STRESS & PRESSURE SENSOR BASED ON POLYMER FIBER BRAGG GRATING

This chapter is about a practical application of the fabricated PFBGs. Two PFBGs were embedded in a cube of silicone elastomer to simultaneously measure the shear and normal stress (or strain) applied on the cube. In addition to the experimental study, finite element model (FEM) was developed to analyze the sensor and optimize the sensor design.

6.1. Application Background

Precision measurement of shear stress as well as pressure is of profound interest for health monitoring of diabetic foot [155-158] and tactile sensing of prosthetic skin and robotic hands [159-165]. Shear stress under the sole of foot, as well as pressure distribution, plays a major role in diabetic ulceration, and information of shear stress under foot is crucial for the prediction and prevention of ulceration [156, 166]. Even for health foot, plantar shear stress is an important factor for foot problems resulted from wearing high-heel shoes [167]. Robot hands and limb prosthesis need shear sensing to grasp and manipulate objects. Hence, shear stress sensing is being widely studied by researchers from various fields for respective purposes [168].

Compared to the numerous commercial systems and experimental techniques available for plantar pressure measurement, most shear force or stress measurement are done in research laboratories currently, and only a few commercial products are available. There are two main types of sensors used in research laboratories for shear

stress sensing, namely, electrical and optical ones. Electrical ones convert shear deformation into electrical signal while optical ones measure properties change of light, such as intensity and wavelength et al. The electrical type can be further divided into strain gauge [159, 161], piezoelectric [169, 170], capacitive [163, 164], impedance [162], piezoresistive [171-173], magneto resistive ones [174] according to transduction principle. They are generally made by micro-electro-mechanical systems fabrication techniques. Main drawbacks of electrical sensors are wiring complexity and cross-talk between sensors, and their vulnerability to external electromagnetic fields. To address these issues, optical sensors are being studied for shear stress measurement.

Most recently, coupling of optical power between a vertical-cavity surface-emitting laser (VCSEL) and a photodiode facing each other and separated by a deformable transducer layer was exploited to measure shear force [165]. Sensors based on optical fiber bending loss were also reported [175]. These two examples are based on light intensity modulation. Detecting optical power, however, limits the sensing precision because light power fluctuates with electrical source. Moreover, the direction of force or stress is difficult to determine by light intensity modulated sensors.

FBGs are promising for shear stress measurement due to its small size, high sensitivity and distributed sensing capability. Tjin and et al have shown that silica FBGs can be used for measurement of three-component force [176, 177]. They measured pressure by embedding a silica FBG in a layer of a carbon composite block because the FBG that was embedded below the neutral layer was stretched under pressure (The pressure was actually the point load divided by the area of the layer, rather than the real pressure evenly distributed on the composite layer). Two other

FBGs were embedded non-rectilinearly (with a certain angle to the horizontal plane) in the deformable layer sandwiched between two layers of carbon composite material. The axes of two fibers were perpendicular so that they could measure the longitudinal and transverse shear force respectively. The fabricated sensor could measure the magnitude as well as the direction of the applied force in 3D space. The sensitivity of this sensor to normal and shear force was about 30 and 300 pm/N, respectively. However, this sensor could measure only the point load, otherwise the FBG to measure pressure would not work. And also, response of the three FBGs in this sensor to applied force was not linear even within 0-20 N, especially for the pressure and longitudinal shear force measurement.

6.2. **Experimental**

6.2.1. **Polymer fiber Bragg gratings**

The used PFBGs were written in a POF that has PMMA core doped with 0.7 wt % TS core and poly(MMA/TFEME 95/5 mol/mol) cladding. The diameter of fiber core and cladding was about 12 and 130 μm, respectively. PFBGs were inscribed by phase masked exposure of UV laser described in Chapter 5. Each grating was 5 mm in length by scanning a laser beam along the fiber length with a speed of 5 μm/s, and the accumulated exposure time for each position was 5 min. The central wavelength of gratings was around 1310 nm.

6.2.2. **Sensor fabrication**

Figure 6.1 shows structure of the pressure and shear stress sensor. Two gratings are used to measure shear stress and pressure indirectly based on the geometry change of

the silicone cube subject to external normal and shear force. To discriminate pressure and shear force, one grating is horizontally embedded while the other one is tilted.

The sensor cube was cast from silicone in a cubic container. Two opposite sides of the container were acrylic transparent tape so that after silicone curing, they could be cut off for easy mold removal. A release agent (Vaseline) was applied on the inner surface of mold to facilitate easy separation of the mold and the sensor cube. Two couples of holes on two plastic sides were cut to fix two fibers. The release agent was also applied on the surface of fibers for aforementioned reasons. Mixture of SILASTIC 3483 base (Dow Corning) and curing agent was vacuumed to remove any air bubble formed during mixing, and then poured into the mold. Silicone was cured and hardened at room temperature within one day. The test of sensor was conducted at least seven days to ensure complete curing. After removal of mold, four gaskets were adhered to fiber using UV adhesive (NORLAND 65). Figure 6.2 shows the photo of the fabricated sensor.
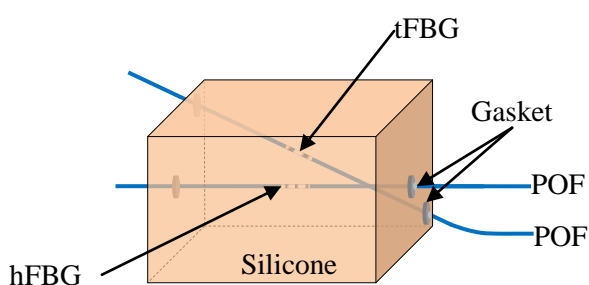
Figure 6.1 Structure of the sensor for the measurement of shear and pressure stresses. One grating, hFBG, is horizontally placed through the center, whereas the other one is tilted and denoted as tFBG.
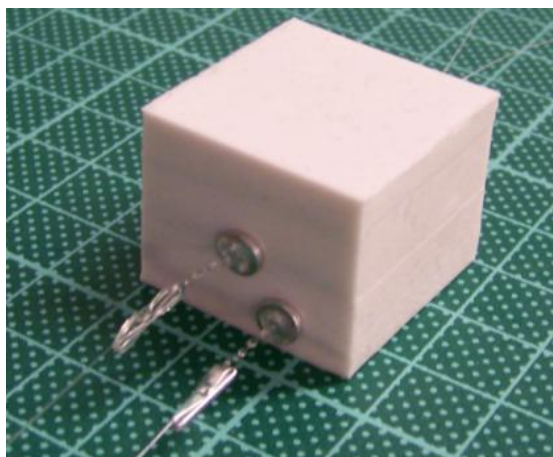
Figure 6.2 Photo of the fabricated sensor on a plastic mat. The sensor is 27 mm in length and in width, and 22 mm in height.

Preliminary study found that if the fiber was bonded to the silicone, the reflection spectrum of grating deformed dramatically under large strain due to uneven strain distribution with the silicone and along fiber axis [178]. To address this problem, release agent was applied on the surface of fiber during embedding process so that no mechanical bonding between the elastomer and two fibers. To induce strain on fiber grating, four gaskets with holes slightly larger than fiber were adhered to fiber at surface of the silicone cube.

6.2.3. **Sensor test**

To simulate different application situations, the sensor was tested using two experimental schemes: (1) applying displacement as shown in Figure 6.3 and (2) applying stress as shown in Figure 6.4. The sensor was free to rotate in the Figure 6.4 upon shear force but it was restricted in Figure 6.3. The peak wavelength shift of tFBG and hFBG under loading was monitored by the optical spectrum analyzer (ANDO 6315A).
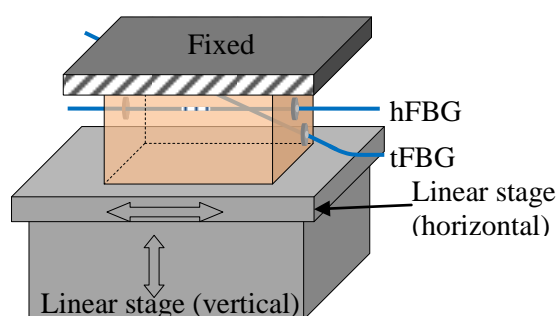
Figure 6.3 Experimental setup to test the sensor by simultaneously applying normal and horizontal displacements. Normal and horizontal displacements are applied on the bottom of the cube by use of two linear stages, while the top face is fixed.
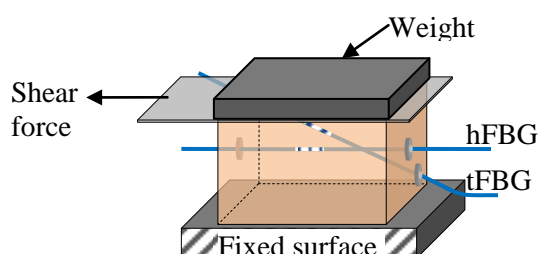
Figure 6.4 Experimental setup to test the sensor by simultaneously applying pressure and shear stress. A glass side is placed on top of the cube, on which a weight is added to apply pressure on the sensor. The glass slide is drawn laterally to impose shear stress.

The deformation of the silicone cube under to loading schemes is illustrated in Figure 6.5. Under displacement loading, the normal and shear strains were calculated by

$$\epsilon_n = \frac{\Delta y}{y} \tag{6-1}$$

$$\epsilon_s = \beta = \text{atan}\left(\frac{\Delta x}{y - \Delta y}\right) \approx \frac{\Delta x}{y} \tag{6-2}$$

Where Δx and Δy are normal and shear displacements, respectively; y is the height of the cube. The shear strain is simplified to $\Delta x/y$ for small deformation without considering the height change of the sensor upon normal displacement, resulting in an error of 5% in the calculated ϵ_s.

Under force loading, the normal and shear stresses were calculated by

$$\sigma_n = \frac{F_n}{A} \tag{6-3}$$

$$\sigma_s = \frac{F_s}{A} \tag{6-4}$$

Where F_n and F_s are vertical (normal) and horizontal (shear) forces, respectively; A is the area of the top surface of the cube, on which forces were applied.

(a) Applying displacement

(b) Applying force
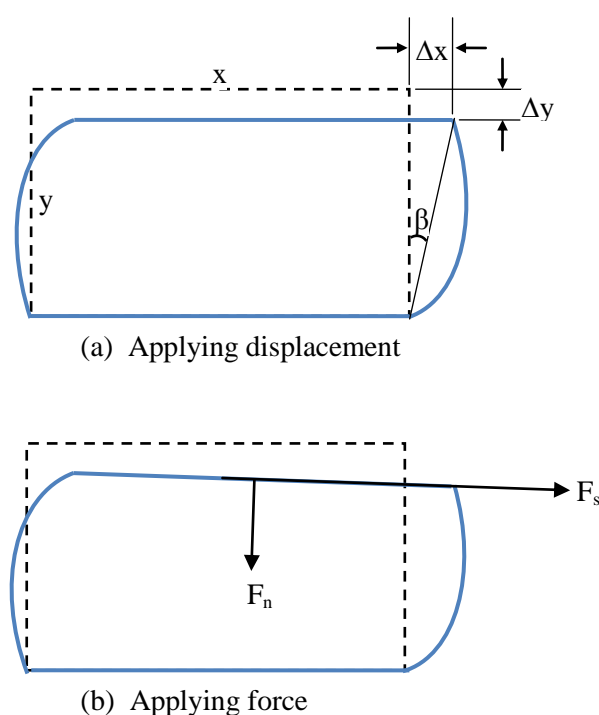
Figure 6.5 Schematic deformation of the silicone cube under (a) displacement loading and (b) force loading

6.3. **Finite Element Analysis of the Sensor**

Finite element analysis (FEA) was conducted (by Dr. Zhang Hua-Peng) in parallel with experiment for sensor design. The structural mechanics module of ANSYS 13.0, a commercial FEA package, was used to build and simulate the sensor model. Major specifications of the finite element model are listed in Table 6.1. Two cases of sensor

design were studied. First, the sensor without the four gaskets was simulated, and surfaces of two optical fibers and silicone matrix were assumed to be perfectly bonded together, so that strain was induced along fiber due to silicone deformation under loading. Secondly, a sensor with four gaskets was simulated with a friction-free interface between the fibers and matrix. The axial fiber strain was induced by relative movements of two gaskets, which were determined by the displacement of the cube. Vertical or horizontal displacements were added to the bottom face of the cube in the same manner as experimental scheme in Figure 6.3.

Table 6.1 Specifications of the finite element model

Geometry	The sensor cube 27mm × 27 mm × 22mm(height); The fiber 130 μm in diameter; The gasket 5 mm in diameter
	The fiber with hFBG was placed horizontally through the center of two side faces. The fiber with tFBG was embedded in the vertical plane (5 mm to vertical symmetry plane) with an angle of 27 º to the horizontal plane
Material (All material assumed to be linear elastic)	Fiber modulus 2GPa, Poisson's ratio 0.3 Silicone modulus 0.1 MPa, Poisson's ratio 0.48 Steel gasket modulus 200GPa, Poisson's ratio 0.29
Boundary & Contact conditions	The contacts of optical fibers with the steel gaskets were always bonded; contacts of optical fibers with the silicone cube were modeled as standard sliding contact with a friction coefficient of 0.2 (measured)

6.4. **Results and Discussion**

Figure 6.6 shows the strain distributions of two cases along fiber axis obtained by finite element analysis for the above-mentioned two cases. In case 1, fibers are bonded to silicone matrix, and both fibers exhibit non-uniform axial strain. The strain increases from zero at two ends to highest at the center. Though the gratings are only 5 mm in length, the impact of uneven axial strain on the reflection properties of two gratings is significant. Also, uneven axial strain imposes serious restriction on precise placement of gratings at center of the sensor, or the strain along fiber axis is

not only uneven, but also asymmetric. Asymmetric strain might affect the sensor performance more adversely than unevenness. In case 2, by free slippage between fibers and silicone matrix and using four gaskets to stretch fiber from two ends, the strain along both fibers becomes uniform, in addition, the induced strain increased by 2.0 times for hFBG and 2.2 times for tFBG, making the sensor more sensitive. The increase in sensitivity can be clearly illuminated by the deformation of two sensor models under loading, as shown in Figure 6.6.
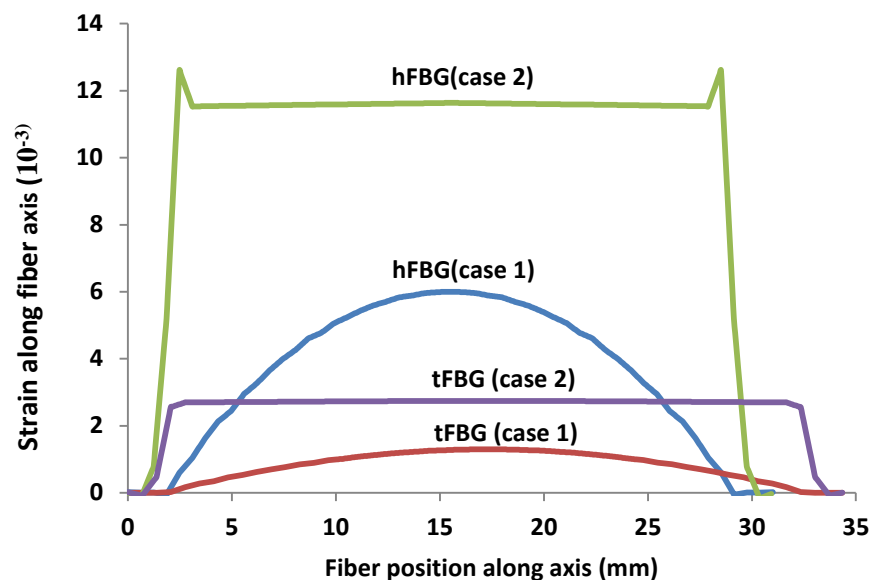
Figure 6.6 Simulated strain along fiber axis for hFBG and tFBG when the sensor was applied 5% normal strain in case (1): the fiber and matrix is bonded perfectly and deformation of the matrix material induced strain on fiber axis; and case (2): no bonding between fibers and silicone matrix, and two gaskets are adhered to each fiber end at the sensor surface to stretch fiber under loading.

The improved sensitivity by using the gaskets to stretch fibers is illustrated by Figure 6.7. Without the gasket, the fiber is stretched by the surrounding silicone. Due to large difference in Young's modulus (2.1 GPa for fiber; 0.1 MPa for silicone), deformation of the silicone surrounding the fiber is restricted by the fiber. By using gaskets to stretch the fiber, more volume of silicone takes part into deformation to

stretch fiber. The fiber is stretched by two gaskets at two ends, so that the strain along the fiber is uniform. In addition, the fiber is not bonded to the silicone elastomer, and hence there is no stress concentration effect.

<div align="center">(a) Case 1   (b) Case 2</div>
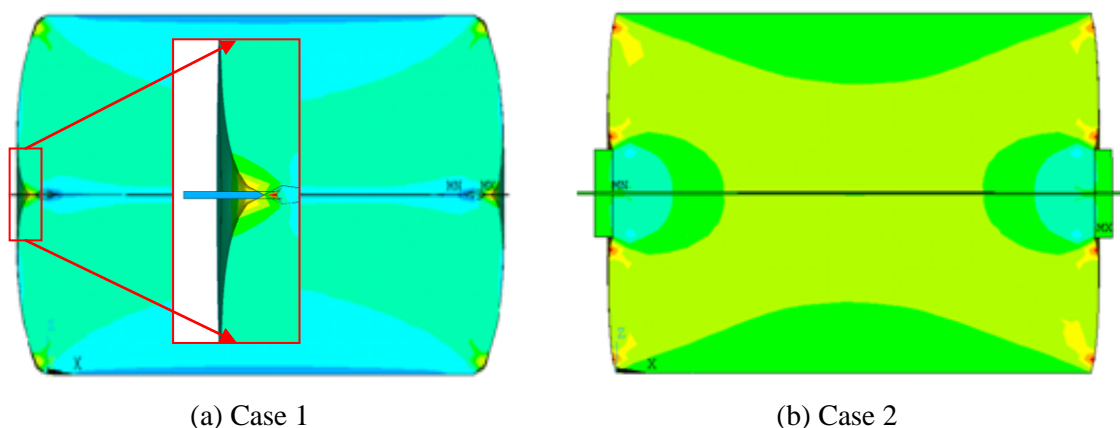
Figure 6.7 Strain distributions of the fiber and the cross section of the sensor simulated by FEM

During sensor fabrication, a release agent was applied on fiber surface to make frictionless interface between the fiber surface and silicone matrix. In order to confirm the frictionless interface, the sensor was applied pressure before sticking the gaskets to fibers, and the Bragg wavelength of hFBG was monitored. As shown in Figure 6.8, the Bragg wavelength of hFBG did not change upon loading, suggesting no strain on fiber, and hence no friction between silicone matrix and the fiber. Figure 6.8 also shows the Bragg wavelength of the hFBG upon loading after the gaskets were adhered to the fiber. The Bragg peak positively shifted because the fiber was stretched by two gaskets from two ends.
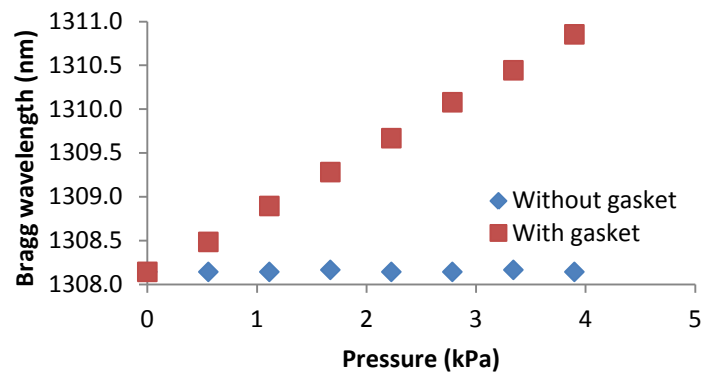
Figure 6.8 Pressure response of a single grating embedded in silicone cube while silicone oil applied on the surface of fiber during embedding process
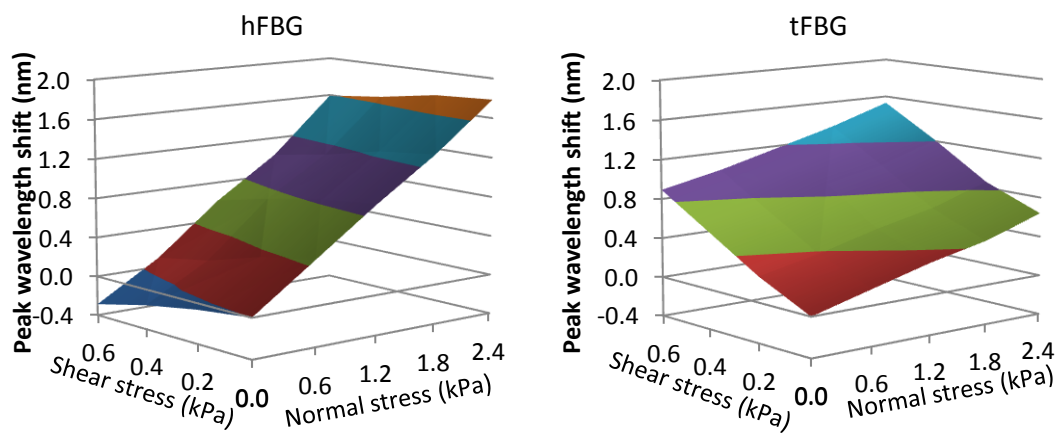
Figure 6.9 Measured Bragg wavelength shift of hFBG and tFBG when pressure and shear force applied (experimental scheme of Figure 6.4)
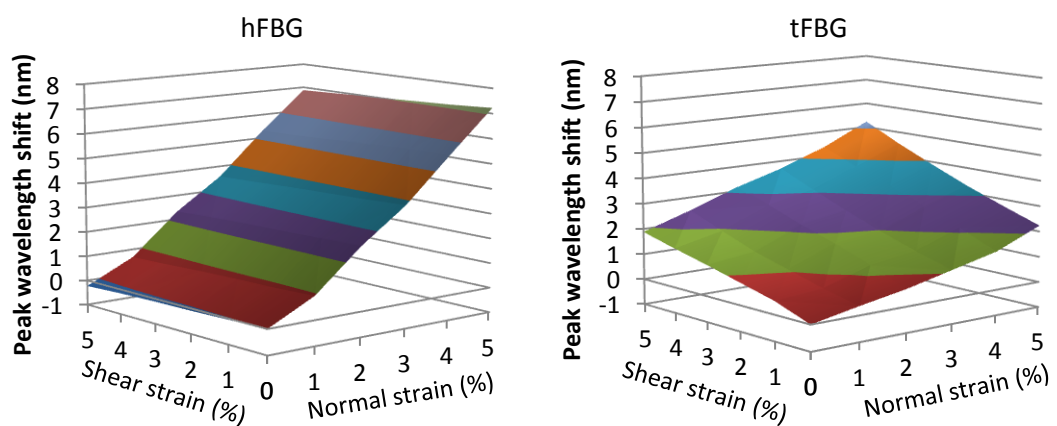
Figure 6.10 Measured Bragg wavelength shift of hFBG and tFBG when normal and shear displacement applied (experimental scheme of Figure 6.3)

141

Figure 6.9 and Figure 6.10 show the measured Bragg wavelength shift of hFBG and tFBG when experimentally applying force and displacement on the fabricated sensor, respectively. The horizontal grating (hFBG) shifts towards longer wavelength upon normal stress but shear loading results in negative shift. For tFBG, both normal and shear loading lead to positive peak wavelength shift. The trends of major responses of two gratings agree with the finite element analysis, despite the fact that there is apparent discrepancy quantitatively, as demonstrated in Figure 6.11. The discrepancy between experimental and simulation results might come from several oversimplified assumptions in finite element model, like perfect adhesion between fiber and gasket, rigid body treatment of the used adhesive and et al.
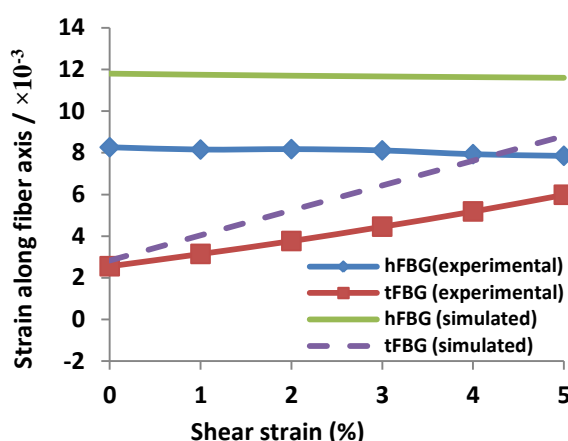
Figure 6.11 Comparison of experimental and simulated strain along fiber axis with constant normal strain of 5% and shear strain ranging from 0 to 5%. Raising shear strain leads to larger strain on tFBG and slightly smaller strain on hFBG. Experiment and simulation exhibit the same trend while the simulated strain is larger than the experimental value.

To quantitatively express the responses of two gratings under loading, the data in Figure 6.9 and Figure 6.10 is linearly fitted using the least square method. The peak wavelength shift of hFBG and tFBG under applied displacement are fitted to be:

$$\Delta\lambda_{hFBG} = 140.8\ \varepsilon_n - 9.7\ \varepsilon_s\ (\text{R}^2\ 0.9966) \qquad (6\text{-}5)$$

$$\Delta\lambda_{tFBG} = 47.0\ \varepsilon_n + 43.7\varepsilon_s\ (\text{R}^2\ 0.9911) \qquad (6\text{-}6)$$

Where $\Delta\lambda_{hFBG}$ and $\Delta\lambda_{tFBG}$ are Bragg wavelength shifts of hFBG and tFBG in nanometer, respectively; ε_n and ε_s are the applied normal and shear strain on silicone cube, respectively.

When force applied, the peak wavelengths shift according to the following two equations:

$$\Delta\lambda_{hFBG} = 0.82\ \sigma_n - 0.45\ \sigma_s\ (\text{R}^2\ 0.9985) \qquad (6\text{-}7)$$
$$\Delta\lambda_{tFBG} = 0.30\ \sigma_n + 1.33\ \sigma_s\ (\text{R}^2\ 0.9984) \qquad (6\text{-}8)$$

Where σ_n and σ_s are the applied normal and shear stress on silicone cube in kilopascal, respectively.

In matrix manner, equation 6-7 and 6-8 can be expressed as

$$\begin{bmatrix} \Delta\lambda_{hFBG} \\ \Delta\lambda_{tFBG} \end{bmatrix} = \begin{bmatrix} 0.82 & -0.45 \\ 0.30 & 1.33 \end{bmatrix} \begin{bmatrix} \sigma_n \\ \sigma_s \end{bmatrix} \qquad (6\text{-}9)$$

This equation means the sensitivity of hFBG to normal stress is 0.82 nm/kPa, while the sensitivity of tFBG to shear stress is 1.33 nm/kPa. In other words, using optical spectrum analyzer or FBG interrogator with 1 pm resolution, pressure as low as 1.2 Pa, or shear stress of 0.8 Pa can be detected by this sensor. As for force, the sensitivity to normal and shear force is 1.12 nm/N and 1.80 nm/N, respectively. They are 37 and 6 times higher than those sensors using silica FBGs [177]. From point view of sensing applications, σ_n and σ_s can be calculated by converting the above equation after peak wavelength shift are measured

$$\begin{bmatrix} \sigma_n \\ \sigma_s \end{bmatrix} = \begin{bmatrix} 0.82 & -0.45 \\ 0.30 & 1.33 \end{bmatrix}^{-1} \begin{bmatrix} \Delta\lambda_{hFBG} \\ \Delta\lambda_{tFBG} \end{bmatrix} = \begin{bmatrix} 1.09 & 0.37 \\ -0.24 & 0.67 \end{bmatrix} \begin{bmatrix} \Delta\lambda_{hFBG} \\ \Delta\lambda_{tFBG} \end{bmatrix} \qquad (6\text{-}10)$$

The same conversion can be applied on 6-1 and 6-2 to resolve normal and shear strain

$$\begin{bmatrix} \varepsilon_n \\ \varepsilon_s \end{bmatrix} = \begin{bmatrix} 6.6 & 1.5 \\ -7.1 & 21.3 \end{bmatrix} \begin{bmatrix} \Delta\lambda_{hFBG} \\ \Delta\lambda_{tFBG} \end{bmatrix} \times 10^{-3} \qquad (6\text{-}11)$$

Equation 6-9 and 6-11 are not equivalent since different experimental schemes are used. In most applications, especially like shear stress monitoring under soles, the sensor is free to rotate, and equation 5 should be used to calculate stress. But in cases like structure health monitoring, where there might be relative displacement between structures similar to the scheme of applying displacement, equation 6 should be utilized to resolve strain first, then convert to stress through modulus.

The largest normal and shear strain applied on the sensor reach 5%, but the responses of two gratings exhibit good linearity since the induced strain on fiber grating is still within elastic range of fiber. The largest strain along fiber axis is 0.8% under displacement loading of 5% normal strain and 5% shear strain. It is well below elastic limit of the used fiber, which was measured to be around 2%. Another reason for good linearity is the free interface between two fibers and the elastomer matrix, which avoids uneven strain distribution along the gratings.

6.5. **Summary**

In this chapter, shear and pressure sensors based on the fabricated PFBGs were experimentally studied, and also by finite element analysis. Two PFBGs were embedded in a silicone cube, which was 27 mm in length and width, and 22 mm in width. One of them was horizontally placed whereas the other one was tilted through the cube. Two cases to induce strain on fiber were studied by finite element analysis:

(1) strain was induced by bonding between silicone matrix and fiber surface; (2) strain was induced on fiber by the two gaskets that was adhered to two fiber ends at surface of the cube, while the interface between silicone matrix and fiber surface was frictionless. Simulation results revealed that the strain along fiber length in the second case was uniform when pressure was applied on the sensor, and the produced strain was two times higher than the first case. Hence, the sensor using four gaskets was fabricated.

Performance of the fabricated sensor was tested using two experimental schemes: (1) applying normal and shear forces on the sensor; (2) applying normal and shear displacements on sensor. Both hFBG and tFBG positively shifted except that hFBG slightly negatively shifted upon shear loading. By combining responses of two gratings, normal and shear stress (or strain) could be determined. As for the scheme of applying forces, the sensitivity of the sensor to normal and shear stress were 0.82 and 1.33 nm/kPa.

CHAPTER 7 CONCLUSIONS AND FUTURE WORKS

7.1. **Conclusions**

Photosensitive step-index PMMA-based single-mode POFs with high quality were fabricated. The formation process of Bragg grating in the fabricated POFs was systematically studied. The thermal, humidity, strain responses of the resultant PFBGs were characterized. Major findings and conclusions are summarized as follows:

1. Refractive index modulation of TS doped film by UV irradiation, formation of volume grating in TS doped polymer film, and formation of FBBGs in TS doped optical fibers show that TS doped PMMA is an appropriate material system as fiber core. PMMA based optical fibers doped with TS is photosensitive and suitable to write PFBGs.

2. Differing from previous understanding, PFBGs have been inscribed by phase masks that have zeroth order diffraction higher than 5%, which is the maximum value believed previously by others for phase mask to write FBGs. The calculation of the near-field pattern of phase masks shows the zeroth order diffraction does influence the distribution of light intensity along the strip of constructive interference. In addition, the calculation reveals that the second and the third diffraction also have impacts on the interference pattern, and hence the microstructure of the fabricated PFBGs.

3. The formation of PFBGs exhibits two distinct stages during long-time UV exposure in PMMA based POFs doped with TS. The increase in peak power

in the first stage most likely is due to photoisomerization of TS, whereas the peak increase in the second stage seems to be caused by the degradation of the PMMA.

4. The fading and recovery of the PFBGs after UV exposure, referred to as the relaxation process, was observed for the first time within the area of PFBGs. This relaxation process was found to speed up at elevated temperature, and it slowed down at dry conditions. The probable reason for this relaxation process was ascribed to the stress relaxation after the photoisomerization of TS because of the geometric difference of its trans and cis isomers.

5. The temperature sensitivity of PFBGs in PMMA based optical fibers has been found not as high as previously reported. Moreover, it is highly dependent on humidity. For a PFBGs around 1310 nm, the temperature sensitivity at 0 %RH and 60 %RH are -1 pm/°C (20 °C) and -8.7 pm/°C, respectively. The absolute values are almost two orders of magnitude lower than many values reported in literature. The measured intrinsic temperature sensitivity (at 0 %RH and at 20 °C) is even ten times smaller than that of FBGs in silica optical fibers, completely changing the notion of high temperature sensitivity of FBGs in polymer optical fibers.

6. PFBGs in PMMA based optical fibers have been found extremely sensitive to relative humidity. Such a grating at 1308 nm shifts 66 pm per 1 %RH at 20 °C, which is almost of one to two orders of magnitude larger than that caused by 1 °C in temperature change. This synergetic effect of temperature and humidity on PFBGs was first reported and systematically studied.

7. PFBGs in PMMA based optical fiber are very sensitive to salinity. An increase in molar concentration of 1 mol/L shifts the PFBGs 0.37 nm. This

value is three times higher than FBGs in silica fiber coated with hydrogels, and more than 20 times higher than silica FBGs coated with polyimide, and on the same level with the polyimide-coated polarization-maintaining photonic crystal fiber Sagnac interferometer.

8. Annealing has been found necessary to make the fabricated POFs thermally stable. In addition, annealing treatment was found having various impacts on the POFs and PFBGs. After complete annealing treatment, the Bragg wavelength shifted as large as -35 nm for a grating around 960 nm. The effective strain-optic coefficient was increased by annealing, and magnitudes of increase at various wavelengths were different.

9. Shear stress and pressure were simultaneously determined by a PFBGs based sensor, which places two PFBGs in a silicone cube, one horizontally embedded while the other one tilted. It is found that the strain along POF length is not uniform when the POFs are adhered to the host silicone matrix. By applying release agent onto POF surface and stretching POFs by using two gaskets from fiber ends, the induced strain on fiber becomes larger and uniform.

7.2. **Future Works**

This study has significantly improved the quality of single-mode POFs, closely examined the grating formation process, changed the commonly believed notion of the high temperature sensitivity of PFBGs, and discovered the synergetic effect of temperature and humidity on the FBGs in PMMA based fibers. Nevertheless, the following issues are of great scientific and practical importance in the future studies.

7.2.1. Study of the relaxation process of PFBGs after UV exposure

The relaxation process immediately after grating inscription in PMMA based fibers needs further investigation. Compared to the formation dynamics of PFBGs, the relaxation process seems more directly related to the Bragg grating formation. Photoisomerization of TS is the proposed photosensitivity of POFs, which leads to refractive index decrease of fiber core when it is doped within it. But this mechanism cannot explain this relaxation process. Several factors were excluded by the present study, such as moisture sorption/desorption, volatile molecules produced during inscription, thermal back-reaction of cis-4-stilbenemethanol. The other possible reason is the release of residual stress induced by photoisomerization of TS because of the dimension and structure difference of trans and cis isomers of 4-stilbenemethanol. They should be further investigated in details.

7.2.2. Development of FBGs in COC based optical fibers

Due to high moisture absorption of PMMA, FBGs in PMMA based fibers have been found extremely sensitive to environmental humidity. In other words, they are vulnerable to humidity variation. Humidity compensation is an acceptable approach, but it is more desirable to write PFBGs in a humidity-insensitive polymer, for example, COC. In addition, COC has a T_g up to 180 ℃, and that means the operation temperature of FBGs in fibers bases on it is broader than PMMA more than 70 ℃ (PMMA T_g ~104 ℃).

Previous literature reports microstructured POFs based on COC drawn from COC preforms drilled with holes. Also, FBGs have been reported in this kind of fibers.

However, the formation of FBG in pure COC based fiber is most likely due to certain degradation of the host polymer under long time phase masked UV exposure. Hence the fiber is inevitably damaged. In addition, as early mentioned, the microstructured fiber is more difficult to cleave and couple with single-mode silica fibers. Therefore, solid-core COC based optical fiber is more attractive, and this kind of fiber can be made photosensitive by the same doping technique used in this study.

7.2.3. **Quality improvement of single-mode POFs**

Compared to those fabricated at the beginning of the study, the quality of the fabricated POFs including the RIP and diameter fluctuation has been significantly improved. Nevertheless, they need further improvement. The fiber diameter variation is too large to be directly connected to fiber optic instruments. Hence the butt-coupling between POFs and silica fibers have to be done manually, which consumes time and energy, but also results in low repeatability of experiments. In addition, the measured attenuation of the fabricated POFs is two to three orders of magnitude higher than the absorption loss of bulk PMMA, suggesting a large room for attenuation reduce.

7.2.4. **Applications of PFBGs**

PFBGs have been fabricated more than ten years. Its responses to temperature and strain have been intensively studied, and some applications have been demonstrated, such as wavelength filter, accelerator, textile monitoring, and accelerator. Two other major areas have not been explored are bio sensing and chemical sensing. The

superiorities of PFBGs would be more obvious in these two areas thanks to their flexibility in chemical and biocompatibility.

As for the fabricated shear stress and pressure sensor, its dimension and structure can be further optimized by finite element analysis. More PFBGs may be added to measure the stress in the other directions.

7.2.5. Development of super-structured gratings in POFs

This study focused on FBGs, which reflect light into guiding mode. Hence, they are insensitive to environment conditions surrounding cladding surface, unless the measurand (e.g. water) can diffuse through thick cladding into the core. Otherwise, the cladding has to be polished to exposure the core.

Long period gratings (LPGs) couple light into cladding modes, and they are intrinsically sensitive to environment conditions surrounding cladding surface. Since the surface of POFs can be chemically modified, either by surface treatment or by polymerizing chemically-active cladding, the long period gratings in POFs can be made selectively sensitive to chemical, biomedical or physiological analyte. The super-structured gratings by combining FBGs and LPGs in POFs would provide more sophisticated solutions to these sensing areas.

Appendix 1 Specifications of the He-Cd Laser

Item	Specification
Laser Head Model	CSTR-G-18
Wavelength	325.0 nm
Specified Power	80 mW
Transverse Mode	TEM multimode
Mode Spacing (C/2l)	113 MHz
Spectral Bandwidth	1 GHz (0.35 pm)
Coherence Length	30 cm
Polarization	Linear, Vertical
Polarization Ratio	> 500:1
Noise (Peak-To-Peak)	15%
Noise (R.M.S.)	4%
Beam Diameter (1/E^2)	1.5 mm
Beam Divergence	1.0 mrad
Beam Pointing Stability (25 °C Constant Temperature)	±25 μrad
Warm Up Time (90% Power)	20 minutes
Power Stability (25 °C Constant Temperature)	±2%/4hr.
Power Stability (10 °~40 °C)	20%

References

[1] A. Othonos and K. Kalli, *Fiber Bragg Gratings :Fundamentals and Applications in Telecommunications and Sensing.* Boston, Mass.: Artech House, 1999.

[2] R. Kashyap, *Fiber Bragg Gratings.* Burlington, MA: Academic Press, 2010.

[3] A. Othonos, "Fiber Bragg gratings," *Review of Scientific Instruments,* vol. 68, pp. 4309-4341, DEC, 1997.

[4] K. O. Hill and G. Meltz, "Fiber Bragg grating technology fundamentals and overview," *J. Lightw. Technol.,* vol. 15, pp. 1263-1276, AUG, 1997.

[5] A. Othonos and K. Kalli, "Bragg gratings in optical fibers," in *Handbook of Advanced Electronic and Photonic Materials and Devices*, Hari Singh Nalwa, M.Sc. and Ph.D., Eds. Burlington: Academic Press, 2001, pp. 367-480.

[6] K. O. Hill, Y. Fujii, D. C. Johnson and B. S. Kawasaki, "Photosensitivity in optical fiber waveguides: Application to reflection filter fabrication," *Appl. Phys. Lett.,* vol. 32, pp. 647-649, May 15, 1978.

[7] G. Meltz, W. W. Morey and W. H. Glenn, "Formation of Bragg Gratings in Optical Fibers by a Transverse Holographic Method," *Opt. Lett.,* vol. 14, pp. 823-825, Aug 1, 1989.

[8] K. O. Hill, B. Malo, F. Bilodeau, D. C. Johnson and J. Albert, "Bragg Gratings Fabricated in Monomode Photosensitive Optical Fiber by Uv Exposure through a Phase Mask," *Appl. Phys. Lett.,* vol. 62, pp. 1035-1037, Mar 8, 1993.

[9] S. Yin, P. B. Ruffin and F. T. S. Yu, *Fiber Optic Sensors.* Boca Raton, FL: CRC Press/Taylor & Francis, 2008.

[10] A. Othonos, K. Kalli, D. Pureur and A. Mugnier. "Fibre bragg gratings," in *Wavelength Filters in Fibre Optics*, H. Venghaus, Ed. 2006, .

[11] I. R. Husdi, K. Nakamura and S. Ueha, "Sensing characteristics of plastic optical fibres measured by optical time-domain reflectometry," *Meas. Sci. Technol.,* vol. 15, pp. 1553, 2004.

[12] C. H. Jiang, M. G. Kuzyk, J. L. Ding, W. E. Johns and D. J. Welker, "Fabrication and mechanical behavior of dye-doped polymer optical fiber," *J. Appl. Phys.,* vol. 92, pp. 4-12, JUL 1, 2002.

[13] I. P. Kaminow, H. P. Weber and E. A. Chandross, "Poly (methyl methacrylate) dye laser with internal diffraction grating resonator," *Appl. Phys. Lett.,* vol. 18, pp. 497, 1971.

[14] A. Dodabalapur, E. A. Chandross, M. Berggren and R. E. Slusher, "Organic solid-state lasers: Past and future," *Science,* vol. 277, pp. 1787-1788, 1997.

[15] A. F. Abouraddy, M. Bayindir, G. Benoit, S. D. Hart, K. Kuriki, N. Orf, O. Shapira, F. Sorin, B. Temelkuran and Y. Fink, "Towards multimaterial multifunctional fibres that see, hear, sense and communicate," *Nat. Mater.,* vol. 6, pp. 336-347, MAY, 2007.

[16] K. Kalli, H. L. Dobb, D. J. Webb, K. Carroll, C. Themistos, M. Komodromos, G. Peng, Q. Fang and I. W. Boyd, "Development of an electrically tuneable Bragg grating filter in polymer optical fibre operating at 1.55 mu m," *Meas. Sci. Technol.,* vol. 18, pp. 3155-3164, OCT, 2007.

[17] K. Kalli, H. L. Dobb, D. J. Webb, K. Carroll, M. Komodromos, C. Themistos, G. D. Peng, Q. Fang and I. W. Boyd, "Electrically tunable Bragg gratings in single-mode polymer optical fiber," *Opt. Lett.,* vol. 32, pp. 214-216, FEB 1, 2007.

[18] M. C. Large, L. Poladian, G. W. Barton and M. A. v. Eijkelenborg, *Microstructured Polymer Optical Fibres.* Boston, MA: Springer Science+Business Media, LLC, 2007.

[19] Z. Xiong, G. D. Peng, B. Wu and P. L. Chu, "Highly tunable Bragg gratings in single-mode polymer optical fibers," *IEEE Photon. Technol. Lett.,* vol. 11, pp. 352-354, MAR, 1999.

[20] G. D. Peng, Z. Xiong and P. L. Chu, "Photosensitivity and gratings in dye-doped polymer optical fibers," *Opt. Fiber Technol.,* vol. 5, pp. 242-251, 1999.

[21] H. Y. Liu, H. B. Liu, G. D. Peng and P. L. Chu, "Observation of type I and type II gratings behavior in polymer optical fiber," *Opt. Commun.,* vol. 220, pp. 337-343, MAY 15, 2003.

[22] H. B. Liu, H. Y. Liu, G. D. Peng and P. L. Chu, "Novel growth behaviors of fiber Bragg gratings in polymer optical fiber under UV irradiation with low power," *IEEE Photon. Technol. Lett.,* vol. 16, pp. 159-161, JAN, 2004.

[23] J. M. Yu, X. M. Tao and H. Y. Tam, "Trans-4-stilbenemethanol-doped photosensitive polymer fibers and gratings," *Opt. Lett.,* vol. 29, pp. 156-158, JAN 15, 2004.

[24] T. Mizunami, T. V. Djambova, T. Niiho and S. Gupta, "Bragg Gratings in Multimode and Few-Mode Optical Fibers," *J. Lightwave Technol.,* vol. 18, pp. 230, 2000.

[25] Changgui Lu and Yiping Cui, "Fiber Bragg grating spectra in multimode optical fibers," *J. Lightw. Technol.,* vol. 24, pp. 598-604, 2006.

[26] Y. Luo, B. Yan, M. Li, X. Zhang, W. Wu, Q. Zhang and G. Peng, "Analysis of multimode POF gratings in stress and strain sensing applications," *Opt. Fiber Technol.,* vol. 17, pp. 201-209, 5, 2011.

[27] W. Yuan, A. Stefani, M. Bache, T. Jacobsen, B. Rose, N. Herholdt-Rasmussen, F. K. Nielsen, S. Andresen, O. B. Sørensen, K. S. Hansen and O. Bang, "Improved thermal and strain performance of annealed polymer optical fiber Bragg gratings," *Opt. Commun.,* vol. 284, pp. 176-182, 1/1, 2011.

[28] A. Stefani, W. Yuan, C. Markos and O. Bang, "Narrow Bandwidth 850-nm Fiber Bragg Gratings in Few-Mode Polymer Optical Fibers," *IEEE Photon. Technol. Lett.,* vol. 23, pp. 660-662, MAY 15, 2011.

[29] J. Terblanche, D. Schmieder and J. Meyer, "Fibre bragg gratings in polymer optical fibre at 980 nm," in *Proc. SPIE 7503: 20th International Conference on Optical Fibre Sensors,* Edinburgh, United Kingdom, 2009, pp. 75037F.

[30] I. P. Johnson, K. Kalli and D. J. Webb, "827 nm Bragg grating sensor in multimode microstructured polymer optical fibre," *Electron. Lett.,* vol. 46, pp. 1217, 2010.

[31] R. M. Waxler, D. Horowitz and A. Feldman, "Optical and physical parameters of Plexiglas 55 and Lexan," *Appl. Opt.,* vol. 18, pp. 101-104, 01/01, 1979.

[32] I. D. Nikolov and C. D. Ivanov, "Optical Plastic Refractive Measurements in the Visible and the Near-Infrared Regions," *Appl. Opt.,* vol. 39, pp. 2067-2070, 05/01, 2000.

[33] G. Khanarian, "Optical properties of cyclic olefin copolymers," *Opt. Eng.,* vol. 40, pp. 1024-6, 2001-06-01, 2001.

[34] J. M. Cariou, J. Dugas, L. Martin and P. Michel, "Refractive-index variations with temperature of PMMA and polycarbonate," *Appl. Opt.,* vol. 25, pp. 334-336, 1986.

[35] M. K. Szczurowski, T. Martynkien, G. Statkiewicz-Barabach, W. Urbanczyk, L. Khan and D. J. Webb, "Measurements of stress-optic coefficient in polymer optical fibers," *Opt. Lett.,* vol. 35, pp. 2013-2015, 2010.

[36] G. Zhou, C. F. J. Pun, H. Tam, A. C. L. Wong, C. Lu and P. K. A. Wai, "Single-Mode Perfluorinated Polymer Optical Fibers With Refractive Index of 1.34 for Biomedical Applications," *IEEE Photon. Technol. Lett.,* vol. 22, pp. 106-108, 2010.

[37] D. J. Webb and K. Kalli. "Polymer fiber bragg grating," in *Fiber Bragg Grating Sensors: Recent Advancements, Industrial Applications and Market Exploitation*, A. Cusano, A. Cutolo and J. Albert, Eds. 2011, [online]. Available: http://www.benthamscience.com/ebooks/9781608050840/contents.htm.

[38] H. Dobb, D. J. Webb, K. Kalli, A. Argyros, M. C. J. Large and M. A. van Eijkelenborg, "Continuous wave ultraviolet light-induced fiber Bragg gratings in few- and single-mode microstructured polymer optical fibers," *Opt. Lett.,* vol. 30, pp. 3296-3298, DEC 15, 2005.

[39] G. Peng, H. Y. Liu and P. L. Chu, "Dynamics and threshold behavior in polymer fiber bragg grating creation," in *Proc. SPIE 4803: Photorefractive Fiber and Crystal Devices: Materials, Optical Properties, and Applications VIII,* Seattle, WA, USA, 2002, pp. 164-178.

[40] H. Y. Liu, G. D. Peng, P. L. Chu, Y. Koike and Y. Watanabe, "Photosensitivity in low-loss perfluoropolymer (CYTOP) fibre material," *Electron. Lett.,* vol. 37, pp. 347-348, MAR 15, 2001.

[41] H. Y. Liu, G. D. Peng and P. L. Chu, "Thermal stability of gratings in PMMA and CYTOP polymer fibers," *Opt. Commun.,* vol. 204, pp. 151-156, APR 1, 2002.

[42] I. P. Johnson, W. Yuan, A. Stefani, K. Nielsen, H. K. Rasmussen, L. Khan, D. J. Webb, K. Kalli and O. Bang, "Optical fibre Bragg grating recorded in TOPAS cyclic olefin copolymer," *Electron. Lett.,* vol. 47, pp. 271-272, 2011.

[43] P. L. Chu, "Polymer optical fiber Bragg gratings," *Opt. Photonics News,* vol. 16, pp. 52-56, 2005.

[44] A. K. Baker and P. E. Dyer, "Refractive-index modification of polymethylmethacrylate (PMMA) thin films by KrF-laser irradiation," *Appl. Phys. A,* vol. 57, pp. 543-544, 1993.

[45] J. M. Yu, X. M. Tao, H. Y. Tam and M. S. Demokan, "Modulation of refractive index and thickness of poly(methyl methacrylate) thin films with UV irradiation and heat treatment," *Appl. Surf. Sci.,* vol. 252, pp. 1283-1292, DEC 15, 2005.

[46] T. Kada, T. Hiramatsu, K. Ogino, C. X. Liang, H. Machida, K. Kiso and S. Miyata, "Fabrication of Refractive Index Profiles in Poly (Methyl Methacrylate) using Ultraviolet Rays Irradiation," *Jpn. J. Appl. Phys.,* vol. 41, pp. 876, .

[47] P. J. Scully, D. Jones and D. A. Jaroszynski, "Femtosecond laser irradiation of polymethylmethacrylate for refractive index gratings," *J. Opt. A: Pure Appl. Opt.,* vol. 5, pp. S92, 2003.

[48] S. Sowa, W. Watanabe, T. Tamaki, J. Nishii and K. Itoh, "Symmetric waveguides in poly(methyl methacrylate) fabricated by femtosecond laser pulses," *Opt. Express,* vol. 14, pp. 291-297, JAN 9, 2006.

[49] J. Yu. "Photosensitive Polymer Optical Fibers and Gratings," Ph.D. thesis, The Hong Kong Polytechnic University, Hong Kong, 2005.

[50] J. Yu, X. Tao, H. Tam, D. Yang and M. S. Demokan, "Photo sensitivity and grating development in trans-4-stilbenemethanol-doped poly(methyl methacrylate) materials," *Opt. Commun.,* vol. 265, pp. 132-139, SEP 1, 2006.

[51] X. Tao, J. Yu and H. Tam, "Photosensitive polymer optical fibres and gratings," *Trans. Inst. Meas. Control,* vol. 29, pp. 255-270, 2007.

[52] G. H. Brown, *Photochromism.* New York: Wiley-Interscience, 1971.

[53] H. Dürr and H. Bouas-Laurent, *Photochromism: Molecules and Systems.* Elsevier Science Ltd, 2003.

[54] D. R. Lide, *CRC Handbook of Chemistry and Physics.* CRC press, 1993.

[55] G. B. Kistiakowsky and W. R. Smith, "Kinetics of Thermal Cis-Trans Isomerization. III," *J. Am. Chem. Soc.,* vol. 56, pp. 638-642, 03/01; 2012/03, 1934.

[56] Z. Sekkat and W. Knoll, *Photoreactive Organic Thin Films.* Academic Pr, 2002.

[57] X. Meng, A. Natansohn and P. Rochon, "Azo polymers for reversible optical storage .13. Photoorientation of rigid side groups containing two azo bonds," *Polymer,* vol. 38, pp. 2677-2682, MAY, 1997.

[58] O. Tanchak and C. Barrett, "Light-induced reversible volume changes in thin films of azo polymers: The photomechanical effect," *Macromolecules,* vol. 38, pp. 10566-10570, DEC 13, 2005.

[59] C. Wang and J. Xia, "Holographic grating relaxation studies of photo processes of azobenzenes in polymer hosts," *J. Phys. Chem.,* vol. 96, pp. 190-194, 1992.

[60] J. Zhang and C. H. Wang, "Simultaneous measurements of the diffusion coefficients of the dye molecule and its photoproduct by the holographic relaxation technique," *J. Phys. Chem.,* pp. 2296, .

[61] J. Zhang, B. Yu and C. Wang, "Holographic grating relaxation studies of camphorquinone diffusion in a polystyrene host," *J. Phys. Chem.,* vol. 90, pp. 1299-1301, 1986.

[62] G. D. Peng and P. L. Chu, "Polymer optical fiber photosensitivities and highly tunable fiber gratings," *Fiber Integr. Opt.,* vol. 19, pp. 277-293, 2000.

[63] Y. Luo, J. Zhou, Q. Yan, W. Su, Z. Li, Q. Zhang, J. Huang and K. Wang, "Optical manipulable polymer optical fiber Bragg gratings with azopolymer as core material," *Appl. Phys. Lett.,* vol. 91, pp. 071110, AUG 13, 2007.

[64] Y. Luo, Z. Li, R. Zheng, R. Chen, Q. Yan, Q. Zhang, G. Peng, G. Zou, H. Ming and B. Zhu, "Birefringent azopolymer long period fiber gratings induced by 532 nm polarized laser," *Opt. Commun.,* vol. 282, pp. 2348-2353, JUN 15, 2009.

[65] Y. Luo, Q. Zhang, H. Liu and G. Peng, "Gratings fabrication in benzildimethylketal doped photosensitive polymer optical fibers using 355 nm nanosecond pulsed laser," *Opt. Lett.,* vol. 35, pp. 751-753, MAR 1, 2010.

[66] M. G. Kuzyk, *Polymer Fiber Optics :Materials, Physics, and Applications.* Boca Raton: CRC Press, 2007.

[67] D. Bosc and C. Toinen, "Full Polymer Single-Mode Optical Fiber," *IEEE Photon. Technol. Lett.,* vol. 4, pp. 749-750, JUL, 1992.

[68] M. G. Kuzyk, U. C. Paek and C. W. Dirk, "Guest-Host Polymer Fibers for Nonlinear Optics," *Appl. Phys. Lett.,* vol. 59, pp. 902-904, AUG 19, 1991.

[69] D. W. Garvey, K. Zimmerman, P. Young, J. Tostenrude, J. S. Townsend, Z. Zhou, M. Lobel, M. Dayton, R. Wittorf, M. G. Kuzyk, J. Sounick and C. W. Dirk, "Single-mode nonlinear-optical polymer fibers," *J. Opt. Soc. Am. B-Opt. Phys.,* vol. 13, pp. 2017-2023, SEP, 1996.

[70] C. W. Dirk, A. Nagarur, J. J. Lu, L. X. Zhang, P. Kalamegham, J. Fonseca, S. Gopalan, S. Townsend, G. Gonzalez, P. Craig, M. Rosales, L. Green, K. Chan, R. Twieg, S. Ermer, D. Leung, S. Lovejoy, S. Lacroix, N. Godbout and E. Monette, "Molecular studies and plastic optical fiber device structures for nonlinear optical applications," in *Proc. SPIE 2527: Nonlinear Optical Properties of Organic Materials VIII,* San Diego, CA, USA, 1995, pp. 116-126.

[71] G. Barton, M. A. van Eijkelenborg, G. Henry, M. C. J. Large and J. Zagari, "Fabrication of microstructured polymer optical fibres," *Opt. Fiber Technol.,* vol. 10, pp. 325-335, OCT, 2004.

[72] Y. Zhang, K. Li, L. Wang, L. Ren, W. Zhao, R. Miao, M. Large C.J. and M. A. van Eijkelenborg, "Casting preforms for microstructured polymer optical fibre fabrication," *Opt. Express,* vol. 14, pp. 5541-5547, 06/12, 2006.

[73] C. W. Huang, M. C. Ho, H. H. Chien, K. J. Ma, Z. P. Zheng, C. P. Yu, H. C. Chang and C. C. Yang, "Design, fabrication, and characterization of microstructured polymer optical fibers," in *Lasers and Electro-Optics, 2003. CLEO/Pacific Rim 2003. the 5th Pacific Rim Conference on,* 2003, pp. 18 Vol.1.

[74] J. Zagari, A. Argyros, N. A. Issa, G. Barton, G. Henry, M. C. J. Large, L. Poladian and M. A. van Eijkelenborg, "Small-core single-mode microstructured polymer optical fiber with large external diameter," *Opt. Lett.,* vol. 29, pp. 818-820, 04/15, 2004.

[75] C. Zhang, D. J. Webb, K. Kalli, G. Emiliyanov, O. Bang and E. Kjær, "Bragg grating inscription in TOPAS microstructured polymer optical fibre," in *Proc. 16th Int. Conf. Polymer Opt. Fiber,* 2007, .

[76] G. Emiliyanov, J. B. Jensen, O. Bang, P. E. Hoiby, L. H. Pedersen, E. M. Kjær and L. Lindvold, "Localized biosensing with Topas microstructured polymer optical fiber," *Opt. Lett.,* vol. 32, pp. 460-462, 03/01, 2007.

[77] D. J. Webb, K. Kalli, C. Zhang, M. Komodromos, A. Argyros, M. Large, G. Emiliyanov, O. Bang and E. Kjaer, "Temperature sensitivity of bragg gratings in PMMA and TOPAS microstructured polymer optical fibres," in *Proc. SPIE 6990: Photonic Crystal Fibers II,* Strasbourg, FRANCE, 2008, pp. 69900L.

[78] W. Yuan, D. J. Webb, K. Kalli, K. Nielsen, A. Stefani, H. K. Rasmussen and O. Bang, "870nm bragg grating in single mode TOPAS microstructured polymer optical fibre," in *Proc. SPIE 7753: 21st International Conference on Optical Fiber Sensors,* 2011, pp. 77538X.

[79] I. Johnson, "Polymer PCF bragg grating sensors based on poly(methyl methacrylate) and TOPAS cyclic olefin copolymer," in *Proc. SPIE 8073: Optical Sensors 2011; and Photonic Crystal Fibers V,* 2011, pp. 80732V.

[80] H. M. Reeve, A. M. Mescher and A. F. Emery, "Investigation of steady-state drawing force and heat transfer in polymer optical fiber manufacturing," *J. Heat Transfer,* vol. 126, pp. 236-243, APR, 2004.

[81] H. M. Reeve, A. M. Mescher and A. F. Emery, "Unsteady natural convection of air in a tall axisymmetric, nonisothermal annulus," *Numerical Heat Transfer Part A-Applications,* vol. 45, pp. 625-648, APR, 2004.

[82] H. M. Reeve and A. M. Mescher, "Effect of unsteady natural convection on the diameter of drawn polymer optical fiber," *Opt. Express,* vol. 11, pp. 1770-1779, JUL 28, 2003.

[83] H. M. Reeve and A. M. Mescher, "A study on transient heating of polymer fiber preforms," *J. Mater. Process. Manuf. Sci.,* vol. 8, pp. 94-105, OCT, 1999.

[84] H. M. Reeve, A. M. Mescher and A. F. Emery, "Experimental and numerical investigation of polymer preform heating," *J. Mater. Process. Manuf. Sci.,* vol. 9, pp. 285-301, APR, 2001.

[85] H. M. Reeve, A. M. Mescher and A. F. Emery, "Investigation of convective heating in a polymer fiber drawing process," *Polymer Composites,* vol. 24, pp. 279-290, APR, 2003.

[86] K. Lyytikäinen, J. Zagari, G. Barton and J. Canning, "Heat transfer within a microstructured polymer optical fibre preform," *Modell. Simul. Mater. Sci. Eng.,* vol. 12, pp. S255, 2004.

[87] S. C. Xue, R. I. Tanner, G. W. Barton, R. Lwin, M. C. J. Large and L. Poladian, "Fabrication of microstructured optical fibers-part I: problem formulation and numerical modeling of transient draw process," *J. Lightw. Technol.,* vol. 23, pp. 2245-2254, 2005.

[88] S. Choudhury and Y. Jaluria, "Thermal transport due to material and gas flow in a furnace for drawing an optical fiber," *J. Mater. Res.,* vol. 13, pp. 494-503, FEB, 1998.

[89] W. J. Stewart, "Optical Fiber and Preform Profiling Technology," *IEEE Trans. Microwave Theory Tech.,* vol. 30, pp. 1439-1454, 1982.

[90] T. Ishigure, E. Nihei and Y. Koike, "Graded-Index Polymer Optical-Fiber for High-Speed Data Communication," *Appl. Opt.,* vol. 33, pp. 4261-4266, JUL 1, 1994.

[91] Y. Koike, T. Ishigure and E. Nihei, "High-Bandwidth Graded-Index Polymer Optical-Fiber," *J. Lightw. Technol.,* vol. 13, pp. 1475-1489, JUL, 1995.

[92] Y. Ohtsuka and Y. Shimizu, "Radial distribution of the refractive index in light-focusing rods: determination using Interphako interference microscopy," *Appl. Opt.,* vol. 16, pp. 1050-1053, 04/01, 1977.

[93] P. Ji, A. D. Q. Li and G. Peng, "Transverse birefringence in polymer optical fiber introduced in drawing process," in *Proc. SPIE 5212: Linear and Nonlinear Optics of Organic Materials III,* San Diego, CA, USA, 2003, pp. 108-116.

[94] T. Kaino, "Absorption losses of low loss plastic optical fibers," *Jpn. J. Appl. Phys.,* vol. 24, pp. 1661-1665, 1985.

[95] G. D. Peng, P. L. Chu, Z. J. Xiong, T. W. Whitbread and R. P. Chaplin, "Dye-doped step-index polymer optical fiber for broadband optical amplification," *J. Lightw. Technol.,* vol. 14, pp. 2215-2223, OCT, 1996.

[96] C. Koeppen, R. F. Shi, W. D. Chen and A. F. Garito, "Properties of plastic optical fibers," *J Opt Soc Am B,* vol. 15, pp. 727-739, 02/01, 1998.

[97] T. Kaino, M. Fujiki, S. Oikawa and S. Nara, "Low-loss plastic optical fibers," *Appl. Opt.,* vol. 20, pp. 2886-2888, 1981.

[98] C. Zhang, W. Zhang, D. J. Webb and G. -. Peng, "Optical fibre temperature and humidity sensor," *Electron. Lett.,* vol. 46, pp. 643-644, 2010.

[99] K. E. Carroll, C. Zhang, D. J. Webb, K. Kalli, A. Argyros and M. C. J. Large, "Thermal response of Bragg gratings in PMMA microstructured optical fibers," *Opt. Express,* vol. 15, pp. 8844-8850, JUL 9, 2007.

[100] M. van Eijkelenborg, A. Argyros, A. Bachmann, G. Barton, M. Large, G. Henry, N. Issa, K. Klein, H. Poisel, W. Pok, L. Poladian, S. Manos and J. Zagari, "Bandwidth and loss measurements of graded-index microstructured polymer optical fibre," *Electron. Lett.,* vol. 40, pp. 592-593, MAY 13, 2004.

[101] X. Chen, C. Zhang, D. J. Webb, G. Peng and K. Kalli, "Bragg grating in a polymer optical fibre for strain, bend and temperature sensing," *Meas. Sci. Technol.,* vol. 21, pp. 094005, 2010.

[102] N. G. Harbach. "Fiber Bragg Gratings in Polymer Optical Fibers," Ph.D. thesis, EPFL, Switerland, 2008.

[103] G. N. Harbach, H. G. Limberger and R. P. Salathé, "Influence of humidity and temperature on polymer optical fiber bragg gratings," in *Bragg Gratings, Photosensitivity, and Poling in Glass Waveguides,* Karlsruhe, Germany, 2010, .

[104] W. Wu, Y. Luo, X. Cheng, X. Tian, W. Qiu, B. Zhu, G. -. Peng and Q. Zhang, "Design and fabrication of single mode polymer optical fiber gratings," *J. Optoelectron. Adv. Mater.,* vol. 12, pp. 1652-1659, AUG, 2010.

[105] K. Kalli, D. J. Webb, K. Carroll, C. Zhang, A. Argyros, M. Large and M. van Eijkelenborg, "Non-linear temperature response of bragg gratings in doped and undoped holey polymer optical fibre," in *Proc. SPIE 6588: Photonic Crystal Fibers,* Prague, CZECH REPUBLIC, 2007, pp. E5880-E5880.

[106] Z. Xiong, G. D. Peng, B. Wu and P. L. Chu, "Effects of the zeroth-order diffraction of a phase mask on Bragg gratings," *J. Lightw. Technol.,* vol. 17, pp. 2361-2365, NOV, 1999.

[107] H. Y. Liu, G. D. Peng and P. L. Chu, "Thermal tuning of polymer optical fiber Bragg gratings," *IEEE Photon. Technol. Lett.,* vol. 13, pp. 824-826, AUG, 2001.

[108] H. B. Liu, H. Y. Liu, G. D. Peng and P. L. Chu, "Strain and temperature sensor using a combination of polymer and silica fibre Bragg gratings," *Opt. Commun.,* vol. 219, pp. 139-142, 4/15, 2003.

[109] A. D. Kersey, M. A. Davis, H. J. Patrick, M. LeBlanc, K. P. Koo, C. G. Askins, M. A. Putnam and E. J. Friebele, "Fiber grating sensors," *J. Lightw. Technol.,* vol. 15, pp. 1442-1463, 1997.

[110] X. Cheng, W. Qiu, W. Wu, Y. Luo, X. Tian, Q. Zhang and B. Zhu, "High-sensitivity temperature sensor based on Bragg grating in BDK-doped photosensitive polymer optical fiber," *Chin. Opt. Lett.,* vol. 9, pp. 020602, 2011.

[111] C. Zhang, X. Chen, D. J. Webb and G. D. Peng, "Water detection in jet fuel using a polymer optical fibre bragg grating," in *Proc. SPIE 7503: 20th International Conference on Optical Fibre Sensors,* Edinburgh, United Kingdom, 2009, pp. 750380.

[112] W. Yuan, L. Khan, D. J. Webb, K. Kalli, H. K. Rasmussen, A. Stefani and O. Bang, "Humidity insensitive TOPAS polymer fiber Bragg grating sensor," *Opt. Express,* vol. 19, pp. 19731-19739, 09/26, 2011.

[113] O. Kahle, U. Wielsch, H. Metzner, J. Bauer, C. Uhlig and C. Zawatzki, "Glass transition temperature and thermal expansion behaviour of polymer films investigated by variable temperature spectroscopic ellipsometry," *Thin Solid Films,* vol. 313–314, pp. 803-807, 2/13, 1998.

[114] M. Chanda, S. K. Roy and I. ebrary, *Plastics Technology Handbook.* Boca Raton, Fla.: Taylor & Francis Group, 2006.

[115] W. Martienssen and H. Warlimont, *Springer Handbook of Condensed Matter and Materials Data.* Heidelberg; New York: Springer, 2005.

[116] S. Bäumer, *Handbook of Plastic Optics.* Weinheim: Wiley-VCH, 2010.

[117] R. S. Moshrefzadeh, M. D. Radcliffe, T. C. Lee and S. K. Mohapatra, "Temperature dependence of index of refraction of polymeric waveguides," *J. Lightw. Technol.,* vol. 10, pp. 420-425, 1992.

[118] H. Y. Liu, H. B. Liu and G. D. Peng, "Tensile strain characterization of polymer optical fibre Bragg gratings," *Opt. Commun.,* vol. 251, pp. 37-43, 2005.

[119] R. D. Andrews and J. F. Rudd, "Photoelastic Properties of Polystyrene in the Glassy State. I. Effect of Molecular Orientation," *J. Appl. Phys.,* vol. 28, pp. 1091-1095, October, 1957.

[120] W. Zhang, D. J. Webb and G. -. Peng, "Remotely tuneable optical filter based on polymer fibre bragg grating," in *21st International Conference on Optical Fiber Sensors,* Ottawa, ON, USA, 2011, pp. 77537B-77537B-4.

[121] R. Van Boxel, T. Verbiest and A. Persoons, "Switchable bragg gratings in photochromic-doped graded-index polymer optical fibers," in *Optical Fibers and Passive Components,* Wuhan, China, 2004, pp. 77-84.

[122] R. Van Boxel. "Bragg Gratings in Photosensitive Graded Index Polymer Optical Fibres," Ph.D. thesis, Katholieke Universiteit Leuven, Belgium, 2005.

[123] X. Chen, C. Zhang, D. J. Webb, B. Van Hoe, G. Van Steenberge, K. Kalli, F. Berghmans, H. Thienpont, W. Urbanczyk, K. Sugden and G. D. Peng, "Polymer photonic sensing skin," in *Proc. SPIE 7653: Fourth European Workshop on Optical Fibre Sensors,* Porto, Portugal, 2010, pp. 76533A.

[124] X. Chen, C. Zhang, B. Van Hoe, D. J. Webb, K. Kalli, G. Van Steenberge and G. D. Peng, "Photonic skin for pressure and strain sensing," in *Proc. SPIE 7726: Optical Sensing and Detection,* Brussels, Belgium, 2010, pp. 772604.

[125] C. C. Ye, J. M. Dulleu-Barton, D. J. Webb, C. Zhang, G. -. Peng, A. R. Chambers, F. J. Lennard and D. D. Eastop, "Applications of polymer optical fibre grating sensors to condition monitoring of textiles," *J. Phys. : Conf. Ser,* vol. 178, pp. 12020-12020, 2009.

[126] H. Y. Liu, H. B. Liu, G. D. Peng and P. L. Chu, "Polymer optical fibre Bragg gratings based fibre laser," *Opt. Commun.,* vol. 266, pp. 132-135, OCT 1, 2006.

[127] H. Liu, G. Peng, H. Liu and P. L. Chu, "Polymer fibre bragg gratings tunable laser," in *Optical Fiber Communication Conference and Exposition and the National Fiber Optic Engineers Conference,* 2006, pp. OWM7.

[128] J. J. Pan, Y. Shi and T. Zhu, "Continuously tunable high power fiber lasers with 11 nm tunability," in *Optical Fiber Communication Conference, 1999, and the International Conference on Integrated Optics and Optical Fiber Communication. OFC/IOOC '99. Technical Digest,* 1999, pp. 199-201 vol.2.

[129] A. Stefani, Wu Yuan, S. Andresen and O. Bang, "Polymer optical fiber bragg grating sensors: Measuring acceleration," in *Optical Fibre Technology (ACOFT), 2010 35th Australian Conference on,* 2010, pp. 1-4.

[130] M. G. Kuzyk, D. W. Garvey, S. R. Vigil and D. J. Welker, "All-optical devices in polymer optical fiber," *Chem. Phys.,* vol. 245, pp. 533-544, JUL 1, 1999.

[131] H. Dobb, K. Carroll, D. J. Webb, K. Kalli, M. Komodromos, C. Themistos, G. D. Peng, A. Argyros, M. C. J. Large, M. A. van Eijkelenborg, Q. Fang and I. W. Boyd, "Grating based devices in polymer optical fibre," in *Proc. SPIE 6189: Optical Sensing II,* Strasbourg, France, 2006, pp. 18901-18901.

[132] S. N. Kasarova, N. G. Sultanova, C. D. Ivanov and I. D. Nikolov, "Analysis of the dispersion of optical plastic materials," *Opt. Mater.,* vol. 29, pp. 1481-1490, 7, 2007.

[133] T. Watanabe, N. Ooba, Y. Hida and M. Hikita, "Influence of humidity on refractive index of polymers for optical waveguide and its temperature dependence," *Appl. Phys. Lett.,* vol. 72, pp. 1533-1535, March 30, 1998.

[134] A. A. Bettiol, S. Venugopal Rao, T. C. Sum, J. A. van Kan and F. Watt, "Fabrication of optical waveguides using proton beam writing," *J. Cryst. Growth,* vol. 288, pp. 209-212, 2/2, 2006.

[135] D. Y. Kim, S. K. Tripathy, L. Li and J. Kumar, "Laser-induced holographic surface relief gratings on nonlinear optical polymer films," *Appl. Phys. Lett.,* vol. 66, pp. 1166, 1995.

[136] M. J. Saunders, "Optical fiber profiles using the refracted near-field technique: a comparison with other methods," *Appl. Opt.,* vol. 20, pp. 1645-1651, 1981.

[137] M. Young, "Optical fiber index profiles by the refracted-ray method (refracted near-field scanning)," *Appl. Opt.,* vol. 20, pp. 3415-3422, 1981.

[138] U. C. Paek and C. R. Kurkjian, "Calculation of cooling rate and induced stresses in drawing of optical fibers," *J. Am. Ceram. Soc.,* vol. 58, pp. 330-335, 1975.

[139] A. Siegmann, M. Narkis and N. Rosenzweig, "Softening temperature of glassy polymers as affected by residual stresses," *Polym. Eng. Sci.,* vol. 19, pp. 223-225, 1979.

[140] P. So and L. J. Broutman, "Residual stresses in polymers and their effect on mechanical behavior," *Polym. Eng. Sci.,* vol. 16, pp. 785-791, 1976.

[141] A. Siegmann, A. Buchman and S. Kenig, "Residual stresses in polymers. II. Their effect on mechanical behavior," *Polym. Eng. Sci.,* vol. 21, pp. 997-1002, 1981.

[142] W. Hermann, M. Hutjens and D. U. Wiechert, "Stress in optical waveguides. 3: Stress induced index change," *Appl. Opt.,* vol. 28, pp. 1980-1983, 1989.

[143] P. E. Dyer, R. J. Farley and R. Giedl, "Analysis of grating formation with excimer laser irradiated phase masks," *Opt. Commun.,* vol. 115, pp. 327-334, 3/15, 1995.

[144] J. Zhang and C. Wang, "Holographic grating relaxation measurements of dye diffusion in linear poly (methyl methacrylate) and crosslinked poly (methyl methacrylate) hosts," *Macromolecules,* vol. 20, pp. 2296-2300, 1987.

[145] G. D. Peng, Z. J. Xiong and P. L. Chu, "Fluorescence decay and recovery in organic dye-doped polymer optical fibers," *J. Lightw. Technol.,* vol. 16, pp. 2365-2372, DEC, 1998.

[146] N. B. Embaye, S. K. Ramini and M. G. Kuzyk, "Mechanisms of reversible photodegradation in disperse orange 11 dye doped in PMMA polymer," *J. Chem. Phys.,* vol. 129, pp. 054504, 7 August, 2008.

[147] Y. Zhu, J. Zhou and M. G. Kuzyk, "Two-photon fluorescence measurements of reversible photodegradation in a dye-doped polymer," *Opt. Lett.,* vol. 32, pp. 958-960, APR 15, 2007.

[148] B. F. Howell and M. G. Kuzyk, "Amplified spontaneous emission and recoverable photodegradation in polymer doped with Disperse Orange 11," *J Opt Soc Am B,* vol. 19, pp. 1790-1793, 08/01, 2002.

[149] Wu Yuan, A. Stefani and O. Bang, "Tunable Polymer Fiber Bragg Grating (FBG) Inscription: Fabrication of Dual-FBG Temperature Compensated Polymer Optical Fiber Strain Sensors," *IEEE Photon. Technol. Lett.,* vol. 24, pp. 401-403, 2012.

[150] P. Kronenberg, P. K. Rastogi, P. Giaccari and H. G. Limberger, "Relative humidity sensor with optical fiber Bragg gratings," *Opt. Lett.,* vol. 27, pp. 1385-1387, AUG 15, 2002.

[151] W. D. Drotning and E. P. Roth, "Effects of Moisture on the Thermal-Expansion of Poly(methylmethacrylate)," *J. Mater. Sci.,* vol. 24, pp. 3137-3140, SEP, 1989.

[152] J. Cong, X. Zhang, K. Chen and J. Xu, "Fiber optic Bragg grating sensor based on hydrogels for measuring salinity," *Sens. Actuators, B,* vol. 87, pp. 487-490, 12/20, 2002.

[153] L. Men, P. Lu and Q. Chen, "A multiplexed fiber Bragg grating sensor for simultaneous salinity and temperature measurement," *J. Appl. Phys.,* vol. 103, pp. 053107, 1 March, 2008.

[154] C. Wu, B. Guan, C. Lu and H. Tam, "Salinity sensor based on polyimide-coated photonic crystal fiber," *Opt. Express,* vol. 19, pp. 20003-20008, 10/10, 2011.

[155] M. Lord, R. Hosein and R. B. Williams, "Method for in-shoe shear stress measurement," *J. Biomed. Eng.,* vol. 14, pp. 181-186, 5, 1992.

[156] P. Cavanagh, J. Ulbrecht and G. Caputo, "New developments in the biomechanics of the diabetic foot," *Diabetes-Metab. Res. Rev.,* vol. 16, pp. S6-S10, SEP-OCT, 2000.

[157] J. R. Mackey and B. L. Davis, "Simultaneous shear and pressure sensor array for assessing pressure and shear at foot/ground interface," *J. Biomech.,* vol. 39, pp. 2893-2897, 2006.

[158] M. Yavuz, G. Botek and B. L. Davis, "Plantar shear stress distributions: Comparing actual and predicted frictional forces at the foot–ground interface," *J. Biomech.,* vol. 40, pp. 3045-3049, 2007.

[159] T. Maeno, T. Kawamura and S. Cheng, "Friction estimation pressing an elastic finger-shaped sensor against a surface," *IEEE Transactions on Robotics and Automation,* vol. 20, pp. 222-228, APR, 2004.

[160] M. Ohka, Y. Mitsuya, I. Higashioka and H. Kabeshita, "An experimental optical three-axis tactile sensor for micro-robots," *Robotica,* vol. 23, pp. 457-465, JUL-AUG, 2005.

[161] Eun-Soo Hwang, Jung-hoon Seo and Yong-Jun Kim, "A Polymer-Based Flexible Tactile Sensor for Both Normal and Shear Load Detections and Its Application for Robotics," *J. Microelectromech. Syst.,* vol. 16, pp. 556-563, 2007.

[162] N. Wettels, A. R. Parnandi, Ji-Hyun Moon, G. E. Loeb and G. S. Sukhatme, "Grip Control Using Biomimetic Tactile Sensing Systems," *Mechatronics, IEEE/ASME Transactions on,* vol. 14, pp. 718-723, 2009.

[163] M. Cheng, C. Lin, Y. Lai and Y. Yang, "A Polymer-Based Capacitive Sensing Array for Normal and Shear Force Measurement," *Sensors,* vol. 10, pp. 10211-10225, NOV, 2010.

[164] M. I. Tiwana, A. Shashank, S. J. Redmond and N. H. Lovell, "Characterization of a capacitive tactile shear sensor for application in robotic and upper limb prostheses," *Sens. Actuators, A,* vol. 165, pp. 164-172, 2, 2011.

[165] J. Missinne, E. Bosman, B. Van Hoe, G. Van Steenberge, S. Kalathimekkad, P. Van Daele and J. Vanfleteren, "Flexible Shear Sensor Based on Embedded

Optoelectronic Components," *IEEE Photon. Technol. Lett.,* vol. 23, pp. 771-773, 2011.

[166] R. Hosein and M. Lord, "A study of in-shoe plantar shear in normals," *Clin. Biomech.,* vol. 15, pp. 46-53, 1, 2000.

[167] Y. Cong, J. T. Cheung, A. K. L. Leung and M. Zhang, "Effect of heel height on in-shoe localized triaxial stresses," *J. Biomech.,* vol. 44, pp. 2267-2272, AUG 11, 2011.

[168] H. Yousef, M. Boukallel and K. Althoefer, "Tactile sensing for dexterous in-hand manipulation in robotics—A review," *Sens. Actuators, A,* vol. 167, pp. 171-187, 6, 2011.

[169] S. Kärki, J. Lekkala, H. Kuokkanen and J. Halttunen, "Development of a piezoelectric polymer film sensor for plantar normal and shear stress measurements," *Sens. Actuators, A,* vol. 154, pp. 57-64, 8/31, 2009.

[170] D. Roche, C. Richard, L. Eyraud and C. Audoly, "Shear stress sensor using piezoelectric bimorphs bending," *Ultrasonics,* vol. 34, pp. 147-151, 6, 1996.

[171] L. Wang and D. J. Beebe, "A silicon-based shear force sensor: development and characterization," *Sens. Actuators, A,* vol. 84, pp. 33-44, 8/1, 2000.

[172] B. J. Kane, M. R. Cutkosky and G. T. A. Kovacs, "A traction stress sensor array for use in high-resolution robotic tactile imaging," *J. Microelectromech. Syst.,* vol. 9, pp. 425-434, 2000.

[173] W. L. Jin and C. D. Mote Jr., "Development and calibration of a sub-millimeter three-component force sensor," *Sens. Actuators, A,* vol. 65, pp. 89-94, 2/15, 1998.

[174] P. Laing, H. Deogan, D. Cogley, S. Crerand, P. Hammond and L. Klenerman, "The development of the low profile Liverpool shear transducer," *Clin. Phys. Physiol. Meas.,* vol. 13, pp. 115, 1992.

[175] W. C. Wang, W. R. Ledoux, B. J. Sangeorzan and P. G. Reinhall, "A shear and plantar pressure sensor based on fiber-optic bend loss," *J. Rehabil. Res. Dev.,* vol. 42, pp. 315-325, MAY-JUN, 2005.

[176] S. C. Tjin, R. Suresh and N. Q. Ngo, "Fiber Bragg grating based shear-force sensor: modeling and testing," *J. Lightw. Technol.,* vol. 22, pp. 1728-1733, 2004.

[177] R. Suresh, S. C. Tjin and S. Bhalla, "Multi-component force measurement using embedded fiber Bragg grating," *Opt. Laser Technol.,* vol. 41, pp. 431-440, 6, 2009.

[178] S. Webb, K. Peters, M. Zikry, T. Vella, S. Chadderdon, R. Selfridge and S. Schultz, "Wavelength hopping due to spectral distortion in dynamic fiber Bragg grating sensor measurements," *Meas. Sci. Technol.,* vol. 22, pp. 065301, 2011.